Advances in Two-Dimensional Organic-Inorganic Hybrid Perovskites

Journal:	*Energy & Environmental Science*
Manuscript ID	EE-REV-11-2019-003757.R1
Article Type:	Review Article
Date Submitted by the Author:	24-Jan-2020
Complete List of Authors:	Zhang, Fei; National Renewable Energy Laboratory, Chemistry and Nanoscience Center; Tianjin University, School of Chemical Engineering and Technology Lu, Haipeng; National Renewable Energy Laboratory, Chemistry & Nanoscience Center Tong, Jinhui; National Renewable Energy Laboratory, Chemistry and Nanoscience Center Berry, Joseph; National Renewable Energy Laboratory (NREL), United States, National Center for Photovoltaics Beard, Matthew; National Renewable Energy Laboratory, Chemical and Nanoscience Zhu, Kai; National Renewable Energy Laboratory, Chemical and Materials Science Center

Advances in Two-Dimensional Organic-Inorganic Hybrid Perovskites

Fei Zhang,[1,+] Haipeng Lu,[1,+] Jinhui Tong,[1] Joseph J. Berry,[2] Matthew C. Beard,[1] Kai Zhu[1,*]

[1] Chemistry and Nanoscience Center, National Renewable Energy Laboratory, Golden, Colorado 80401, USA. Email: kai.zhu@nrel.gov

[2] Materials Science Center, National Renewable Energy Laboratory, Golden, Colorado 80401, USA

[+]These authors contributed equally to this paper.

Keywords: Two-dimensional; perovskite; solar cell; spintronic; light-emitting device

Abstract: Two-dimensional (2D) perovskites have attracted considerable interest for their promising applications for solar cells and other optoelectronics, such as light-emitting diodes, spintronics, and photodetectors. Here, we review the recent achievements of 2D perovskites for various optoelectronic applications. First, we discuss the basic structure and optoelectronic properties of 2D perovskites, including band structure, optical properties, and charge transport. We then highlight recent achievements using 2D perovskites in solar cells and beyond solar cells, including progress on various synthesis strategies and their impact on structural and optoelectronic properties. Finally, we discuss current challenges and future opportunities to further develop 2D perovskites for various applications.

1. Introduction

Photovoltaics (PV) have witnessed the rapid rise of solution-processable organic-inorganic halide perovskites, which will likely become competitive in providing efficient and cheap solar energy.[1, 2] Over the course of about a decade, the power conversion efficiency (PCE) of single-junction perovskite solar cells (PSCs) has achieved a certified 25.2%,[3] which is comparable to that of other commercial PV technologies.[4] As a result, PSCs have attracted explosive attention from academia and industry. Weber *et al.* first established the unique structure and properties of three-dimensional (3D) perovskites in 1978.[5, 6] Then, in the 1990s, more findings of their unique optoelectronic properties were further developed by Mitzi *et al.*[7, 8] However, the initial several reports on PSCs between 2009 and 2012[9-11] are what caused these materials to begin to attract worldwide attention.

In the first report of PSCs, Miyasaka *et al.* used methylammonium lead triiodide ($CH_3NH_3PbI_3$, or $MAPbI_3$) as a light-absorbing material with a liquid electrolyte in dye-sensitized solar cells (DSSCs), yielding a PCE of 3.8% in 2009.[9] Later, Park *et al.* used the solid-state hole-transport material (HTM) of 2,2',7,7'-tetrakis(N,N-di-p-methoxyphenylamine)-9,9'-spirobifluorene (spiro-OMeTAD) to replace the liquid electrolyte, and they obtained an efficiency of 9.7% in 2012.[10] Around the same time, Snaith *et al.* demonstrated performance of >10% for the solid-state PSCs.[11] These breakthroughs have led to extensive research interest in PSCs.[12-25]

During the past several years, the PSC field has focused more on increasing the long-term operational stability of PSCs.[26] A large number of studies have focused on optimizing perovskite absorbers (e.g., composition,[27, 28] perovskite nanostructures,[29, 30] tolerance factor,[31, 32] defect passivation,[33, 34] additive control[35, 36]), device structures (e.g., contact layer[37-40] and interface modification[41, 42]), and device encapsulation.[43, 44] One promising category involving the use of two-dimensional (2D) or quasi-2D perovskite has also shown great potential for improving the stability of PSCs.[45, 46]

Unlike small cations in 3D perovskites (e.g., MA^+, formamidinium (FA^+), and Cs^+), the bulky organic cations in 2D perovskites provide a steric barrier for surface water adsorption.[47, 48] The large hydrophobic cation in the 2D perovskite crystal lattice can effectively suppress moisture intrusion.[49] However, the 2D perovskites are generally not a good choice as an absorber for solar cell application because of their wide optical bandgap and limited charge transport associated with the 2D structure. Since the first report in 2014 of 2D perovskites as absorbers in solar cells having 4.73% PCE,[50] the reported PCE of 2D PSCs has reached ~18%,[51] which is still much lower than that of 3D PSCs (~25%). Rather than directly using 2D perovskites as the solar cell absorbers, an alternative approach—using 2D perovskite structures to enhance the surface properties of 3D perovskite grains and films (normally referred to as 3D/2D mixed-dimensionality perovskites)—has shown promise for improving both the stability and performance of perovskites across a wide range of compositions.[21, 22, 52-55]

In addition to solar cell applications, 2D hybrid perovskites offer a much greater playground for chemists to investigate fundamental structure-property relationships. In contrast to their 3D counterparts, where the choice of the organic moiety is restricted by the Goldsmith tolerance factor, many paths of chemical engineering in 2D perovskites are possible because the tolerance factor is relaxed. For instance, a library of organic ligands has been demonstrated in 2D hybrid perovskites, and the inorganic layer thickness can also be tuned synthetically. This rich chemical tunability provides unique opportunities to control their structural distortion, quantum and dielectric confinement, exciton-phonon coupling, and Rashba splitting, which, in turn, modulate their optical, electronic, and spin properties. For this reason, 2D perovskites have shown tremendous potential for photoemission (exciton vs. broad emission), spintronic, and photodetector applications (**Figure 1**).

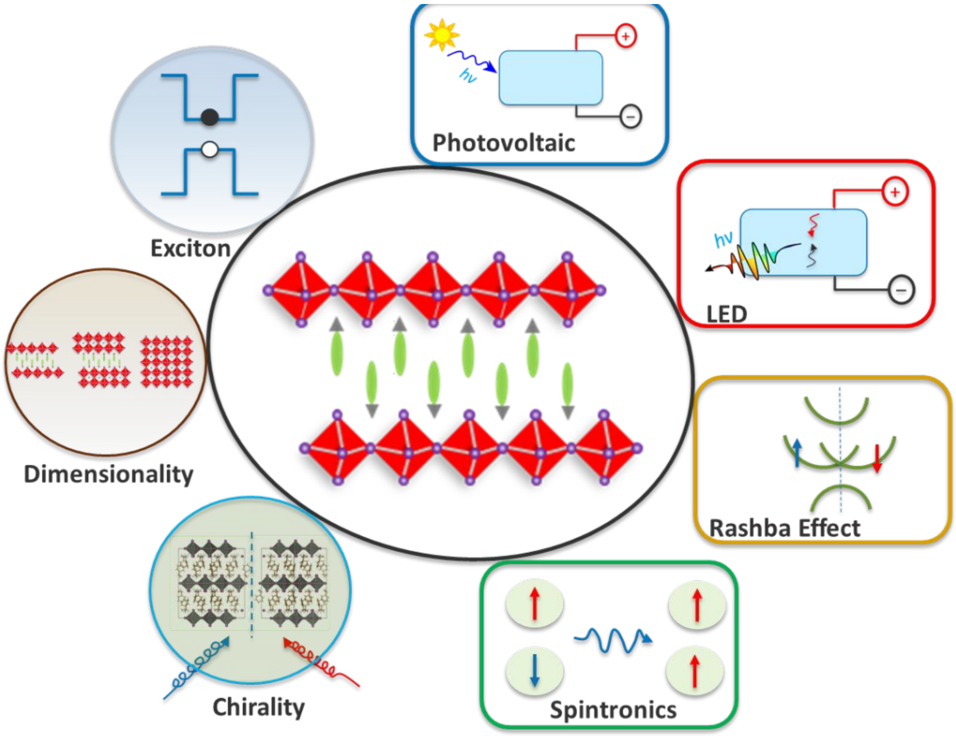

Figure 1. Illustration of 2D perovskites with structure tunability for a variety of optoelectronic applications.

In this review, we discuss recent advances of 2D perovskites for various optoelectronic applications. First, we discuss the structure and optoelectronic properties of 2D perovskites, including band structure, optical properties, and charge transport. We then highlight recent achievements of using 2D perovskite in solar cells and then go beyond solar cells to examine applications including light-emitting diodes (LEDs), spintronic applications, and photodetectors. Finally, we discuss the challenges and future opportunities for further developing 2D perovskites for a wide range of applications.

2. Chemical and Crystal Structure

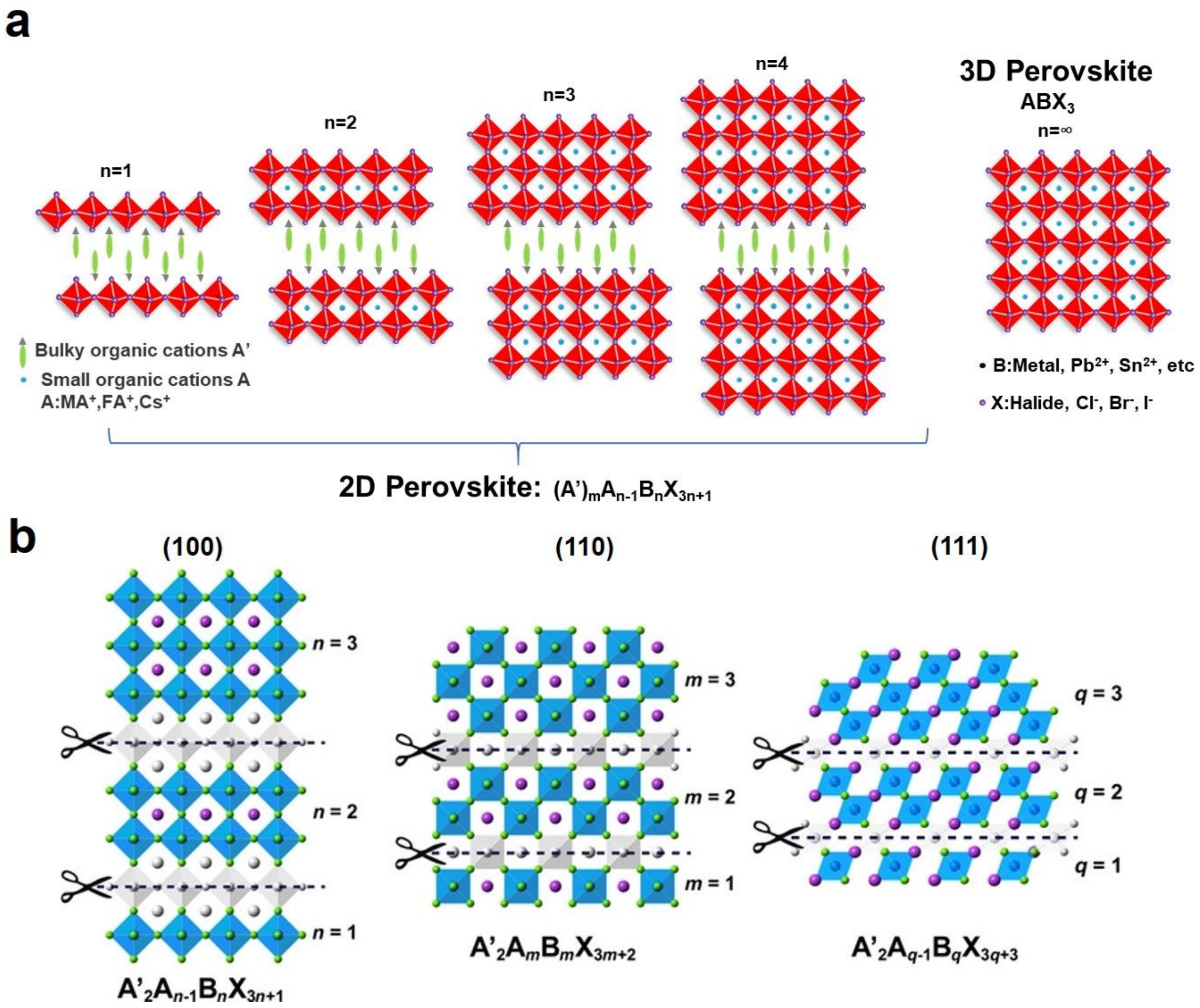

Figure 2. (**a**) Schematic comparing 2D and 3D perovskite structures. (**b**) Schematic of different oriented families of 2D perovskites: <100> plane, $A'_2A_{n-1}B_nX_{3n+1}$; <110> plane, $A'_2A_mB_mX_{3m+2}$; and <111> plane, $A'_2A_{q-1}B_qX_{3q+2}$. Cuts along ⟨100⟩, ⟨110⟩ and ⟨111⟩ directions (grey parts) result in the corresponding different types of 2D perovskites. Reproduced with permission from ref. 56. Copyright 2019, Wiley-VCH.

The standard 3D perovskites have a general structure of ABX_3, and six halide anions (X site; e.g., I^-, Br^-, and Cl^-) coordinated to a divalent metal cation (B site; e.g., Sn^{2+} and Pb^{2+}) form a BX_6 octahedral framework (**Figure 2a**).[57] Twelve monovalent cations (A site; e.g., MA^+, FA^+, and Cs^+) occupy the centers of four BX_6 octahedra. Each of the A, B, and X sites can contain one or multiple elements, allowing flexibility in adjusting the properties of the perovskite. Whether or not certain compositions can form a stable perovskite structure is often estimated based on a simple geometric consideration, the Goldschmidt tolerance factor (*t*),[58]

$$t = \frac{r_{\mathrm{A}} + r_{\mathrm{X}}}{\sqrt{2}(r_{\mathrm{B}} + r_{\mathrm{X}})}$$

where r_{A}, r_{B}, and r_{X} are the corresponding ionic radii. Essentially, when *t* is in the range of ~0.8–1.0, a stable 3D perovskite structure can be formed.[48] Moreover, the octahedral factor ($\mu = r_{\mathrm{B}}/r_{\mathrm{X}}$; μ is normally between 0.4 and 0.9) can be used to empirically evaluate whether a B-site atom prefers an octahedral coordination of the X-site atom (as opposed to other coordination numbers).[59, 60]

The 2D perovskite is generally described with a formula $(A')_m(A)_{n-1}B_nX_{3n+1}$, where A' can be divalent ($m = 1$) or monovalent ($m = 2$) cations that form a bilayer or monolayer connecting the inorganic $(A)_{n-1}B_nX_{3n+1}$ 2D sheets, where *n* indicates the layer thickness of metal halide sheets that can be adjusted by tuning precursor composition (**Figure 2a**).[61, 62] Generally, the organic A'-site cation can be arbitrarily long so that large, high-aspect-ratio cations (e.g., aliphatic- or aromatic-based cations) can be employed. Note that the geometry of a 2D octahedral arrangement typically contains a BX_4^{2-} inorganic unit, and the negative charge from the additional anion needs to be balanced by a positive charge (e.g., $A_2'BX_4$ when $n = 2$ and A' is a monovalent cation). It is worth noting that the limit $n = \infty$ corresponds to the 3D perovskite, whereas $n = 1$ represents the pure 2D, and $1 < n \leq 5$ is often known as quasi-2D. More importantly, a mixture of 3D perovskite and low-*n* phases (e.g., $n \leq 3$) can form even in the case of high *n* values (e.g., $n = 30$–60),[20] which we refer to as quasi-3D perovskites. With the increase of *n*, the differences of thermodynamic stability in the high-*n* structures become smaller, which makes it difficult to prepare phase-pure high-*n* structures.[63] Thus, the *n* value of such perovskites is usually described based on the precursor composition.

We can conceptually obtain 2D halide perovskite layers by cutting along the <100>, <110>, and <111> crystallographic planes of the corresponding 3D perovskite structure, leading to three 2D perovskite families with different orientations (i.e., <100>, <110>, and <111>; **Figure 2b**).

The general formula of <100>-oriented 2D perovskites is $A'_2A_{n\text{-}1}B_nX_{3n+1}$, and their inorganic sheets are obtained by taking *n* layers along the 100 direction of the 3D perovskites. This structure represents the most commonly studied 2D halide perovskites. Because the <110>-oriented perovskite layer is often highly distorted, interesting behaviors such as of the formation of self-trapped excitons, and broad-band/white-light emission at room temperature.[64] In addition, there are few reports on the use of <110>-oriented perovskites as absorbers in solar cells, which is likely caused by the difficulty of modulating the thickness of the inorganic layers in these materials and few cations that can stabilize their structures.[56, 65] The <111>-oriented 2D perovskites have a formula $A'_2A_{q\text{-}1}B_qX_{3q+2}$ ($q > 1$) and can only be constructed from group 15 B^{3+} ions (e.g., Bi, Sb, As).[66] The <111>-oriented perovskites are attractive solar cell absorbers due to their *p*-type-like character and relatively small effective masses for both holes and electrons; however, their strong excitonic nature appears to limit the performance for solar cells thus far in their development.[48] In this review, we focus on the commonly reported <100>-oriented 2D perovskites. This class of materials can be further divided into Ruddlesden-Popper (RP) phases (**Figure 3a**),[67, 68] Dion-Jacobson (DJ) phases (**Figure 3b**),[69-71] and the phases with alternating cations in the interlayer space (ACI) (**Figure 3c**).[72, 73]

For the most commonly studied RP-phase 2D perovskites, a relatively weak van der Waals gap forms between a bilayer of monovalent cations and two adjacent lead halide sheets. The RP compositions are generally described as $A'_2A_{n\text{-}1}B_nX_{3n+1}$,[69] where A' is aryl ammonium or alkyl cation (typical examples include phenylethylammonium (PEA^+) and butylammonium (BA^+)); small A cation is typically Cs^+, FA^+, or MA^+; B site is Sn^{2+} or Pb^{2+}; and the X site is I^-, Br^-, or Cl^-. For the RP phase, the inorganic layers are often offset by one octahedral unit and present certain in-plane displacement (**Figure 3a**). Alternatively, diamine compounds with two amino groups can avoid any gaps by forming hydrogen bonds on both ends with the two adjacent inorganic sheets,[74] leading to a more stable DJ-phase 2D perovskite with $A'A_{n\text{-}1}B_nX_{3n+1}$ stoichiometry. The typical examples are 3-(aminomethyl)piperidinium ($3AMP^+$) and 4-(aminomethyl)piperidinium ($4AMP^+$). Adjacent layers in the DJ phase have no offsets and are stacked on top of each other (**Figure 3b**). For ACI-phase 2D perovskite with the formula $A'A_nB_nX_{3n+1}$,[72] the small A cation not only resides in the lead halide sheets but also fills in the interlayer with the large A' cation, adopting the layer-stacking characteristics of both DJ and RP structures (**Figure 3c**). Note that guanidinium (Gua^+) is the only cation that is reported, so far, to form the ACI structure. Obviously, the interlayer distance varies with the choice of spacing cation A′, and the RP phases have larger interlayer distance due to the requirement of a bilayer of spacer organic cations.

Many bulky organic cations have been reported to incorporate into a 2D perovskite and later into a solar cell; the reported bulky cations for RP- and DJ-phase 2D perovskites are summarized in **Figure 4**. In general, the properties determining whether a cation is suitable as a spacer include: 1) the net positive charge and degree of substitution of the perovskite anchoring site (primary ammonium > secondary amine > tertiary amine > quaternary amine, in descending order); 2) hydrogen-bonding ability; 3) space-filling ability (linear cross cations > branch irregular cations); and 4) stereochemical configuration (aromatic hydrocarbons < flexible aliphatic hydrocarbons).[65]

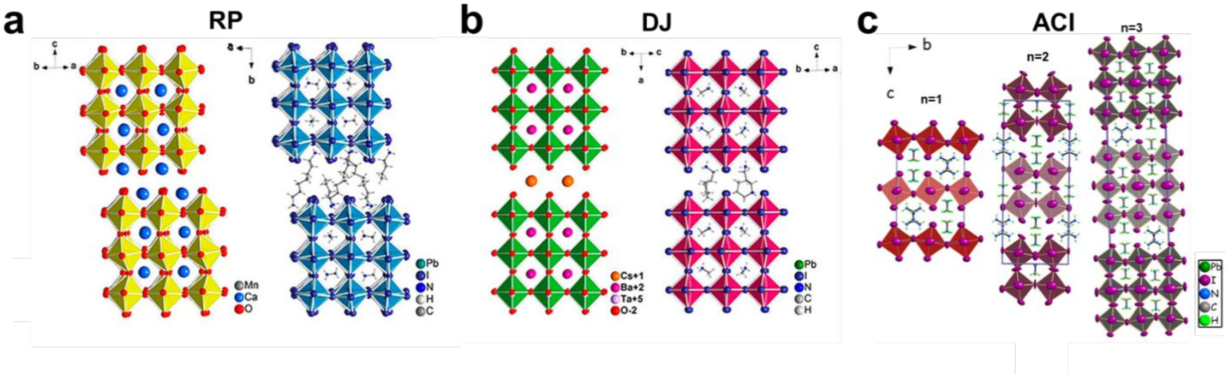

Figure 3. Examples of RP-, DJ-, and ACI-phase 2D perovskite structures. (**a**) $Ca_4Mn_3O_{10}$ (left) and $(BA)_2(MA)_2Pb_3I_{10}$ ($n = 3$; right); (**b**) $CsBa_2Ta_3O_{10}$ (left) and $(3AMP)(MA)_2Pb_3I_{10}$ ($n = 3$; right). Reproduced with permission from ref. 69. Copyright 2018, American Chemical Society. (**c**) $(Gua)(MA)_nPb_nI_{3n+1}$($n = 1$, 2, 3). Reproduced with permission from ref. 72. Copyright 2017, American Chemical Society.

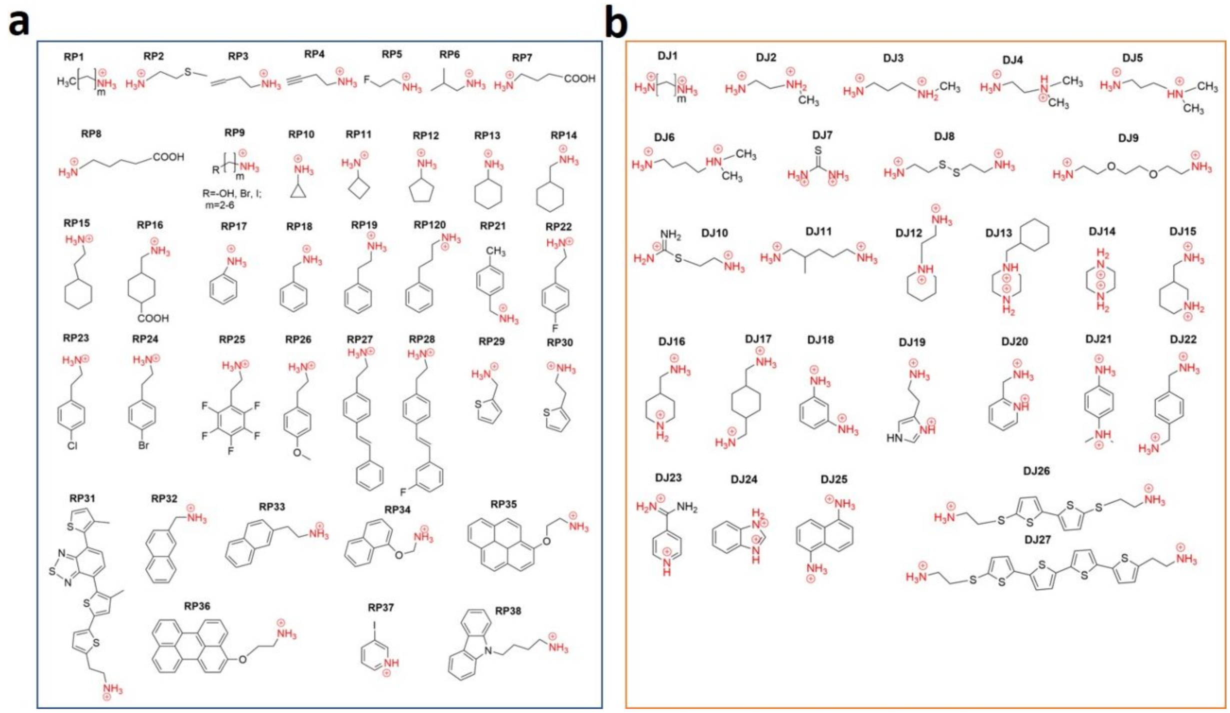

Figure 4. Summary of different bulky cations for RP- and DJ-phase 2D perovskites. **RP phases:** RP1, ethylammonium (EA^+, *m* = 1),[75, 76] propan-1-ammonium (*m* = 2),[77, 78] butan-1-ammonium (BA, *m* = 3),[7, 79, 80] pentan-1-ammonium (*m* = 4),[81] hexan-1-ammonium (*m* = 5),[81] heptan-1-ammonium (*m* = 6),[82] octan-1-ammonium (*m* = 7),[82] nonan-1-ammonium (*m* = 8);[82] decan-1-ammonium (*m* = 9),[82, 83] undecan-1-ammonium (*m* = 10);[83] RP2, 2-(methylthio)ethylamine (MTEA);[84] RP3, allylammonium (ALA);[85] RP4, but-3-yn-1-ammonium (BYA);[86] RP5, 2-fluoroethylammonium;[87] RP6, isobutylammonium (iso-BA);[88] RP7, ammonium 4-butyric acid (GABA);[89] RP8, 5-ammonium valeric acid (5-AVA);[90] RP9, heteroatom-substituted alkylammonium;[91] RP10, cyclopropylammonium;[92, 93] RP11, cyclobutylammonium;[92, 93] RP12, cyclopentylammonium;[92, 93] RP13, cyclohexylammonium;[92, 93] RP14, cyclohexylmethylammonium;[94] RP15, 2-(1-cyclohexenyl)ethylammonium;[95, 96] RP16, (carboxy)cyclohexylmethylammonium (TRA);[97] RP17, phenyltrimethylammonium (PTA);[98] RP18, benzylammonium (BZA);[99-104] RP19, phenylethylammonium (PEA);[50, 100, 101, 105-108] RP20, propyl phenyl ammonium (PPA);[100, 101] RP21, 4-methylbenzylammonium;[109] RP22, 4-fluorophenylethylammonium (F-PEA);[106, 110-113] RP23, 2-(4-chlorophenyl) ethanaminium (Cl-PEA);[111] RP24, 2-(4-bromophenyl) ethanaminium (Br-PEA);[111] RP25, perfluorophenethylammonium (F5-PEA);[114] RP26, 4-methoxyphenethylammonium (MeO-PEA);[112] RP27, 2-(4-stilbenyl)ethanammonium (SA);[115] RP28, 2-(4-(3-fluoro)stilbenyl)ethanammonium (FSA);[115] RP29, 2-thienylmethylammonium (ThMA);[116] RP30, 2-(2-thienyl)ethanaminium;[116] RP31, 2-(4'-Methyl-5'-(7-(3-methylthiophen-2-yl)benzo[c][1,2,5]thiadiazol-4-yl)-[2,2'-bithiophen]-5-yl)ethan-1-aminium (BTM);[117] RP32, 1-(2-naphthyl)methanammonium (NMA);[118] RP33, 2-(2-naphthyl)ethanammonium (NEA);[118] RP34, naphthalene-O-ethylammonium;[119] RP35, pyrene-O-ethylammonium;[119] RP36, perylene-*O*-ethylammonium;[119] RP37, 3-iodopyridinium (IPy);[97] RP38, carbazole alkylammonium (CA-C4).[120] **DJ phases:** DJ1, propane-1,3- diaminium (PDA, *m* = 3);[121] butane-1,4-diaminium (BDA, *m* = 4);[122-126] pentane-1,5-diaminium (*m* = 5);[125] hexane-1,6-diaminium (HDA, *m* = 6);[124, 125] heptane-1,7-diaminium (*m* = 7);[125] octane-1,8-diaminium (ODA, *m* = 8);[124, 125] nonane-1,9-diaminium (*m* = 9)[125] decane-1,10-diaminium (*m* = 10);[126] dodecane-1,12-diaminium (m=12);[126, 127] DJ2, N^1-methylethane-1,2-diammonium (N-MEDA);[128] DJ3, N^1-methylpropane-1,3-diammonium (N-MPDA);[128] DJ4, 2-(dimethylamino)ethylammonium (DMEN);[129] DJ5, 3-(dimethylamino)-1-propylammonium (DMAPA);[129] DJ6, 4-(dimethylamino)butylammonium (DMABA);[129] DJ7, protonated thiourea cation;[130] DJ8, 2,2′-dithiodiethanammonium;[91, 131] DJ9, 2,2′-(ethylenedioxy)bis(ethylammonium) (EDBE);[132] DJ10, 2-(2-

ammonioethyl)isothiouronium;[133] DJ11, 2-methylpentane-1,5-diammonium;[121] DJ12, *N*-(aminoethyl)piperidinium;[97] DJ13, *N*-benzylpiperazinium;[134] DJ14, piperazinium;[134] DJ15, 3-(aminomethyl)piperidinium (3AMP);[69] DJ16, 4-(aminomethyl)piperidinium (4AMP);[69] DJ17, 1,4-bis(aminomethyl)cyclohexane;[135] DJ18, *m*-phenylenediammonium;[136] DJ19, histammonium (HA);[99] DJ20, 2-(ammoniomethyl)pyridinium;[137] DJ21, *N*,*N*-dimethyl-*p*-phenylenediammonium (DPDA);[138] DJ22, 1,4-phenylenedimethanammonium (PDMA);[139] DJ23, 4-amidinopyridinium;[140] DJ24, benzimidazolium;[141] DJ25, 1,5-diammoniumnaphthalene;[126] DJ26, 5,5′-bis(ammoniumethylsulfanyl)-2,2′-bithiophene (BAESBT);[142] DJ27, 5,5‴-bis(aminoethyl)-2,2′:5′,2″:5″,2‴-quaterthiophene (AEQT).[143]

3. Basic Optoelectronic Properties

In this section, we discuss some basic optoelectronic properties of 2D perovskites, including the electronic band structure, optical properties and charge transport dynamics.

3.1. Band Structure and Optical Properties

In the layer-structured 2D perovskites, the large-sized organic cation interlayers can limit charge carriers within a two-dimensional range. These interlayers also act as dielectric regulators, determining the electrostatic force on the electron-hole pairs.[144] The alternating arrangement of lead halide inorganic sheets and bulky organic interlayers results in a multiple-quantum-well (MQW) electronic structure (**Figure 5a**).[145] The high organic and inorganic dielectric contrast leads to a huge electron-hole binding energy (E_b) in 2D perovskites.[146] Time-resolved terahertz spectroscopy has verified that charge transport is preferred along the inorganic planes for prototypical 2D perovskites.[147] The excitons can be stabilized by 2D perovskite MQWs, even at ambient temperatures. Various possibilities based on the MQW structure make 2D perovskite an interesting material system for room-temperature photoelectric and fundamental physical applications.

The 2D confinement effect directly influences the bandgap (E_g) of 2D perovskite materials. For an RP hybrid perovskite, the E_g depends on the well width,[148] and the total E_g energy is determined by the base 3D structure and extra quantization energies of the electron and hole.[149] The optical E_g of $A'_2A_{n-1}B_nX_{3n+1}$ perovskite generally decreases as the n value increases. For example, the E_g value for $BA_2A_{n-1}Pb_nI_{3n+1}$ perovskites decrease with increased layer thickness from 2.24 eV ($n = 1$) to 1.52 eV ($n = \infty$) due to quantum-confinement effects associated with dimensional increase (**Figure 5b,c**).[150] The size and electronegativity of the halide and metal ions can also affect E_g, which increases as their size decreases. Pb has a lower Pauling electronegativity in comparison to Sn, so the Pb electronic states are higher in the band structure.[99] This flexibility of bandgap tuning, as well as composition tailoring for 3D/2D multi-dimensional perovskite, can facilitate various optoelectronic applications with targeted optical E_g materials.

Excitons have an essential influence on charge transport in semiconductors.[151] The 2D structure generally shows a large exciton binding energy (E_b) of several hundred meV (**Figure 5d**), which significantly enhances the interaction between electrons and holes compared to 3D perovskites.[152] For quasi-3D perovskites (i.e., 3D perovskite mixed with 2D perovskites), E_b is smaller and is comparable to 3D perovskites.[153] Because of this MQW band structure and large E_b values, low-n (e.g., $n < 5$) 2D perovskites often exhibit significant transport barrier across the adjacent 2D perovskite sheets. To address this challenge, various efforts have focused on controlling the growth of the inorganic perovskite framework perpendicular to the substrate to facilitate vertical charge transport for efficient charge collection in PV devices.[154-157]

Although the large E_b in low-n 2D perovskites may be detrimental for charge separation in solar cells, it can be beneficial for other optoelectronic applications beyond solar cells. For instance, the excitonic effect can significantly promote radiative recombination, which leads to higher photoluminescence quantum yield (PLQY) in perovskite-based LED devices, making them excellent candidates for high-efficiency LEDs. Additionally, the excitonic character in 2D perovskites also results in interesting and tunable exciton-phonon,[158] exciton-photon,[159] and exciton-exciton coupling,[160, 161] as well as the formation of self-trapped excitons (which leads to broadband emission) and many other paths for relevant optoelectronic applications.

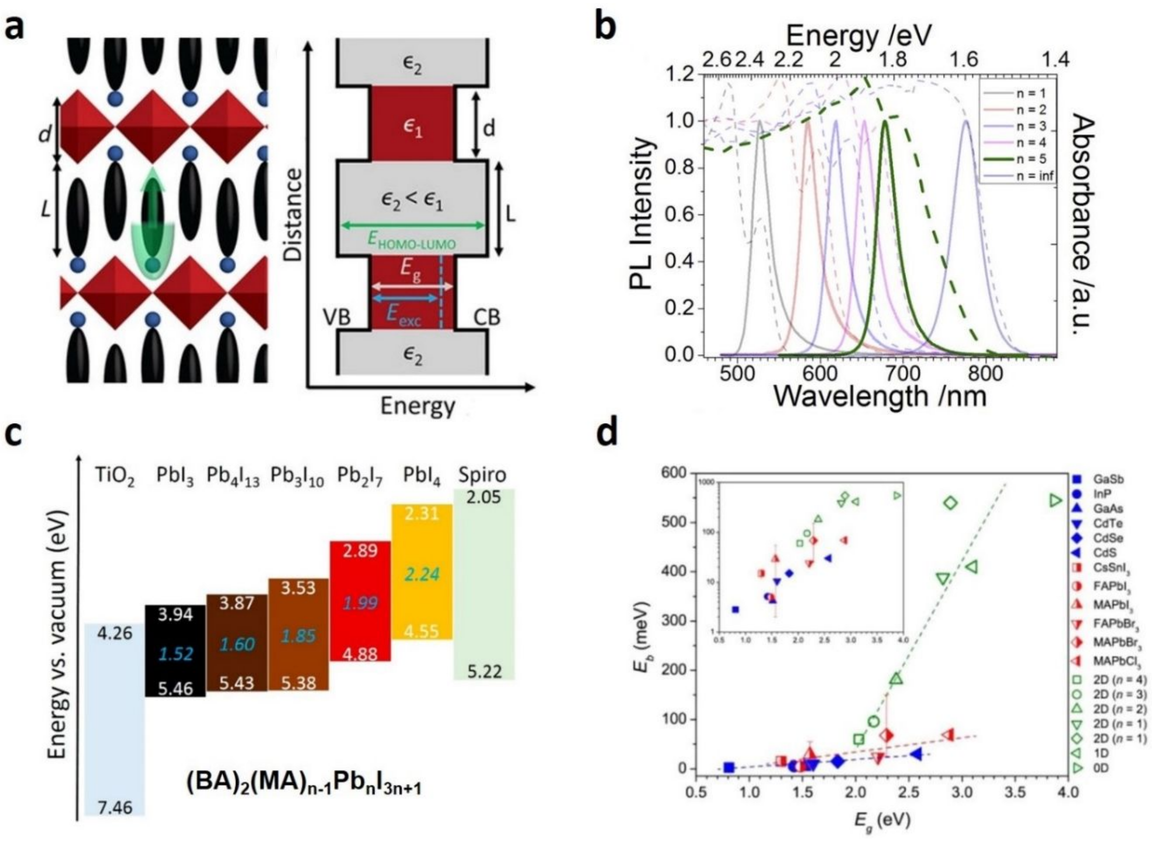

Figure 5. (**a**) Schematic of $n = 1$ 2D perovskite structure with alternating organic and inorganic sheets along with the corresponding MQW energy diagram (E_{exc} and E_{g} are the optical bandgap and electronic bandgap of the inorganic framework, respectively; organic cations have a larger HOMO–LUMO gap). The constant dielectric contrast (ε_1 and ε_2 for inorganic and organic layers, respectively) is also presented. Reproduced with permission from ref. 56. Copyright 2019, Wiley-VCH. (**b**) Typical optical emission and absorption spectra of $(BA)_2(MA)_{n-1}Pb_nI_{3n+1}$ perovskites. Reproduced with permission from ref. 79. Copyright 2017, Cell Publishing Group. (**c**) Band energy diagrams of $BA_2MA_{n-1}Pb_nI_{3n+1}$ perovskites. Reproduced with permission from ref. 150. Copyright 2014, ACS Publishing Group. (**d**) Comparison of the relationship between bandgap E_{g} and exciton binding energy E_{b} in various low-D and 3D perovskites. Reproduced with permission from ref. 152. Copyright 2016, ACS Publishing Group.

3.2. Charge-Transport Dynamics

The confining nature of 2D perovskite results in anisotropic conductivity and carrier mobility along various crystallographic directions. In general, when measured along the plane of the inorganic sheet, the conductivity and mobility are much better in comparison to that measured perpendicular to the sheets. The challenge of out-of-plane charge transfer is caused by the relatively high resistive, low mobility organic interlayer between adjacent higher mobility inorganic conductive sheets. In addition, the charge-transfer behavior of 2D perovskite also shows a strong dependence on the *n* value. In RP 2D perovskite films, the holes transfer from high-*n* QWs or the bulk to low-*n* phase along with electrons flowing in the opposite direction.[85, 162] An optimized *n* distribution of the QWs will enable more-efficient charge transfer across 2D structures with mixed *n* values. In addition, as the ratio of the number of inorganic perovskite plates per organic spacer increases, the mobility increases significantly as a continuous inorganic pathway is achieved. The orientation of the 2D perovskite layers is critical to the device performance: when the inorganic plates are arranged parallel to the charge-collection direction, better device performance can usually be obtained.

The charge-transport mechanism between inorganic layers has been proposed to be mediated by a tunneling process[163,164] with the organic molecules acting as barriers. Tunnel junctions have two key factors affecting charge transport: tunneling distance and barrier height. The latter is more complex and unpredictable than the former. The out-of-plane charge transport is generally believed to increase when the interlayer distance decreases,[164] although a systematic study is still absent from the literature. The tunneling barrier height can vary depending on the following two primary effects: 1) the intermolecular coupling between adjacent organic cations, and 2) the energy arrangement between the perovskite transport belt and the oxidation or reduction potential of organic cations.

Based on these considerations, we divide the strategies to improve charge transport of 2D perovskites into four parts: 1) process engineering (e.g., hot casting[154, 155] and solvent ratio tuning[165-169]); 2) additive engineering (e.g., NH_4SCN,[170, 171] NH_4Cl,[170] MACl,[172] PbI_2,[173] and HI[174]) to tune the orientation of 2D perovskite films; 3) engineering based on small cations (e.g., FA^+,[62, 175] MA^+, or Cs^+[156, 157]) to align perovskite 2D sheets and orientation of corresponding 2D perovskite films; and (4) engineering based on choice of bulky cations (e.g., F-PEA and MeO-PEA[106, 112, 114, 164, 176, 177]) to adjust the coupling between perovskite 2D sheets and the energy levels of organic layers. These strategies have been used mainly in low-*n* 2D perovskite in solar cells, and we discuss the details of how these strategies affect charge transport in the next section.

4. Application in Solar Cells

Here, we discuss the application of 2D perovskites in solar cells. This section is organized in four parts: 1) the application of low-*n* 2D ($n \leq 5$) perovskites as absorbers in devices; 2) 3D/2D mixed perovskites as absorbers in devices; 3) 2D perovskite as an interfacial layer on the bottom and top surface of 3D perovskite; and 4) Pb-free 2D perovskites as absorbers in devices.

4.1. 2D and Quasi-2D Perovskites with $n \leq 5$

4.1.1. Process Engineering

Although water (or moisture) is sometimes beneficial to device preparation, a humid environment is usually considered as a key factor that accelerates the degradation of PSCs under practical operation conditions.[150] In 2014, Karunadasa *et al.* demonstrated the first quasi-2D perovskites ($PEA_2MA_2Pb_3I_{10}$; $n = 3$) in mesoscopic PSCs. Although the cell efficiency (4.73%) was low at that time (**Table 1**), the quasi-2D perovskite film did show great promise regarding stability after 40 days of storage under ambient conditions with 52% relative humidity (RH), whereas the 3D counterpart degraded quickly within 4–5 days.[50]

The 2D perovskite film surface is normally rough, and there are many defects at the surface/boundary of 2D perovskites prepared with the normal one-step process due to the rapid crystallization process.[150, 153] In addition, charge transport is anisotropic for directions across and within the 2D sheets; thus, it is strongly affected by the crystal orientation relative to the substrate.[150] Tsai *et al.* first reported the hot-casting method for preparing 2D perovskite $(BA)_2(MA)_3Pb_4I_{13}$ ($n = 4$).[154] Interestingly, hot casting promoted the growth-oriented 2D perovskite films with the inorganic framework more aligned vertically to the substrate (**Figure 6a**), which would enable better pathways of charge transport. The corresponding 2D devices exhibited better stability compared to their 3D counterpart. The device performance was brought over 10% for the first time for 2D PSCs. Since this study, the hot-casting method has become a standard approach for preparing various 2D PSCs.[174, 178] However, this method is difficult as it requires precise control of the substrate temperature, which can then affect the batch-to-batch reproducibility. Gao *et al.* deposited the precursor solutions by a substrate-heated drop-casting method, which allowed self-assembly into uniform and oriented 2D-$(BA)_2(MA)_3Pb_4I_{13}$ ($n = 4$) perovskite films in air (**Figure 6b**), yielding PSCs with PCE of up to 14.9%.[179] Zhao *et al.* proposed a slow post-annealing (SPA) process for $BA_2MA_3Pb_4I_{13}$ ($n = 4$) 2D PSCs, and a favorable alignment of bandgap energy within 2D perovskite (from bottom ($n = 1$) to top ($n = \infty$)) was achieved due to gradients in vertical distribution of different perovskite phases after SPA. As a result, they obtained the champion performance of 17.26%.[180] Hu *et al.* reported another strategy by introducing a vacuum poling treatment to arrange different-*n*-value nanoplates and to enforce uniform nucleation during crystallization.[181] Using this approach, a PCE of 18.04% based on $(PEA)_2MA_4Pb_5I_{16}$ ($n = 5$) was demonstrated.

When 2D perovskite films are formed from the hot-casting process, heterogeneous nucleation mainly occurs at the gas/liquid interface, which helps to form a thin sheet-like capping layer on the outmost surface of the perovskite film. As a result, the rapid volatilization of DMF facilitates homogeneous nucleation, resulting in the formation of randomly oriented perovskite grains in the inner layer. To address this issue, Fan *et al.* fabricated the devices through mixed solvent engineering of DMF/DMSO, which improved PCE from ~6% (pure DMF) to ~11% (DMF/DMSO 1:3).[165] By using DMF/DMSO solvent engineering, the solvent volatilization process is used to modulate the crystallization process which makes the perovskite cover act as the seed—thus promoting the subsequent perovskite crystallization perpendicular to the inner layer of the perovskite film (**Figure 6c**). In another study, Huang *et al*. showed that specific solvents strongly affect the crystallization kinetics and crystal orientation of the resulting 2D perovskites by hot-casting.[166] Among several solvents, dimethylacetamide (DMAC) shows weak coordination to Pb and ammonium salts, suitable boiling point, and low polarity; thus, it is easy to remove during solution processing, and it can facilitate rapid crystallization of 2D perovskites. As a result of proper solvent selection, a PCE from 7.33% (from DMF) to 12.15% (from DMAC) was demonstrated.

For the anti-solvent method, the mechanism of formation are different according to Zhang's recent report.[167] The coordination strength of the solvent with perovskite precursor affects the formation of intermediate complexes and the subsequent growth of the 2D perovskite layer. Perovskite structure and intermediate complexes coexist after anti-solvent extraction and before thermal annealing of the DMF based precursor. During annealing, the existing perovskite and intermediate complex lead to different growth directions, which create structural mismatches and random boundaries. However, by using a mixed solvent (DMF/DMSO 5:5), only one intermediate complex is formed after anti-solvent extraction and before annealing. As a result, one direction of perovskite growth is enhanced and the 2D perovskites exhibit preferred orientation/alignment (**Figure 6d**). Consistent with the improved quality of the 2D perovskite films, the devices based on mixed solvents (DMF:DMSO, 5:5) also showed >80% performance improvement (from 6.78% to 12.29%) over those made with pure DMF by using the anti-solvent extraction method.

It is worth noting that at present, different reports often conclude different growth mechanisms, despite the reported use of the same growth methods. More detailed mechanistic studies are required to obtain a deeper, more actuate understanding of how the hot-casting or solvent processing routes impact the crystallization process.

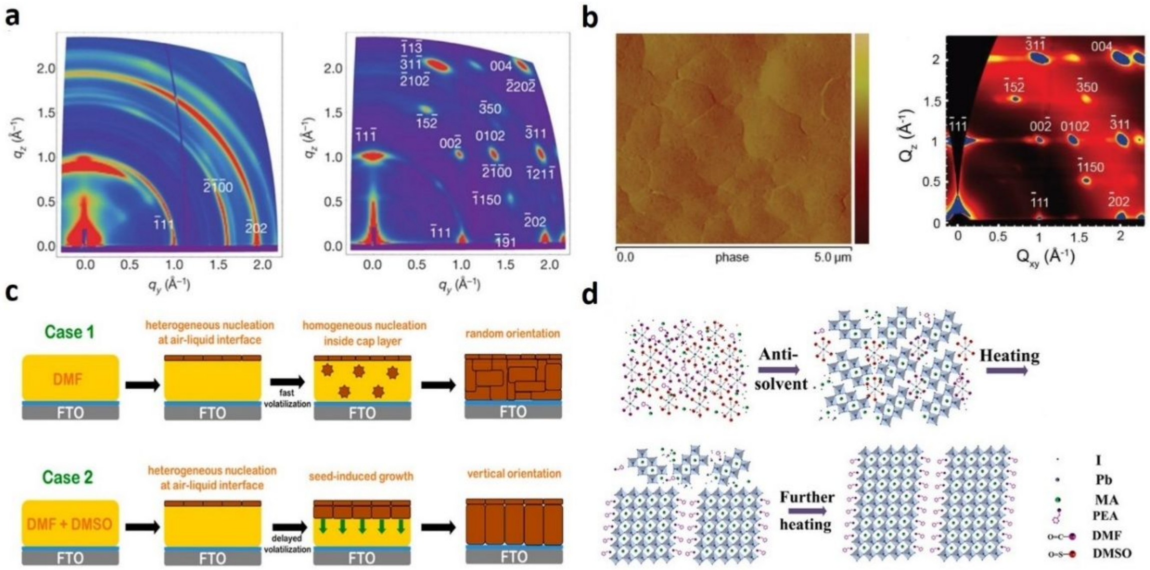

Figure 6. (**a**) Grazing-incidence wide-angle X-ray scattering (GIWAXS) comparison of room-temperature cast (left) and hot-cast (right) $(BA)_2(MA)_3Pb_4I_{13}$ perovskite films. X-ray scattering intensity is related to the color scale. Reproduced with permission from ref. 154. Copyright 2016, Nature Publishing Group. (**b**) Atomic force microscopy (AFM) phase images (left) and 2D GIWAXS pattern (right) of a drop-cast 2D-perovskite film prepared at 50 °C. Reproduced with permission from ref. 179. Copyright 2018, Wiley-VCH. (**c**) Schematics of the crystallization process using DMF solvent (case 1) and DMSO/DMF solvent (case 2). Reproduced with permission from ref. 165. Copyright 2019, ACS Publishing Group. (**d**) Schematics showing the effect of the mixed solvent DMSO:DMF (5:5) on 2D perovskite crystal growth. Reproduced with permission from ref. 167. Copyright 2019, Wiley-VCH.

Table 1. Representative 2D ($n \leq 5$) perovskite absorbers of PSCs based on process engineering.

Perovskite	Device Structure	PCE (%)	Stability	Year[Ref]
$PEA_2MA_2Pb_3I_{10}$ ($n = 3$)	Device A	4.73	N/A	2014[50]
$(BA)_2(MA)_3Pb_4I_{13}$ ($n = 4$)	Device B	12.52	100% of PCE after 2250 h, dark, 65% RH [a]	2016[150]
$(Gua)(MA)_3Pb_3I_{10}$ ($n = 3$)	Device B	16.65	84% of PCE after 2400 h, dark [b]	2019[178]

$(BA)_2(MA)_3Pb_4I_{13}$ ($n = 4$)	Device B with PEIE on PCBM and changing Al to Ag	14.9	N/A	2018[179]
$(BA)_2(MA)_3Pb_4I_{13}$ ($n = 4$)	ITO/PTAA/PVK/ C60/BCP/Ag	17.26	96% of PCE after 2000 h, dark [a]	2019[180]
$(PEA)_2MA_4Pb_5I_{16}$ ($n = 5$)	Device B with PEIE on PCBM and changing Al to Ag	18.04	96.1% of PCE after 8 months, dark [a]	2019[181]
$(BA)_2(MA)_3Pb_4I_{13}$ ($n = 4$)	Device A	11.8	90% of PCE after 30 days, dark, 60±5% RH [a]	2019[165]
$(BA)_2(MA)_3Pb_4I_{13}$ ($n = 4$)	Device B with LiF on PCBM.	12.15	85% of PCE after 330 h, dark, 60±5% RH [a]	2018[166]
$(PEA)_2MA_4Pb_5I_{16}$ ($n = 5$)	Device A	12.29	N/A	2019[167]
$(BA,Gua)_2MA_4Pb_5I_{16}$ ($n = 5$)	ITO/PCP-Na/PVK/ PCBM/BCP/Ag	15.86	91% of PCE after 700 h, dark, 55±5% RH [b]	2019[169]

Note:

[a] Encapsulated devices or non-encapsulated devices in Ar or N_2 atmosphere.

[b] Non-encapsulated devices in air.

RH: relative humidity. PVK: perovskite. PCP-Na: 3,3'-(2-([1,1'-biphenyl]-4-yl)-4Hcyclopenta[2,1-b:3,4-b']dithiophene-4,4-diyl)bis(propane-1-sulfonate)].

Device A: FTO/c-TiO_2/PVK/spiro-OMeTAD/Au.

Device B: ITO/PEDOT:PSS/PVK/PCBM/Al.

4.1.2. Additive Engineering

Additives can also assist the growth of vertically oriented 2D perovskite films.[170-173] Chen *et al.* first added ammonium thiocyanate (NH_4SCN) into a room-temperature, one-step, spin-coated process method.[171] After introducing the NH_4SCN, one can clearly observe vertical-oriented larger grains perpendicular to the substrate with almost no grain boundary, resulting in increased carrier lifetime and transport mobility, leading to improved efficiency and shelf life of the unencapsulated device. Later, they applied NH_4SCN to $(PEA)_2(MA)_4Pb_5I_{16}$ (n = 5) films, and the device performance improved from 0.56% to 11.01% due to the highly crystalline, vertically orientated 2D perovskite films (**Figure 7a**) and improved electron/hole transport.[182] With the cooperation of NH_4Cl and NH_4SCN to further enhance the crystallization and charge transport, PSC based on $(PEA)_2(MA)_4Pb_5I_{16}$ (n = 5) obtained an efficiency of 14.1%.[170]

In 3D PSCs, MACl is shown to slow down the speed of perovskite film formation and benefit the film coverage, resulting in much-improved performance.[183, 184] Chen *et al.* reported using a MACl-assisted method to prepare highly oriented 2D-perovskite $(ThMA)_2(MA)_2Pb_3I_{10}$ (n = 3) thin films, resulting in improved PCE from 1.74% to more than 15%.[185] After applying a MACl treatment, the 2D perovskite formed a unique nanorod-shape morphology, and showed a significant increase in crystal size, out-of-plane orientation (**Figure 7b**), and carrier lifetime. Other groups have reported similar phenomena.[186] PbI_2 as a typical Lewis acid can also form self-induced passivation in 2D-perovskite films with reduced surface defects.[173]

Chen *et al.* recently introduced a second spacer cation (SSC^+) approach by adding PEAI into the $BA_2MA_4Pb_5I_{16}$ (n = 5) perovskite precursor solution.[187] If PEAI is not added, a large number of the nuclei will precipitate from the precursor solution, resulting in small-grained perovskite films. However, after adding PEAI, the presence of precursor agglomerates may induce preferential nucleation and reduce the nucleation density, facilitating the formation of large grains (**Figure 7c**). This approach leads to the demonstration of a PCE of 14.09 % and ~10% degradation of an unsealed device after 1000-h air exposure. They also used Gua^+ as the SSC^+ and obtained a similar result in a follow-up study.[188]

Although using excessive additives can lead to better crystallinity, it also results in a large gap between grains, thus reducing the PV performance.[189] Chen *et al.* reported a sequential post-treatment process to make ACI 2D PSCs with high performance, where they sequentially used guanidinium thiocyanate (GuaSCN) and MACl as post-treatment agents (**Figure 7d**).[190] GuaSCN treatment has a significant effect on the perovskite morphology, leading to the fusion of segregated grains into dense and ordered grains. The trap state can be further passivated by subsequent MACl treatment; as a result, the performance is enhanced to 15.27% (**Table 2**).

Table 2. Representative 2D ($n \leq 5$) perovskite absorbers of PSCs based on additive engineering.

Type	**Perovskite**	**Device Structure**	**PCE (%)**	**Stability**	**Year[Ref]**
NH_4SCN	$(BA)_2(MA)_2Pb_3I_{10}$ (n = 3)	Device A	6.89	100% of PCE after 24 days, dark [a]	2017[171]
NH_4SCN	$(PEA)_2(MA)_4Pb_5I_{16}$	Device A	11.01	78.5% of PCE after 160 h,	2018[182]

	(n = 5)			dark, 55±5% RH [b]	
NH_4SCN +NH_4Cl	$(PEA)_2(MA)_4Pb_5I_{16}$ (n = 5)	Device A	14.1	>90% of PCE after 45 days, dark, 30% RH [b]	2018[170]
MACl	$(ThMA)_2(MA)_2Pb_3I_{10}$ (n = 3)	Device A	15.42	90% of PCE after 1000 h, dark [a]	2018[185]
PEAI	$BA_2MA_4Pb_5I_{16}$ (n = 5)	Device A	14.09	>90% of PCE after 1000 h, dark, 25±5% RH [b]	2019[187]
GuaI	$BA_2MA_4Pb_5I_{16}$ (n = 5)	Device A	16.26	94% of PCE after 1200 h, dark, 25±5% RH [b]	2019[188]
GuaSCN + MACl	$GAMA_4Pb_4I_{13}$ (n = 4)	Device A	15.27	75% of PCE for 480 h, dark, 50% RH [b]	2019[190]

Note:

[a] Encapsulated devices or non-encapsulated devices in Ar or N_2 atmosphere.

[b] Non-encapsulated devices in air.

RH: relative humidity. PVK: perovskite.

Device A: ITO/PEDOT:PSS/PVK/PCBM/BCP/Ag.

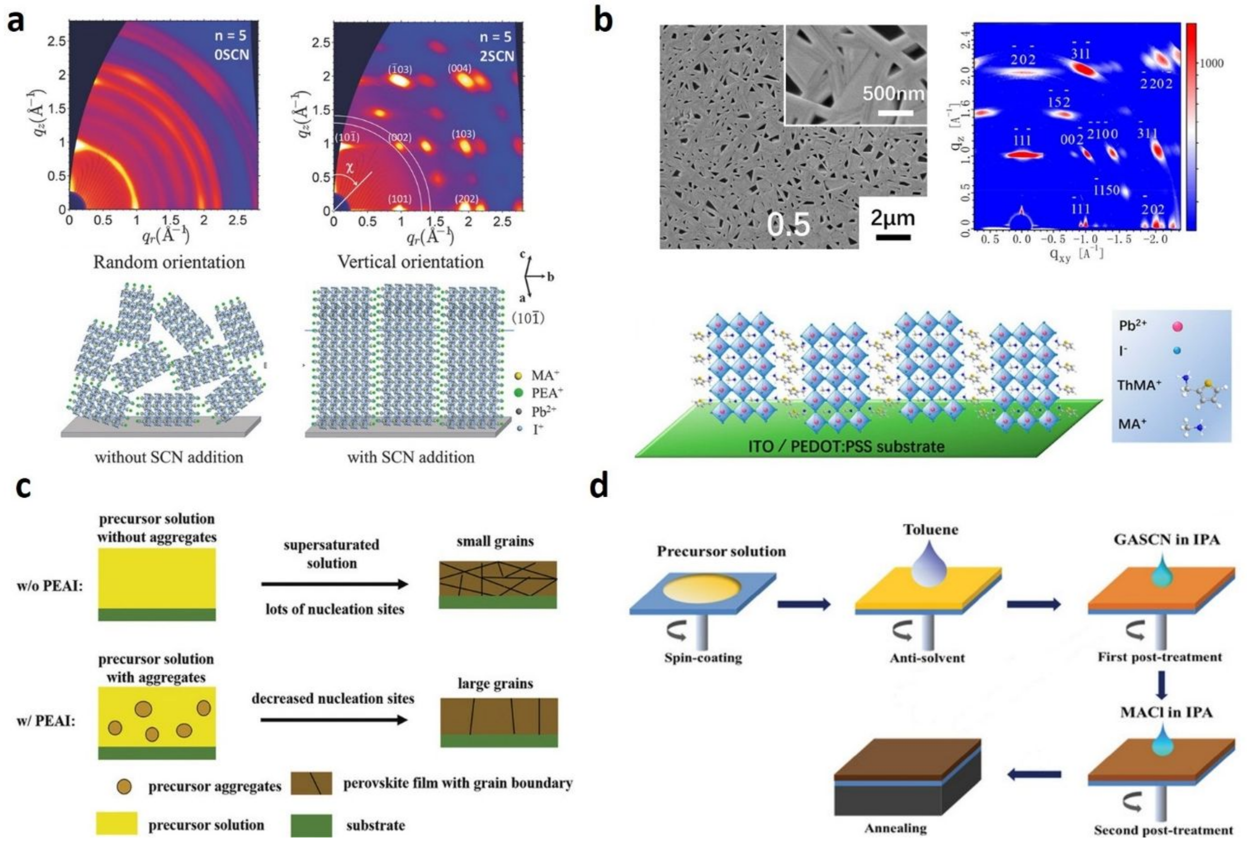

Figure 7. (**a**) GIWAXS patterns of perovskite films without (left) and with (right) addition of NH_4SCN in $(PEA)_2(MA)_4Pb_5I_{16}$ ($n = 5$). Schematic showing the effect of SCN additive on perovskite crystal orientation. Reproduced with permission from ref. 182. Copyright 2018, Wiley-VCH. (**b**) SEM images, GIWAXS results, and schematic of proposed packing structures of 2D $(ThMA)_2(MA)_2Pb_3I_{10}$ ($n = 3$) perovskite films with MACl. Reproduced with permission from ref. 185. Copyright 2018, ACS Publishing Group. (**c**) Illustration of the formation of the 2D perovskite film without or with PEAI addition by second spacer cation. Reproduced with permission from ref. 187. Copyright 2018, Wiley-VCH. (**d**) Schematic of sequential two-step post-treatment for $GuaMA_4Pb_4I_{13}$ film fabrication. Reproduced with permission from ref. 190. Copyright 2019, Wiley-VCH.

4.1.3. Small-Cation Engineering

Previous reports have shown that Cs^+ can effectively assist the crystallization of more stable 3D perovskite due to entropy gains if phase segregation is avoided.[191, 192] The surface morphology and apparent grain size of the 2D perovskite film are improved (**Figure 8a**) by replacing MA^+ with Cs^+ based on the hot-casting method,[156] thereby reducing the trap density, increasing the mobility of charge carriers, and improving the thermal stability. The enhanced film quality and the corresponding structural and optoelectronic properties significantly improved PCE from 12.3% to 13.68% (**Table 3**). Moreover, the 5% Cs^+-doped devices only exhibited a degradation of 11% from its initial PCE value after 1400-h air exposure with 30% RH.

It was further reported that incorporating a suitable amount of FA^+ can effectively control $BA_2(MA_xFA_{1-x})_3Pb_4I_{13}$ ($n = 4$) crystallization kinetics for enlarging crystal grains with increased crystallinity (**Figure 8b**), leading to high-quality films with limited nonoriented phases and reduced recombination centers.[62] *In-situ* photoluminescence (PL) techniques showed that the low-n-number 2D phase was formed early, then $n = \infty$ perovskite was eventually formed. After the introduction of 20% FA^+, the $BA_2(MA_{0.8}FA_{0.2})_3Pb_4I_{13}$ ($n = 4$) perovskite-based devices displayed the highest performance of 12.81%, resulting from enhanced carrier lifetime and crystal orientation. Ke *et al.* employed MA^+ and FA^+ cations in 3-(aminomethyl)piperidinium ($3AMP^{2+}$)-based 2D perovskite.[71] Single-cation $(3AMP)(MA)_3Pb_4I_{13}$ perovskite shows a wider bandgap, more distorted inorganic structure, and smaller Pb-I-Pb angles compared to that of mixed-cation $(3AMP)(MA_{0.75}FA_{0.25})_3Pb_4I_{13}$ perovskite. Adding a small amount of hydroiodic acid further improved film morphology, crystal quality, and vertical orientation, leading to the demonstration of 12.04%-efficient devices based on $(3AMP)(MA_{0.75}FA_{0.25})_3Pb_4I_{13}$ ($n = 4$).

Based on these findings, Zhang *et al.* first reported the use of mixed triple cations (MA^+, FA^+, and Cs^+) in fabricating 2D $BA_2(Cs_{0.02}MA_{0.64}FA_{0.34})_4Pb_5I_{16}$ ($n = 5$) perovskites.[175] Compared with the traditional MA-based counterparts, the use of these mixed triple cations leads to the film formation with smooth/dense surface morphology, bigger grain size, fewer grain boundary, and stronger crystallographic texture (**Figure 8c,d**). In addition, the corresponding perovskite films with the triple cations showed a longer carrier lifetime and higher conductivity. Compared with devices prepared by mono A-cation (MA^+), PCE of 2D $BA_2(Cs_{0.02}MA_{0.64}FA_{0.34})_4Pb_5I_{16}$ ($n = 5$) devices with triple cations increased from 7.80% to 14.23%. Recently, Zhou *et al.* also reported a similar effect and demonstrated a PCE of 15.58% based on $BA_2(MA_{0.76}FA_{0.19}Cs_{0.05})_3Pb_4I_{13}$ ($n = 4$) with 8.6% excess PbI_2.[157] The approach based on these triple cations is also found to be effective for mixed Pb/Sn perovskites $(BA)_2(FA_{0.85}Cs_{0.15})_3$ $(Pb_{0.6}Sn_{0.4})_4I_{13}$ ($n = 4$).[193]

Table 3. Representative 2D ($n \leq 5$) perovskite absorbers of PSCs based on small cations engineering.

Perovskite	**Device Structure**	**PCE (%)**	**Stability**	**Year[Ref]**
$(BA)_2(Cs_{0.05}MA_{0.95})_3Pb_4I_{13}$ ($n = 4$)	Device A	13.68	89% of PCE after 1400 h, dark, 30% RH [a]	2017[156]
$BA_2(MA_{0.8}FA_{0.2})_3Pb_4I_{13}$ ($n = 4$)	Device B	12.81	88% of PCE after 1300 h, dark, ~40%–60% RH [a]	2018[62]
$(3AMP)(MA_{0.75}FA_{0.25})_3Pb_4I_{13}$ ($n = 4$)	Device B with changing PCBM to C60	12.04	42% of PCE after 48 h, continuous light soaking [a]	2019[71]
$BA_2(Cs_{0.02}MA_{0.64}FA_{0.34})_4Pb_5I_{16}$ ($n = 5$)	Device A	14.23	74% of PCE after 600 h, dark, ~15%–20% RH [a]	2019[175]
$BA_2(MA_{0.76}FA_{0.19}Cs_{0.05})_3Pb_4I_{13}$ ($n = 4$)	Device B	15.58	80% of PCE after 1400 h, dark, 85 °C [b]	2019[157]
$(BA)_2(FA_{0.85}Cs_{0.15})_3(Pb_{0.6}Sn_{0.4})_4I_{13}$ ($n = 4$)	Device B	9.3	47% of PCE after 2000 h, dark [b]	2018[193]

Note:

[a] Non-encapsulated devices in air.

[b] Encapsulated devices or non-encapsulated devices in Ar or N_2 atmosphere.

RH: relative humidity. PVK: perovskite.

Device A: FTO/c-TiO_2/PVK/spiro-OMeTAD/Au.

Device B: ITO/PEDOT:PSS/PVK/PCBM/BCP/Ag.

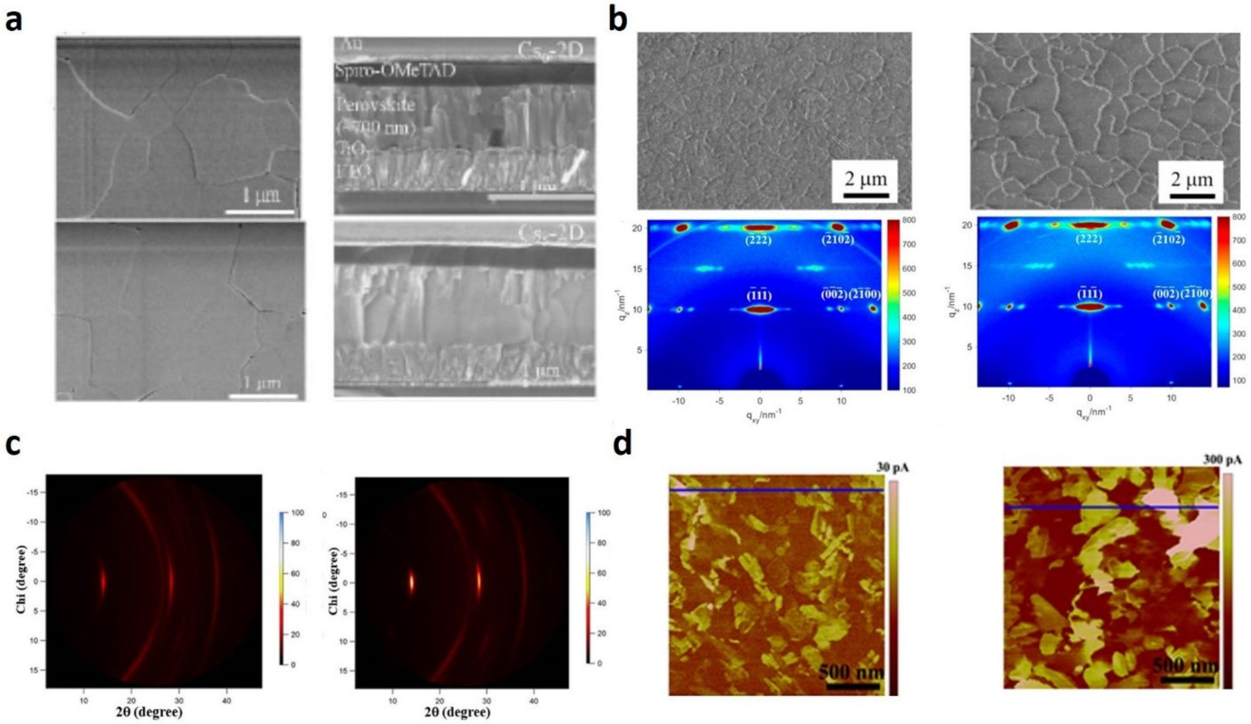

Figure 8. (**a**) Plan-view and cross-section view of scanning electron microscopy (SEM) images of $(BA)_2(Cs_{0.05}MA_{0.95})_3Pb_4I_{13}$ (n = 4) and $(BA)_2(MA)_3Pb_4I_{13}$ (n = 4) perovskite films. Reproduced with permission from ref. 156. Copyright 2017, Wiley-VCH. (**b**) SEM images and GIWAXS patterns of $(BA)_2(MA_{1-x}FA_x)_3Pb_4I_{13}$ films (x = 0, and 0.4). Reproduced with permission from ref. 62. Copyright 2018, ACS Publishing Group. (**c**) 2D XRD patterns and (**d**) conductive atomic force microscopy (C-AFM) imaging for the perovskite films of $BA_2MA_4Pb_5I_{16}$ (n = 5) (left) and $BA_2(Cs_{0.02}MA_{0.64}FA_{0.34})_4Pb_5I_{16}$ (n = 5) (right). Reproduced with permission from ref. 175. Copyright 2019, Wiley-VCH.

4.1.4. Bulky-Cation Engineering

Although PEA^+ and BA^+ represent the most commonly studied bulky cations so far, other large-sized organic cations have been incorporated into 2D perovskites and subsequently into solar cells. The suitability of a bulky cation includes its hydrogen-bonding capacity, stereochemical configuration, and space-filling ability.[65] Spin-orbit coupling and density functional theory (DFT) calculations indicated that the increased length of the barrier molecule would result in decreased electrical conductivity.[100] Moreover, it was shown that a better open-circuit voltage (V_{oc}) could be achieved when the charge is localized on the barrier molecule whereas a better current density was obtained when the charge is more delocalized.

Zhang *et al.* recently reported the application of F-PEA by introducing fluorine to the para position of PEA in 2D perovskites.[106] F-PEA can better align the stacking of perovskite sheets and decrease the average phenyl ring centroid–centroid distances in the organic layer, which would result in better interlayer electronic coupling and higher out-of-plane conductivity (**Figure 9a**). Using the anti-solvent deposition method at room temperature, the efficiency of 13.64% was achieved by $(\text{F-PEA})_2\text{MA}_4\text{Pb}_5\text{I}_{16}$ ($n = 5$)-based PSCs in the absence of any additives (**Table 4**). In addition, F-PEA-based 2D PSCs displayed improved thermal stability relative to PEA-based devices. The same results were later confirmed by other reports.[111, 112, 194] In another recent study, Wang *et al.* report a method of using 4-aminoethyl pyridine (4-AEP) as a bi-functional organic cation to adjust the crystallization rate of 2D perovskite.[195] 4-AEP not only can react with PbI_2 to form 2D perovskite but can also coordinate with Pb^{2+} (pyridyl unit) to slow down the crystallization rate, thus controlling the nucleation growth. As a result, the device based on $(\text{4-AEP})_2\text{MA}_4\text{Pb}_5\text{I}_{16}$ ($n = 5$) perovskite achieved a PCE of 11.68%, which is higher than that of PEA-based devices prepared under the same condition.

The bulky cations of DJ-phase perovskites with two amino groups can form a single layer with hydrogen bonds to the two neighboring inorganic sheets. This structural feature was shown to improve the material stability compared to RP-type perovskites (with a van der Waals gap).[74, 164] Kanatzidis *et al.* first reported PSCs based on DJ-phase perovskites (aminomethyl)piperidinium (3AMP) and 4-(aminomethyl)piperidinium (4AMP).[69] The Pb–I–Pb angles of 3AMP-based perovskite are bigger than that of perovskite based on 4AMP, indicating more orbitals overlap between the I p and Pb s,[196] thus resulting in a reduced bandgap (**Figure 9b**). The structural change also led to the difference in device performance. Specifically, devices based on 4AMP-based perovskite ($n = 4$) showed a lower PCE of 4.24% compared to 3AMP-based counterpart (7.32%); the higher performance associated with 3AMP largely results from the smaller bandgap and improved transport property. Later, Ma *et al.* proposed propane-1,3-diammonium (PDA) with reduced cation length to form 2D perovskites.[164] Compared to BA-based 2D perovskites, charge transport across neighboring inorganic perovskite layers are greatly enhanced. As a result, the corresponding devices achieved a high PCE of 13.0% with improved stability. Other bulky cations (e.g., (aminomethyl)pyridinium (4AMPY), (adamantan-1-yl)methanammonium (A), and 1,4-

phenylenedimethanammonium (PDMA)) are also reported as candidates to the DJ-type 2D perovskites.[71, 139, 177]

The ACI-type 2D perovskites adopt a larger crystal symmetry and different stacking, which can decrease the bandgap compared to RP perovskites with the same *n* values. Kanatzidis *et al.* reported the first ACI 2D perovskite $(Gua)(MA)_nPb_nI_{3n+1}$ (n = 1–3) along with the application in solar cells with a good performance of 7.26%.[72] Later, Zhao *et al.* compared anti-solvent and hot-casting methods to get more insight into the kinetic transformation process.[73] The formed intermediate phases, $(Gua)_2PbI_4$ perovskite, is critical to the subsequent transformation into $(Gua)(MA)_3Pb_3I_{10}$ (n = 3) perovskites. This material was able to achieve a PCE of 14.68% via use of an anti-solvent approach. MACl was later added to the precursor to further improve the $(Gua)(MA)_3Pb_3I_{10}$ (n = 3) films' morphology and QW's distribution (**Figure 9c**), resulting in the an impressive PCE (18.48%) for 2D PSCs.[51] 1,4-butanediamine (BEA) was used as a bulky organic cation to form a new type of 2D perovskite in which BEA^{2+} and MA^+ alternating cations are in the interlayer space (B-ACI) (**Figure 9d**), this combines advantages of DJ and ACI perovskites.[197] Devices based on $(BEA)_{0.5}MA_3Pb_3I_{10}$ perovskite reached a performance of 14.86%, which further increased to 17.39% by alloying with Cs, FA, and Br into the composition $((BEA)_{0.5}Cs_{0.15}(FA_{0.83}MA_{0.17})_{2.85}Pb_3(I_{0.83}Br_{0.17})_{10})$.

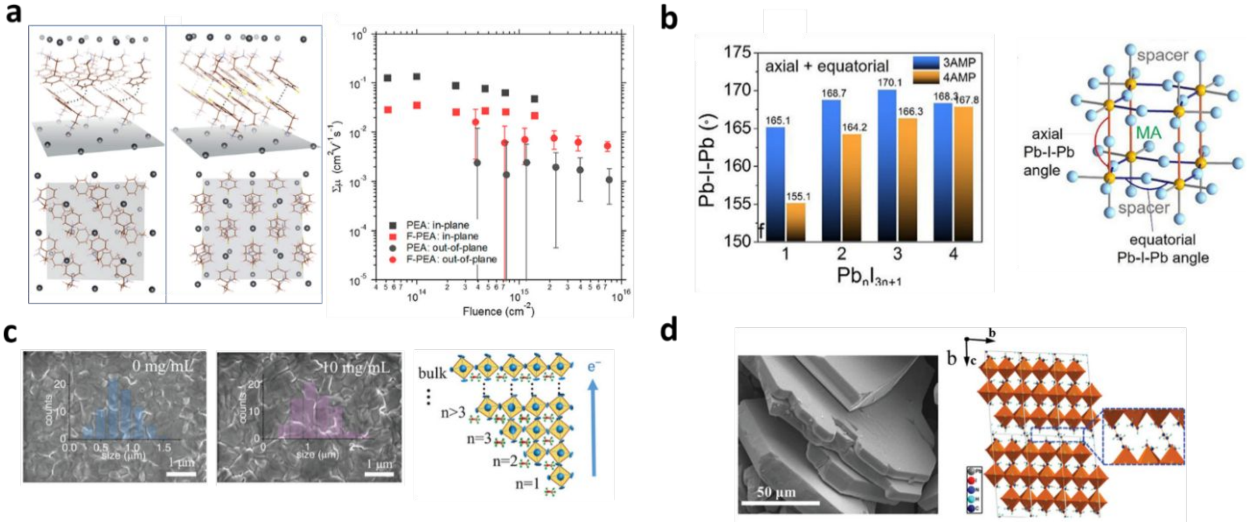

Figure 9. (**a**) The structures of n = 1 2D perovskites $(PEA)_2PbI_4$ (left) and $(F\text{-}PEA)_2PbI_4$ (right) along with time-resolved microwave conductivity results of transport across and within the 2D sheets. Reproduced with permission from ref. 106. Copyright 2019, ACS Publishing Group. (**b**) Average axial and equatorial

angles of (4AMP)PbI$_4$ and (3AMP)PbI$_4$ along with the definitions of the respective axial and equatorial Pb-I-Pb angles. Reproduced with permission from ref. 69. Copyright 2018, ACS Publishing Group. (**c**) Top-view SEM images of (Gua)(MA)$_3$Pb$_3$I$_{10}$ (n = 3) films without and with MACl additive along with an illustration of different n distribution of QWs and n-dependent electron flow direction. Reproduced with permission from ref. 51. Copyright 2019, Wiley-VCH. (**d**) SEM image and crystal structures of (BEA)$_{0.5}$MA$_3$Pb$_3$I$_{10}$ perovskite with alternating BEA^{2+} and MA$^+$ cations in the interlayer space. Reproduced with permission from ref. 197. Copyright 2019, Wiley-VCH.

Table 4. Representative 2D ($n \leq 5$) perovskite absorbers of PSCs based on bulky cations engineering.

Perovskite	**Device Structure**	**PCE (%)**	**Stability**	**Year[Ref]**
(F-PEA)$_2$(MA)$_4$Pb$_5$I$_{16}$ (n = 5)	Device A with m-TiO$_2$ on c-TiO$_2$	13.64	65% of PCE after 76 h, dark, 70 °C [a]	2019[106]
F-PEA$_2$MA$_2$Pb$_3$I$_{10}$ (n = 3)	FTO/NiO$_x$/PVK/PC$_{61}$BM/BCP/Ag	5.83	N/A	2019[111]
(F-PEA)$_2$(MA)$_4$Pb$_5$I$_{16}$ (n = 5)	Device B with changing C60 to PCBM	14.5	90% of PCE after 40 days, dark, 40%–50% RH [a]	2019[112]
(4-AEP)$_2$MA$_4$Pb$_5$I$_{13}$ (n = 5)	Device A with changing c-TiO$_2$ to C$_{60}$	11.68	95% of PCE after 1000 h, dark, 30% RH [a]	2019[195]
(3AMP)(MA)$_2$Pb$_3$I$_{10}$ (n = 3)	Device B with changing ITO to FTO	7.32	N/A	2018[69]
PDAMA$_3$Pb$_4$I$_{13}$ (n = 4)	Device B	13.0	90% of PCE after 1000 h, dark, 85% RH [b]	2018[164]
(3AMPY)(MA)$_3$Pb$_4$I$_{13}$ (n = 4)	Device B with changing Ag to Al	9.2	N/A	2019[71]
A$_2$FA$_2$Pb$_3$I$_{10}$ (n = 3)	Device A with m-TiO$_2$ on c-TiO$_2$	7.8	84% of PCE after 800 h, MPPT, continuous light soaking [a]	2019[177]
(Gua)(MA)$_3$Pb$_3$I$_{10}$ (n = 3)	Device B with changing Ag to Al and C60/BCP to PCBM	7.26	N/A	2017 [72]
(Gua)(MA)$_3$Pb$_3$I$_{10}$ (n = 3)	Device A (changing spiro-OMeTAD to PCBM)	16.48	88% of PCE after 240 days, dark, 30%–40% RH [a]	2019[73]
(Gua)(MA)$_3$Pb$_3$I$_{10}$ (n = 3)	Device A	18.48	95% of PCE after 131 days, dark, 30–40% RH [b]	2019[51]

$(BEA)_{0.5}Cs_{0.15}(FA_{0.83}MA_{0.17})_{2.85}Pb_3(I_{0.83}Br_{0.17})_{10}$ (n = 3)	Device A	17.39	93% of PCE after 500 h, continuous light soaking [a]	2019[197]

Note:

[a] Non-encapsulated devices in air.

[b] Encapsulated devices or non-encapsulated devices in Ar or N_2 atmosphere.

RH: relative humidity. PVK: perovskite.

Device A: FTO/c-TiO_2/PVK/spiro-OMeTAD/Au.

Device B: ITO/PEDOT:PSS/PVK/C60/BCP/Ag.

4.2. 3D/2D Mixed Perovskite

The pure 2D (n = 1) PSCs do not exhibit efficiencies as high as 3D PSCs due to their larger bandgaps and restricted transport across the organic spacer layers. In contrast, 3D/2D multidimensional perovskites formed by incorporating 2D perovskites into 3D perovskites (using bulky cations to replace small amounts of organic cations in the precursor solution) has recently appeared to be a promising approach to balance good device performance with long-term operational stability.[198]

Based on the previous report of better stability of low-n 2D perovskites,[50] Yao *et al.* reported a facile two-step method to form uniform, compact $(MAPbI_3)_{1-x}[(PEI)_2PbI_4]_x$ 3D/2D perovskite films. By spin-coating an initial PbI_2 and polyethylenimine hydriodide (PEI·HI) mixed solution, then coated with a CH_3NH_3I layer to produce a film.[199] The *in-situ*-formed $(PEI)_2PbI_4$ incorporation was shown to retard perovskite growth and promote the formation of a continuous uniform film, and the formation of 3D perovskite crystals with domains hindered by increasing the number of 2D materials. A champion PCE of 15.2% was obtained from this approach for a $(MAPbI_3)_{0.98}[(PEI)_2PbI_4]_{0.02}$ film and displayed better humidity stability than the reference 3D $MAPbI_3$-based devices (**Table 5**).

Park *et al.* used a small amount of PEAI to fabricate $(PEA_2PbI_4)_{0.017}(MAPbI_3)_{0.983}$ PSCs, and the devices showed comparable performance and better stability compared to that of $MAPbI_3$-based devices. However, the small amount of incorporated PEA_2PbI_4 still resulted in a lower short-circuit current density (J_{sc}) than that of $MAPbI_3$-based devices.[200] Later, by applying AVA_2PbI_4 into a printable $MAPbI_3$-based mesoporous HTM-free device, Nazeeruddin *et al.* demonstrated a performance of 11.2% by $(AVA_2PbI_4)_{0.03}(MAPbI_3)_{0.97}$ on a 10×10 cm^2 module; the device exhibited no degradation in performance after testing for >10,000 h under continuous illumination at 55°C.[52] FA- and Cs-based perovskites generally exhibit better stability than MA-based ones for 3D perovskites.[31] Based on this consideration, Snaith *et al.* introduced BA^+ into a mixed-cation 3D $FA_{0.83}Cs_{0.17}Pb(I_yBr_{1-y})_3$ perovskite.[55] They found the formation of 2D perovskite flakes scattered among highly oriented 3D perovskite grains; these 2D perovskite structures significantly reduced nonradiative charge recombination (**Figure 10a**). As a result, a $BA_{0.05}(FA_{0.83}Cs_{0.17})_{0.95}Pb(I_{0.8}Br_{0.2})_3$-based PSC was achieved with a PCE of 20.6%. The energetic alignment across the 3D/2D interface is found to be similar to a standard type-I or type-II heterojunction due to the wider bandgap of 2D perovskite.[124, 201] By further increasing ratios of BA^+ cations and Br anions, $BA_{0.09}(FA_{0.83}Cs_{0.17})_{0.91}Pb(I_{0.6}Br_{0.4})_3$ perovskite was developed with enhanced device stability; the corresponding devices showed only 20% performance degradation after 1000 h in air and almost 4000 h with encapsulation under light illumination. A similar trend was also observed with other bulky salts, such as (2-chloroethylamine (CEA^+), 2-thiophenemethylammonium (ThMA) and dimethylamine (DMA).[202-209]

Ammonium salts containing a short-branched chain than commonly used PEA^+ and BA^+ may exhibit better charge-transport properties when used in 2D perovskites. Lioz Etgar *et al.* introduced 1,4-benzenedimethanamonium iodide (BzDAI) with a relatively short length and aromatic ring with free π-electrons to enhance the charge transport.[210] The PSCs with $(BzDA)(Cs_{0.05}MA_{0.15}FA_{0.8})_9Pb_{10}(I_{0.93}Br_{0.07})_{31}$ ($n = 10$) achieved an efficiency of 15.6%, and the devices also exhibited better stability under humidity and illumination. Some other bulky cations (e.g., carbazole alkylammonium iodide derivative (CAI) and phenyltrimethylammonium (PTA)) also showed the same trend.[98, 120, 211]

Using bulky, large-sized organic halide salts (e.g., BAI and PEAI) has been shown to reduce the defect density of 3D perovskites. However, the formation of RP-type 2D perovskites within these structures could reduce J_{sc} of devices due to quantum-confinement effects. Recently, addition of guanidinium cations (Gua^+) have been reported to form highly stable 3D crystalline structures to improve the solar cell performance for $MAPbI_3$- or $FAPbI_3$-based PSCs.[212-217] In another study, a large Gua cation was incorporated into $Cs_{0.1}(FA_{0.83}MA_{0.17})_{0.9}Pb(I_{0.83}Br_{0.17})_3$ perovskites to form $Gua_x(CsFAMA)_{1-x}$ mixed-cation perovskites.[218] The color of the corresponding perovskite films changed from black for 0% Gua^+ to brown for 40% Gua^+ (**Figure 10b**). Incorporation of 10% Gua^+ resulted in the best device performance (PCE of 21.12%) with higher carrier lifetime and lower trap density due to the strong passivation from the Gua^+ additive.

In addition to increasing the stability against heat and moisture, the use of 2D perovskite is also often reported as an effective additive for phase stabilization in inorganic $CsPbI_3$[155, 219-221] or $FAPbI_3$,[222-224] which are known to have phase instabilities with respect to the α-to-δ phase transition at room temperature. Zhang *et al*. recently demonstrated the use of a small amount of 2D $EDAPbI_4$ (ethylenediamine, EDA) perovskite into the $CsPbI_3$ perovskite to significantly enhance the phase stability of α-$CsPbI_3$.[220] Following this preparation approach, the apparent grain size of $CsPbI_3{\cdot}x EDAPbI_4$ decreased with increasing $EDAPbI_4$ content and the number of pinholes was much reduced (**Figure 10c**), resulting in the all-inorganic PSC with a PCE of 11.8%. Other studies have also shown enhanced phase stability of $CsPbI_3$ PSCs by using other 2D perovskite additives.[155, 221] These results show that the construction of quasi-2D or 3D/2D mixed perovskites represents an effective approach to enhance phase stability of inorganic $CsPbI_3$ perovskite.

$FAPbI_3$ is another well-known perovskite composition that also has a significant phase-stability issue. Adding a small amount of Cs^+ to $FAPbI_3$ to form $CsFAPbI_3$ is one effective way to improve the phase stability by tuning the tolerance factor;[27] however, it generally widens the bandgap, leading to a reduction of J_{sc}. Incorporating a certain amount of 2D $BA_2Pb(I/Br)_4$ into the perovskite precursor facilitates the formation of phase-pure FA-based perovskite. Further passivation of grain boundaries by semiconducting molecules with Lewis base groups significantly improved charge-carrier dynamics, leading to devices with PCE of 20.62% and improved stability.[224] The benefits of incorporating PEA^+-based 2D structures into 3D perovskites were also reported by other groups.[222, 223] Complementary additives PEAI and $Pb(SCN)_2$ were used to improve a wide-bandgap (1.68-eV) PSC with an efficiency of ~20%.[22] Tong *et al*. applied GuaSCN to low-bandgap Sn-Pb mixed-perovskite thin films to improve their structural and optoelectronic properties resulting from the formation of a 2D structure at grain boundaries (**Figure 10d**).[54] New strategies to "design" 2D-PPAs with enhanced charge transport are necessary for further advancing efficient and stable 2D-PPA based-3D PSCs.

Table 5. Representative 3D/2D mixed-perovskite absorbers of perovskite solar cells.

Perovskite	**Device Structure**	**PCE (%)**	**Stability**	**Year[Ref]**
$(MAPbI_3)_{0.98}[(PEI)_2PbI_4]_{0.02}$	ITO/PEDOT:PSS/PVK/$PC_{61}BM$/LiF/Ag	15.2	84% of PCE after 14 days, dark, 50% RH [a]	2015[199]
$(DA_2PbI_4)_{0.05}MAPbI_3$	ITO/TiO_2/PVK/spiro-OMeTAD/MoO_3/Ag	19.05	80% of PCE after 60 days, dark [b]	2019[225]
$(PEA_2PbI_4)_{0.017}(MAPbI_3)$	FTO/c-TiO_2/m-TiO_2/PVK/spiro-OMeTAD/Ag	19.84	96% of PCE after 100 h, dark [a]	2019[200]
$(AVA_2PbI_4)_{0.03}(MAPbI_3)_{0.97}$	FTO/TiO_2/ZrO_2/PVK/C	10.10	100% of PCE after10,000 h, 55°C, continuous light soaking [b]	2017[52]
$BA_{0.09}(FA_{0.83}Cs_{0.17})_{0.91}Pb(I_{0.6}Br_{0.4})_3$	FTO/SnO_2/$PC_{61}BM$/PVK/spiro-OMeTAD/Au	17.2	80% of PCE after 1000 h, air, dark [a]	2017[55]
$(BzDA)(Cs_{0.05}MA_{0.15}FA_{0.8})_9Pb_{10}(I_{0.93}Br_{0.07})_{31(n=10)}$	FTO/c-TiO_2/m-TiO_2/PVK/spiro-OMeTAD/Au	15.6	80% of PCE after 84 h, dark, 20%–50% RH [a]	2019[210]
$CA_2MA_{39}Pb_{40}I_{121(n=40)}$	ITO/SnO_2/PVK/spiro-OMeTAD/Au	6.6	59% of PCE after 264 h, dark, 77% RH [a]	2018[120]
$Gua_{0.1}[Cs_{0.1}(FA_{0.83}MA_{0.17})_{0.9}]_{0.9}Pb(I_{0.83}Br_{0.17})_3$	ITO/SnO_2/PVK/spiro-OMeTAD/MoO_3/Ag	21.12	N/A	2019[218]

Note:

[a] Non-encapsulated devices in air.

[b] Encapsulated devices or non-encapsulated devices in Ar or N_2 atmosphere.

RH: relative humidity. PVK: perovskite.

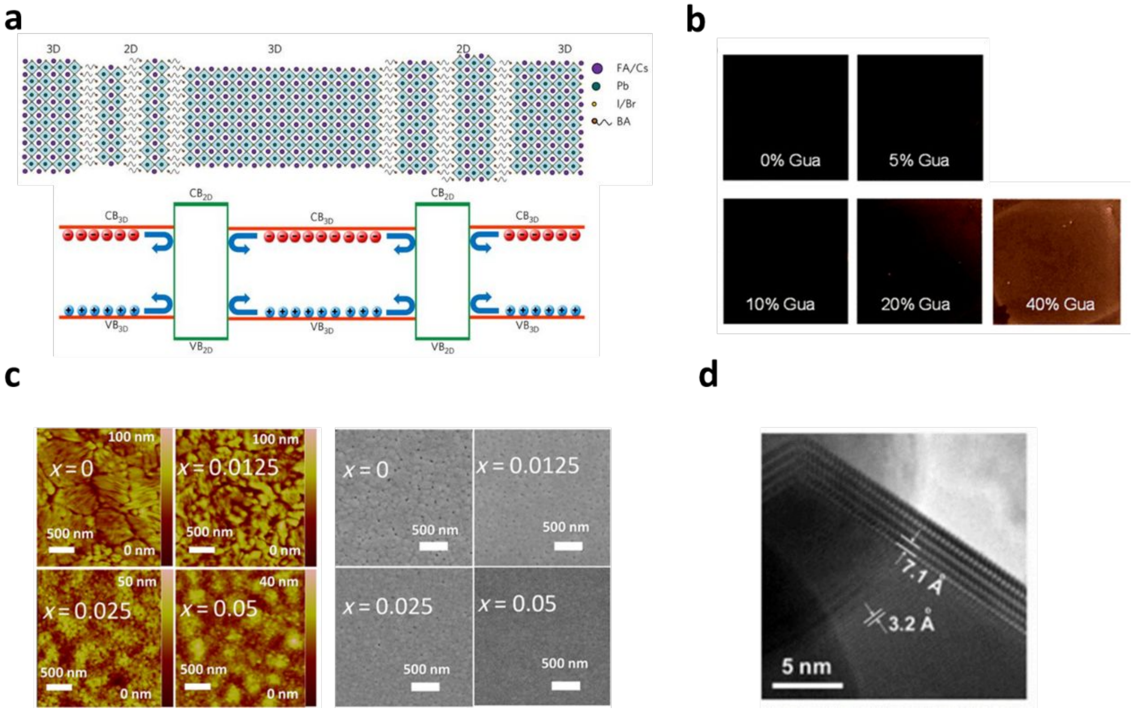

Figure 10. (**a**) Schematic of self-assembled 3D/2D perovskite structure along with the electronic band structures (VB: valence band; CB: conduction band). Reproduced with permission from ref. 55. Copyright 2017, Nature Publishing Group. (**b**) Photographs of perovskite films prepared with different molar ratio of Gua. The pristine perovskite composition is $Cs_{0.1}(FA_{0.83}MA_{0.17})_{0.9}Pb(I_{0.83}Br_{0.17})_3$. Reproduced with permission from ref. 218. Copyright 2019, Royal Society of Chemistry. (**c**) AFM (left) and SEM (right) images of $CsPbI_3{\cdot}x EDAPbI_4$ (x values indicated) perovskite films. Reproduced with permission from ref. 220. Copyright 2017, American Association for the Advancement of Science (AAAS). (**d**) High-resolution transmission electron microscopy (HRTEM) image of the perovskite grain-boundary region with 7% GuaSCN additive. The pristine perovskite composition is $(FASnI_3)_{0.6}(MAPbI_3)_{0.4}$. Reproduced with permission from ref. 54. Copyright 2019, American Association for the Advancement of Science (AAAS).

4.3. Interface Modification with 2D Perovskites

A 2D perovskite thin layer can also be added to the top of a 3D perovskite absorber as an interfacial layer between the perovskite absorber and charge-transport/contact layer; this interfacial engineering was also shown to improve the perovskite absorber layer with lower defect densities and longer carrier lifetimes.[226] The 2D interfacial layer is usually processed by spin coating an isopropanol (IPA) solution containing long-chain alkyl-ammonium halides on top of a 3D perovskite involving a cation exchange reaction. The 2D perovskite interfacial layer is expected to enhance moisture resistance and reduce surface defects by combining large hydrophobic cations with effective charge-transfer properties.[227] In addition, Herz *et al.* found that the blue-shift emission from the quasi-2D region overlaps the absorption spectrum of 3D perovskite, which leads to efficient heterogeneous photon recovery.[228]

Structural analysis has been commonly used to verify the formation of the 2D perovskite structure on top the 3D perovskite absorber in a device stack. Nazeeruddin *et al*. demonstrated the layered 2D perovskite PEA_2PbI_4 with distinct X-ray diffraction (XRD) features on top of the 3D $Cs_{0.1}FA_{0.74}MA_{0.13}PbI_{2.48}Br_{0.39}$ perovskite films (**Figure 11a**).[229] When incorporating the PEA_2PbI_4 perovskite top layer, the PSCs exhibit a higher PCE of 20.1% (**Table 6**). In addition, the devices exhibited less than 15% of performance degradation under ambient illumination at 50°C over 800 h. Other groups also reported similar results of PEAI.[230-232] Based on the application of PEAI, Grätzel *et al.* recently introduced five fluorine atoms to PEAI forming pentafluorophenylethylammonium iodide (F5PEAI) and applied its IPA solution for the post-growth treatment of the 3D perovskite absorber.[233] The X-ray photoelectron spectroscopy (XPS) depth profiling of fluorine (F) and X-ray reflectivity (XRR) peak width (**Figure 11b**) established the presence of ~8–9-nm 2D perovskite on the top. The 2D layer also enhances interfacial charge collection and enables the device performance of >22%. Unencapsulated PSCs only showed 10% degradation after 1000 hours under ambient illumination.

Seo *et al.* reported the use of a mixed solvent (*o*-dichlorobenzene:IPA = 97:3, v/v) containing n-hexyl trimethyl ammonium bromide (HTAB) solution and spin-coated on top of the 3D perovskite surface to form a wide-bandgap perovskite layer, which is confirmed by HRTEM of the device cross-section near the interface region (**Figure 11d**).[21] The HTAB molecule comprises a functionalized moiety ($N^+(CH_3)_3^-$) and an aliphatic moiety ($C_6H_{13}^-$). The $C_6H_{13}^-$ could form van der Waals interactions between the perovskite and organic HTM, which would promote the self-assembly of P3HT. As a result, they attained a PCE of 23.3%, and the encapsulated devices maintained more than 95% of their initial PCE for 1370 h with maximum power-point tracking (MPPT) under continuous light soaking at room temperature. Some other organic cations, with optimized concentration, have also shown similar results with enhanced stability and efficiency; these organic cations include BAI,[226] cyclopropylammonium iodide (CAI),[234] octylammonium iodide (OAI),[226, 235] dodecylammonium iodide (DAI),[235] 5-ammonium valeric acid iodide (5-AVAI),[236] n-butylammonium bromide (BABr),[237] long-chain aliphatic alkylammonium chloride

($C_mH_{2m+1}NH_3Cl$, $m = 8, 10, 12$),[238] and 3-(nonafluoro-tert-butyloxy)propylamine hydroiodide (A43).[239]

For the pure 2D perovskite, many achievements have been made in determining the properties of the films, such as charge transfer between QW and *n*-layer distribution.[162, 240] However, the influence of the cationic chemical dependence of 2D/3D heterostructures on charge collection and final PV performance has not been fully developed. This is important for ensuring effective charge extraction from the 2D interfacial layer. Along this direction, Liu *et al.* conducted a study to deepen the understanding of how interface engineering or composition adjustment can affect the 2D and 3D interface in $FAPbI_3$-based solar cells (**Figure 11c**).[25] They found that better QW distribution with faster charge-transfer mechanics can improve carrier mobility and charge collection and can reduce recombination. The 2D/3D film based on PEA:FA (1:1) achieves a balance between charge transport within QWs and passivation at the 2D/3D heterojunction, resulting in an efficiency of 21.15%, which is significantly higher than that of the 3D counterpart (19.02%). In addition to the performance improvement, the device also displayed impressive long-term environmental stability. A similar effect was also found in the PEAI-treated $MAPbI_3$ devices.[241]

So far, most studies have focused on the structure and optoelectronic properties of the 2D perovskite layer. Bawendi *et al.* recently pointed out that the deposition method is a critical factor for manufacturing high-efficiency 2D/3D PSCs.[242] In this study, the precursor and solvent (linear alkylammonium bromide/chloroform) were combined as a selective precursor dissolution strategy to effectively form a transparent 2D perovskite layer onto the 3D perovskite thin film. This strategy passivated defects, resulting in improved carrier lifetime and V_{oc}. As a result, they obtained a champion PCE of 23.4% with a certified stabilized PCE of 22.6% based on *n*-hexylammonium bromide (C_6Br).

Treatment of ammonium salt or derivatives to 3D perovskite films could lead to the formation of an organic cation layer rather than a 2D capping layer; these organic cations could also passivate defects and improve the performance of PSCs. Some additional candidates include octylammonium iodide (OAI),[243] tetra-ethyl ammonium (TEA),[244] mixed hydroiodic acid and oleylamine (OLA-HI),[245] MABr/FAI,[246] choline iodine (CHI),[247] PEAI,[13, 248] phenyltrimethylammonium bromide (PTABr),[249] and GuaBr.[250] The underlying mechanisms are still not known as to why some cations can form 2D capping layer under particular process conditions whereas some cannot; however, several reports have clear evidence (2D XRD, GIWAXS, SEM, or HRTEM) to support the formation of a 2D perovskite layer on 3D perovskite.[21, 25, 226, 229, 237, 242]

It is challenging to realize the formation of a 2D capping layer for all-inorganic Cs-based perovskites. To address this challenge, Lin *et al.* demonstrated an *in-situ* growth method to form 2D/3D heterostructured on inorganic $CsPbI_2Br$ perovskite.[251] By adding some DMSO in the alkyl-ammonium halide IPA solutions to tune the conversion process, they were able to demonstrate a type-Ⅱ heterojunction between the 2D and 3D perovskites, which resulted in enhanced hole collection and reduced carrier recombination. As a result, both device performance and stability against humid environment were improved compared to the control device without the 2D perovskite surface treatment.

Thus, forming a 2D capping layer or just an organic cation layer can passivate surface defects (and possibly bulk defects); but it also can form a heterojunction to decrease nonradiative recombination and enhance charge-carrier separation. The energy offset at the heterojunction may also produce an energy barrier hindering charge transfer across the 2D/3D heterojunction. More studies should focus on developing the synthesis control to form a transparent 2D capping layer with controlled energy levels and/or the layer thickness (i.e., *n* value) of the 2D structures.[197, 252] Design of new bulky organic cations that could form stable 2D structures with enhanced plane-to-plane charge transport along with new ways to control the 2D structure/composition will further advance the performance and stability of 2D-modified 3D PSCs.[106, 175]

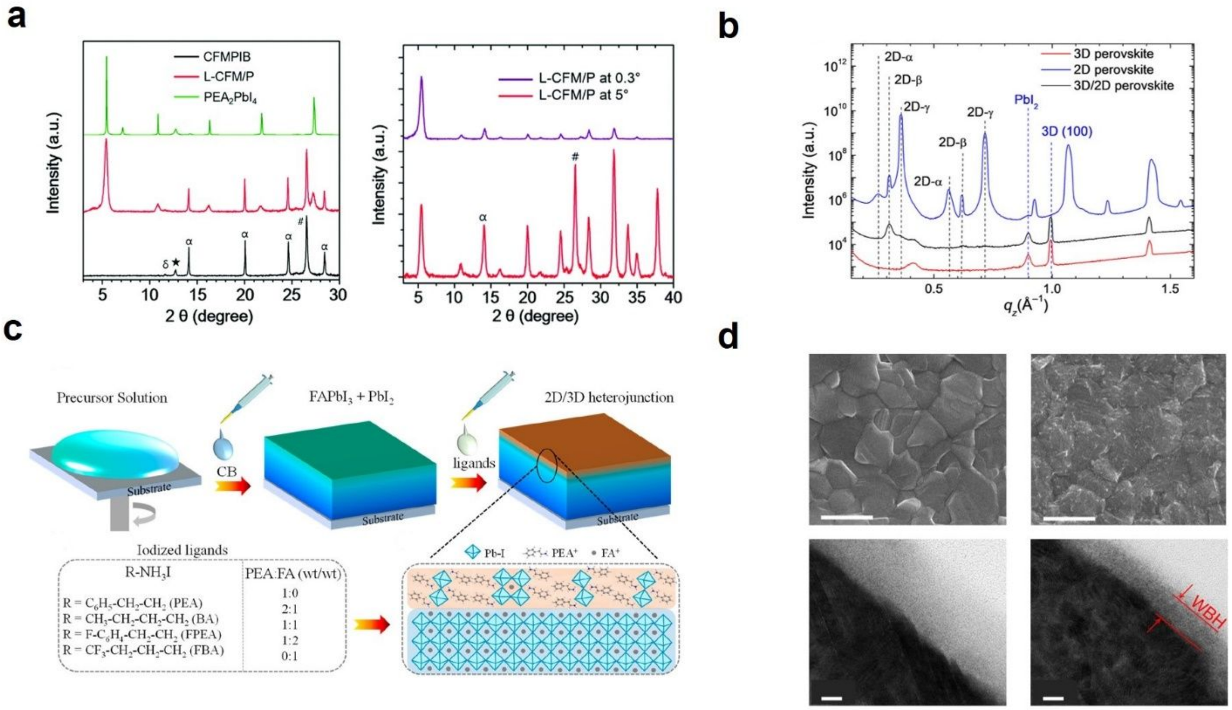

Figure 11. (**a**) XRD spectra (left) and XRD pattern (right) for the L-CFM/P film at X-ray incident angles of 0.3° (for surface) and 5° (for interior). CFMPIB represents pristine 3D perovskite and L-CFM/P represents pristine 3D perovskite with a 2D perovskite layer. Reproduced with permission from ref. 229. Copyright 2018, Royal Society of Chemistry. (**b**) XRR data of pure 2D, 3D, and 2D/3D perovskite films. Reproduced with permission form ref. 233. Copyright 2019, American Association for the Advancement of Science (AAAS). (**c**) Schematic illustration of fabricating the 2D/3D heterostructure and the schematic model of the 2D/3D hierarchical structure. Reproduced with permission from ref. 25. Copyright 2019, American Chemical Society. (**d**) SEM images of a pristine 3D perovskite surface (left) and the surface of the wide-bandgap low-D perovskite layer on the pristine perovskite (right); cross-section HRTEM images of the pristine perovskite (left) and the wide-bandgap low-D perovskite layer on pristine perovskite (right) near the surface. Scale bars: 1 μm (SEM); 10 nm (HRTEM). Reproduced with permission from ref. 21. Copyright 2019, Nature Publishing Group.

Table 6. Representative 2D perovskites used for interface modification to improve the performance and stability of perovskite solar cells.

Type	Perovskite	Device Structure	PCE (%)	Stability	Year[Ref]
BAI	$(Cs_{0.05}(MA_{0.17}FA_{0.83})_{0.95}Pb(I_{0.83}Br_{0.17})_3)$	Device A	15.74	86% of PCE after 100 h, >50% RH, dark [a]	2018[226]
PEAI	$Cs_{0.1}FA_{0.74}MA_{0.13}PbI_{2.48}Br_{0.39}$	Device A	20.1	90% of PCE after 800 h, 50°C, MPPT, continuous light soaking [b]	2018[229]

PEAI	$Cs_{0.05}(MA_{0.17}FA_{0.83})_{0.95}Pb(I_{0.83}Br_{0.17})_3$	Device A	18.51	90% of PCE after 1000 h, dark, 60±10% RH [a]	2018[230]
F-PEAI	$Cs_{0.1}(MA_{0.17}FA_{0.83})Pb(I_{0.83}Br_{0.17})_3$	Device A	20.54	99% of PCE after 36 d, dark, 10%–30% RH [a]	2019[231]
PEAI	$(FAPbI_3)_{0.85}(MAPbBr_3)_{0.15}$	Device A	24.66	90% of PCE, over 600 h, MPPT, continuous light soaking [a]	2019[232]
F5PEAI	$Cs_{0.04}FA_{0.92}MA_{0.04}PbI_3$	Device A	22.16	90% of PCE after 1000 h, 40% RH, MPPT, continuous light soaking [a]	2019[233]
HTAB	$(FAPbI_3)_{0.95}(MAPbBr_3)_{0.05}$	Device A (changing spiro-OMeTAD to P3HT)	23.3	>95% of PCE after 1370 h, MPPT, continuous light soaking [b]	2019[21]
CAI	$MAPbI_xCl_{3-x}$	Device B	13.86	54% of PCE after 220 h, dark, >50% RH [a]	2016[234]
5-AVA	$(FAPbI_3)_{0.88}(CsPbBr_3)_{0.12}$	Device A (changing spiro-OMeTAD to CuSCN)	16.75	98% of PCE after 63 days, dark, 10% RH [a]	2018[236]
BABr	$Cs_{0.17}FA_{0.83}Pb(I_{0.6}Br_{0.4})_3$	Device A (changing c-TiO_2/m-TiO_2 to SnO_2)	19.8	N/A	2019[237]
A34	$Cs_{0.1}FA_{0.74}MA_{0.13}PbI_{2.48}Br_{0.39}$	Device A	20.13	N/A	2018[239]
PEAI-FAI mixture	$FAPbI_3$	Device A	21.15	52% of PCE after 60 days, dark, 30%–40% RH [a]	2019[253]
C_6Br	$(FAPbI_3)_{0.92}(MAPbBr_3)_{0.08}$	Device A	23.4	85% of PCE after 500 h, MPPT, continuous light soaking [b]	2019[242]
BAI	$CsPbI_2Br$	Device A (without m-TiO_2)	14.5	80% of PCE after 25 days in 10% RH and then another 25 days in 25% RH, dark [a]	2019[251]

Note:

[a] Non-encapsulated devices.

[b] Encapsulated devices or non-encapsulated devices in Ar or N_2 atmosphere.

Device A: FTO/c-TiO_2/m-TiO_2/PVK/spiro-OMeTAD/Au.

Device B: ITO/PEDOT:PSS/PVK/PCBM/rhodamine 101/LiF/Ag

4.4. Lead-Free 2D Perovskites

One research topic in the perovskite field is evaluating Pb alternatives so as to reduce the potential toxic impact from Pb.[254-256] For this reason, some researchers have explored quasi-2D perovskites by replacing Pb^{2+} with Sn^{2+},[257] such as $PEA_2FA_{n-1}Sn_nI_{3n+1}$,[258] where a 2D/3D (PEA,FA)SnI_3 bulk heterojunction structure was shown to exhibit improved device performance and stability. In another study, different bulky cations benzylammonium (BzA^+) and histammonium (HA^{2+}) were applied to form $BzA_2Pb_{1-x}Sn_xI_4$ and $HAPb_{1-x}Sn_xI_4$ perovskites.[99] The inorganic frameworks of Sn-based 2D perovskite ($n = 1$) is less distorted than that of 2D Pb-based perovskites,[255] leading to slightly smaller bandgaps (**Figure 12a**).

Kanatzidis *et al.* first used triethylphosphine (TEP) as an intermediate coordinating ligand to improve film quality of $PEA_2MA_3Sn_4I_{13}$ ($n = 4$, **Figure 12b**), resulting in a PCE of 2.53% (**Table 7**).[259] By increasing the 2D layer thickness to nine, $(PEA)_2(FA)_8Sn_9I_{28}$ showed much better stability compared to 3D $FASnI_3$-based devices.[260] Importantly, $(PEA)_2(FA)_8Sn_9I_{28}$ also showed much improved V_{oc} (0.59 V) compared to 3D $FASnI_3$, leading to an efficiency of 5.94%. The improved V_{oc} in the quasi-2D perovskites was attributed to a lower defect density associated with suppressed Sn^{2+} oxidation. By further improving the *n* number, $PEA_2FA_{49}Sn_{50}I_{151}$-based solar cells showed 9% efficiency for Sn-based PSCs, which is much better than the 6% efficiency for the control device based on 3D $FASnI_3$.[261] Huang *et al.* first used the mixed bulky organic cations PEA and BA in 2D Sn-based perovskites to control the crystallization process.[262] Combining BA^+ and PEA^+ to $(BA_{0.5}PEA_{0.5})_2FA_3Sn_4I_{13}$ ($n = 4$) 2D perovskites effectively suppressed the intermediate phase that hinders the uniform nucleation of the perovskite crystals, resulting in improved perovskite morphology and orientation (**Figure 12c**) along with a higher PCE of 8.82%.

Sn(II)-based DJ-type 2D perovskite, $(4AMP)(FA)_{n-1}Sn_nI_{3n+1}$ was recently reported by Zhou *et al.* in solar cells with a performance of over 4%; the unencapsulated device showed 9% degradation after 100 h under 1-sun illumination in N_2 atmosphere at 45°C (**Figure 12d**).[263] They further investigated a series of DJ-type 2D Pb-free perovskites of (diammonium)$(FA)_{n-1}Sn_nX_{3n+1}$ ($n = 1$–4) with the target to overcome the charge-transport limitation.[264] The diammonium candidates include anthra[2,3-*b*:7,8-*b′*]bis(5-thiopheneylmethanammonium) (ATMA), 2,10-hexacenediyldimethanammonium (HMA), 2,9-pentacenediyldimethanammonium (PMA), 2,8-tetracenediyldimethanammonium (TMA), or 2,6-anthracenediyldimethanammonium (AMA).

Through DFT calculation, three compounds—(TMA)$(FA)_3Sn_4I_{13}$, (PMA)$(FA)_3Sn_4I_{13}$, and (ATMA)$(FA)_3Sn_4I_{13}$—were identified to have a type-II band alignment (staggered bandgap) and fast charge transport.

Table 7. Representative Pb-free 2D perovskites absorbers used for Pb-free PSCs.

Perovskite	**Device Structure**	**PCE (%)**	**Stability**	**Year[Ref]**
Bn_2SnI_4 ($n = 1$)	FTO/c-TiO_2/m-TiO_2/ PVK/Au	2.35	N/A	2019[257]
$PEA_2MA_3Sn_4I_{13}$ ($n = 4$)	FTO/c-TiO_2/ PVK/PTAA/Au	2.53	90% of PCE after 1 month, dark [a]	2017[259]
$(PEA)_2(FA)_8Sn_9I_{28}$ ($n = 9$)	ITO/NiO_x/PVK/PCBM/Al	5.94	96% of PCE after 100 h, dark [a]	2017[260]
$PEA_2FA_{49}Sn_{50}I_{151}$ ($n = 50$)	ITO/PEDOT:PSS/PVK/ PCBM/BCP/Al	9.0	59% of PCE after 76 h, dark, 20% RH [b]	2018[261]
$(BA_{0.5}PEA_{0.5})_2FA_3Sn_4I_{13}$ ($n = 4$)	ITO/PEDOT:PSS/PVK/ C60/LiF/Al	8.82	59% of PCE after 8 days, dark [a]	2019[262]
(4AMP)$(FA)_3Sn_4I_{13}$ ($n = 4$)	FTO/TiO_2/ZrO_2/PVK/C	4.22	91% of PCE after 100 h, continuous light soaking 45°C [a]	2019[263]

Note:

[a] Encapsulated devices or non-encapsulated devices in Ar or N_2 atmosphere.

[b] Non-encapsulated devices in air.

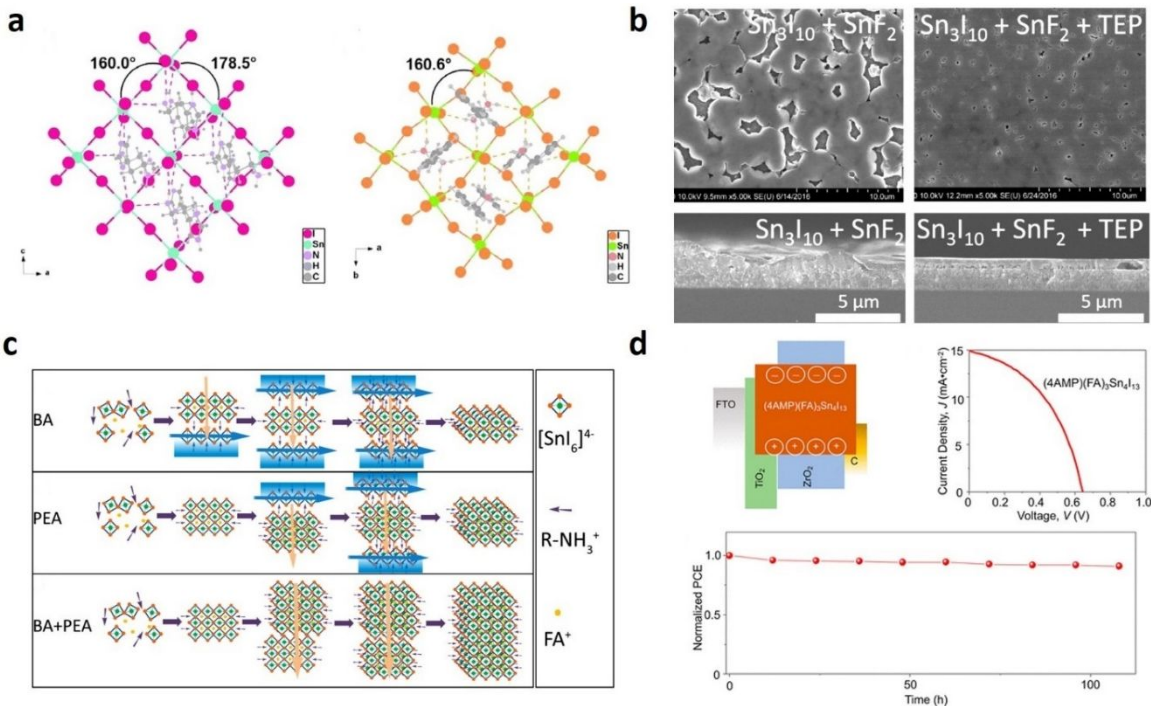

Figure 12. (**a**) Structure of (HA)SnI_4 (left) and $(BZA)_2SnI_4$ (right). Reproduced with permission from ref. 99. Copyright 2017, American Chemical Society. (**b**) SEM images (top: surface view; bottom: cross-section view) of $PEA_2MA_3Sn_4I_{13}$ films without (left) and with (right) TEP additive. Reproduced with permission from ref. 259. Copyright 2017, American Chemical Society. (**c**) An illustration of the crystal-growth process in Sn-based 2D perovskites of BA and/or PEA. Reproduced with permission from ref. 262. Copyright 2019, American Chemical Society. (**d**) Energy-level diagram, *J-V* curves, and stability for hole transport layer (HTL)-free PSCs based on $(4AMP)(FA)_3Sn_4I_{13}$ ($n = 4$). Reproduced with permission from ref. 263. Copyright 2019, American Chemical Society.

5. Application Beyond Solar Cells

In addition to solar cell applications, the excitonic character and versatile structure in the hybrid 2D perovskites also opens the door to other optoelectronic applications. For instance, the excitonic effect in *low-n* 2D perovskites can significantly promote radiative recombination, which leads to higher PLQY in perovskite-based LED devices, making them excellent candidates for high-efficiency LEDs. The structural versatility (*i.e.* organic or inorganic component, dimensionality, crystalline phase, impurity doping), if engineered properly, can allow us to precisely tune their broadband emission, spin lifetime/population, magnetic ordering, along with associated optical, electrical, and magnetic properties. Below we summarize some of the pioneering work of using hybrid 2D perovskites for optoelectronic applications beyond solar cells, including LEDs, spintronics-devices, and photodetectors.

5.1. Light-Emitting Diodes

Two-dimensional metal halide perovskites have emerged as a promising candidate for high-performance light-emitting diodes (LEDs) in the past few years. The superior properties of 2D layered perovskites as electroluminescent materials, when compared to their 3D counterparts, can be summarized as follows.

1) 2D perovskites generally possess much larger exciton binding energies (hundreds of meV)[265, 266] due to dielectric and quantum confinement of the layered structure, which leads to an enhanced radiative recombination and thus higher PLQY.

2) The formation of cascaded energy structures within 2D perovskite films with *mixed n* (layer thickness) can promote rapid and efficient energy transfer from *lower-n* quantum wells to *higher-n* quantum wells (in sub-ns), leading to a reduced exciton quenching effect and enhanced radiative recombination.

3) The incorporation of hydrophobic organic ligands and the enhanced van der Waals interactions between the organic molecules result in a significantly enhanced ambient and thermal stability compared to 3D perovskites with no such hydrophobic molecules.

4) The rich chemical tunability of 2D perovskites, including both organic and inorganic subcomponents, enables unprecedented opportunities to tune their optical and electrical properties for a much broader range of applications such as broadband emission, circular-polarized emission, and detection.

Here, we summarize recent progress in LEDs based on 2D layered perovskites (single-layer vs. quasi-2D and RP vs. DJ), excluding 3D ABX_3-type perovskite thin films, 2D nanoplatelets/nanosheets, or quantum dots, which can be found elsewhere.[17, 267-272]

5.1.1 LEDs based on single-layer *n* = 1 2D perovskites

The usage of RP-type 2D perovskites as electroluminescent layers within an LED can be traced back to Nurmikko's[273] and Saito's[274] work in the 1990s, where the optical properties of single-layered ($n = 1$) PEA_2PbI_4 were investigated and LED devices fabricated. However, they found that a very high (~24 V) turn-on voltage was needed, and the electroluminescence efficiency and quantum yield was minimal at room temperature.[274] It still remains difficult to fabricate high-efficiency LEDs based on n = 1 2D perovskites, even though they intrinsically possess a higher exciton binding energy. The poor performance is ascribed to poor out-of-plane (layer-to-layer) charge transport at low voltages due to the insulating organic ligands and fast nonradiative exciton quenching at room temperature due to powerful exciton-phonon coupling within the layers. The poor charge transport within the n = 1 2D system results in a high voltage to turn on the electroluminescence. The electron-phonon interactions, both for acoustic and optical phonons, is found to be orders of magnitude higher than found in GaAs quantum wells, leading to low PLQY at room temperature.[275] For these reasons, there has been rather slow progress in LEDs based on n = 1 2D perovskite active layers over the last few decades. In 2016, Jin *et al.* used 2D layered PEA_2PbBr_4 nanoplates and fabricated color-pure violet LEDs emitting at 410 nm with a low external quantum efficiency (EQE) of 0.04% at 6 V at room temperature.[276] In 2018, Sargent and co-workers systematically investigated the relationship between PLQY and electron-phonon interaction by preparing high-quality n = 1 2D perovskite single crystals.[277] Through tuning the molecular structures of organic ammonium cations, they were able to control crystal rigidity and electron-phonon interactions, which leads to modulation of their PLQY. Their results showed that the greater the structure rigidity is, the brightest the emitter is. Their optimized structure with PhC2 crystals, namely PEA_2PbBr_4, displayed a PLQY of 79%, although LED devices based on this formula were not fabricated. To address the challenges associated with strong electron-phonon interaction in n = 1 2D perovskites, the field has shifted focus to using quasi-2D ($1 < n < \infty$) layered perovskites as electroluminescent layers.

5.1.2 LEDs based on quasi-2D layered perovskites

In 2016, several breakthroughs were reported showing that electroluminescent layers based on quasi-2D perovskites can display better performance than even their 3D counterparts (**Table 8**). In the $PEA_2(MA)_{n-1}Pb_nBr_{3n+1}$ (n = 1–4) system, Lee *et al.* demonstrated that the quasi-2D perovskites displayed a much higher current efficiency and luminance than 3D $MAPbBr_3$ and 2D n = 1 PEA_2PbBr_4.[278] By tuning the ratio of $MAPbBr_3$ and PEA_2PbBr_4, they were able to achieve a high current efficiency of 4.90 cd/A and a luminance of 2935 cd/m^2. The iodide-based analogue

$PEA_2(MA)_{n-1}Pb_nI_{3n+1}$ ($n = 5$) has been demonstrated by Sargent and co-workers to outperform 3D $MAPbI_3$ ($n = \infty$) for near-infrared emission, with an EQE of 8.8% and a radiance of 80 W sr^{-1} m^{-2}.[61] They further ascribed the superior performance to a cascading energy transfer that funnels photoexcitations to the lowest-bandgap phase within mixed quasi-2D perovskite thin film (**Figure 13a**). Soon after that report, Huang and co-workers demonstrated quasi-2D perovskite LEDs based on $(NMA)_2(FAPbI_3)_{n-1}Pb_nI_{3n+1}$ with a recorded EQE of 11.7% and radiance of 82 W sr^{-1} m^{-2}.[279] Similarly, they also attributed the superior device performance to the funneling mechanism, which occurs within sub-ns timescales and outcompetes nonradiative exciton quenching and increases radiative recombination (**Figure 13b**,**c**). By embedding the quasi-2D perovskites into a high-bandgap polymer forming a bulk heterojunction, Di and co-workers reported LEDs with a record EQE of 20.1%.[280] The polymer component is stated to significantly suppress the bulk and interfacial non-radiative relaxation process. The same energy-funnel concept is also applied within the bromide system,[281] $PEA_2(MA)_{n-1}Pb_nBr_{3n+1}$, showing an EQE of 7.4% and luminescence of 8400 cd/m^2 for green LEDs. By mixing PEA with IPA (iso-propylammonium), Sargent and co-workers showed that the mixed cation can destabilize $n = 1$ phase, and lead to the formation of only quasi-2D perovskites with $n = 2$, 3, and 4 phases.[282] Their perovskite films showed a record PLQY of 88% at 477 nm. The corresponding LEDs device displayed stable sky-blue emission with a maximum luminance of 2480 cd m^{-2} achieved at 490 nm. You and co-workers reported other green LEDs based on $PEA_2(FAPbBr_3)_2PbBr_4$ ($n = 3$).[283] With optimized phase engineering and surface passivation, they achieved a current efficiency of 62.4 cd A^{-1} and EQE of 14. 36%. The mixture of different phases (different layer thicknesses or n numbers) does not seem to be detrimental to LED performance; however, careful phase engineering to favor directional energy funneling is extremely important, and an ongoing challenge, for LEDs based on quasi-2D perovskites.

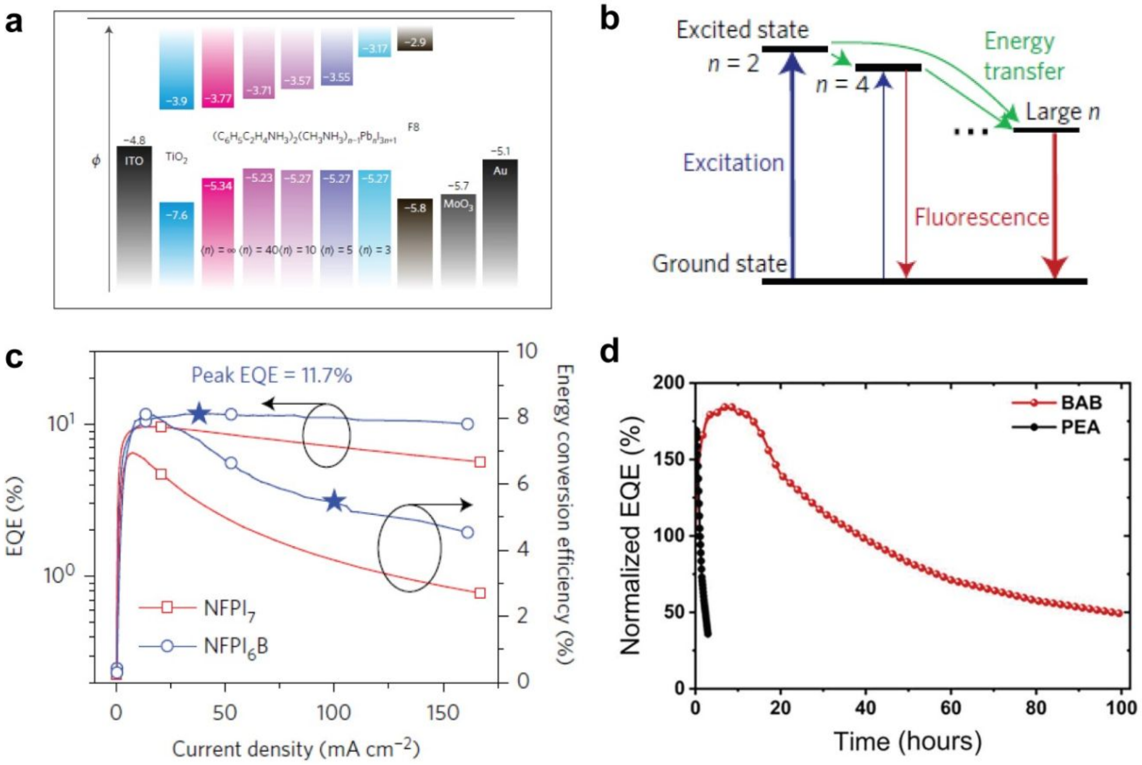

Figure 13. (a) Electronic band structure of ITO, TiO_2, F8, MoO_3, Au electrode, and quasi-2D perovskites with different layer thicknesses (*n* numbers). Reproduced with permission from ref. 61. Copyright 2016, Nature Publishing Group. **(b)** Schematic illustration of cascade energy transfer in quasi-2D perovskite thin films. Reproduced with permission from ref. 279. Copyright 2016, Nature Publishing Group. **(c)** EQE and energy conversion efficiency as a function of current density for the NFPI6B and NFPI quasi-2D perovskite LEDs. Reproduced with permission from ref. 279. Copyright 2016, Nature Publishing Group. **(d)** Operational lifetimes of DJ and RP structure perovskite-based LEDs. Reproduced with permission from ref. 284. Copyright 2019, American Association for the Advancement of Science.

Table 8. Summary of representative highly efficient 2D and quasi-2D perovskite LEDs

Perovskite Composition	Wavelength (nm)	EQE (%)	CE (cd/A)	Lmax (cd/m^2)	Radiance (W sr^{-1} m^{-2})	Year[Ref]
PEA_2PbBr_4	410	0.04	–	–	–	2016[276]
$PEA_2(MA)_{n-1}Pb_nBr_{3n+1}$	526	7.4	4.9	8,400	–	2017[281]
$PEA_2(MA)_{n-1}Pb_nI_{3n+1}$	~760	8.8	–	–	80	2016[61]
$(NMA)_2(FAPbI_3)_{n-1}Pb_nI_{3n+1}$	763	11.7	–	–	82	2016[279]
$(NMA)_2(FAPbI_3)_{n-1}Pb_nI_{3n+1}$/ poly-HEMA	795	20.1	–	–	–	2018[280]
$PEA_2(FAPbBr_3)_2PbBr_4$	532	14.36	62.43	9,120	–	2018[283]

(BAB)$FA_{n-1}Pb_nX_{3n+1}$	776	4.2	–	–	88.5	2019[284]

In addition to the superior LED performance when compared to 3D perovskites, quasi-2D perovskite also exhibit improved stability. Huang and co-workers demonstrated a T_{50} (the amount of time for the EQE to drop to half its initial value) of 2 h under a constant current density of 10 mA cm^{-2}, which is two orders of magnitude better than that based on 3D perovskites (T_{50} = 1 min).[279] Recently, using phase-pure RP-type 2D perovskites based on $BA_2(MA)_{n-1}Pb_nI_{3n+1}$, Kanatzidis, Mohite, and co-workers achieved efficient electroluminescence with a radiance of 35 W sr^{-1} m^{-2} at 744 nm and a significantly enhanced stability (T_{50} > 14 h) compared to quasi-2D or 3D perovskite systems.[285] Their results suggest that although mixed-phase quasi-2D perovskite can promote efficient energy funneling from *lower n* to *higher n*, growing phase-pure 2D perovskite is also an important route for improving device stability. Very recently, the stability of LED-based on quasi-2D perovskites has been dramatically improved by using the DJ rather than RP structure. Ning and co-workers demonstrated that LEDs based on the DJ quasi-2D perovskites ((BAB)$FA_{n-1}Pb_nX_{3n+1}$ (BAB: 1,4-bis(aminomethyl)benzene; X: Br, I)) exhibit a T_{50} of over 100 hours, which is nearly two orders of magnitude longer compared to LEDs based on RP quasi-2D perovskite systems (**Figure 13d**).[284] Their optimized LEDs exhibit an EQE of 5.2% with a maximum radiance of 88.5 W sr^{-1} m^{-2}. Therefore, it is clear that a balance of LED device efficiency and stability requires careful optimization of organic ligands, crystallographic structure, phase engineering, and crystalline orientation of quasi-2D perovskites.

5.1.3 Broadband emission in 2D perovskites

Another interesting optical property of 2D perovskites, in addition to their excitonic emission, is broadband emission enabled by the rich chemical tunability in 2D metal halide perovskites. If the broadband emission covers the visible spectrum, then the emitters can be used as single-source white-light emitters at a high quantum efficiency to produce great energy-efficiency compared to current mixed phosphor based technology. The development of metal halide perovskites as single-source white-light emitters is a young, yet-emerging field. In 2014, seminal work from Karunadasa and co-workers demonstrated bright broadband visible emission in 2D perovskite (EDBE)PbX_4 (**Figure 14a**)[132] and (N-MEDA)$PbBr_{4-x}Cl_x$,[128] (N-MEDA: N^1-

methylethane-1,2-diammonium; EDBE: 2,2-(ethylenedioxy) bis(ethylammonium); X: Cl, Br). Since those results, several white-light-emitting 2D perovskites have been developed as single-source white-light phosphors (**Table 9**). From the standpoint of crystal structures, strong white-light emission has been discovered in both corrugated (110) and (001) Pb-Br and Pb-Cl perovskite-based layered systems. The reported 2D (110) layered perovskites that exhibit broadband emission are (N-MEDA)$PbBr_{4-x}Cl_x$, (N-MEDA)$PbBr_4$, and α-(DMEN)$PbBr_4$[129] (α-DMEN: N^1,N^1-dimethylethane-1,2-diammonium). For instance, by tuning the halide composition in (110) (N-MEDA)$PbBr_{4-x}Cl_x$, Karunadasa[128] and co-workers were able to improve the emission's color-rendering index (CRI) from 82 to 85, yet the PLQY was only 0.5%–1.5%. The PLQY was subsequently improved with their second white-light-emitting (110) perovskite (EDBE)$PbBr_4$,[132] which displays a PLQY of 9% with a CRI of 84. In 2017, Kanatzidis and co-workers reported another white-light-emitting (110) perovskite, namely α-(DMEN)$PbBr_4$, which emits cold white light with a CRI of 73.[129] The first example of a (001) white-light-emitting perovskite is (EDBE)$PbCl_4$, which emits cold white light with a CRI of 81 and a PQLY of 2%. Subsequently, other (001) white-light-emitting perovskites have been reported including $(C_6H_{11}NH_3)_2PbBr_4$,[286] $(H_3NC_6H_4(CH_2)_2NH_3)PbBr_4$ or (AEA)$PbBr_4$,[122] (CyBMA)$PbBr_4$ (CyBMA: cis-1,3-bis(ammoniomethyl)cyclohexane),[287] and $(EA)_4Pb_3Br_xCl_{10-x}$ (EA: $CH_3CH_2NH_3^+$).[76] However, the demonstrated 2D perovskite compounds are still quite limited and the PLQYs observed to date remain low. An improved atomistic understanding is needed to elucidate the underlying mechanism and origin of the bright broadband emission of these materials and enable higher PLQY.

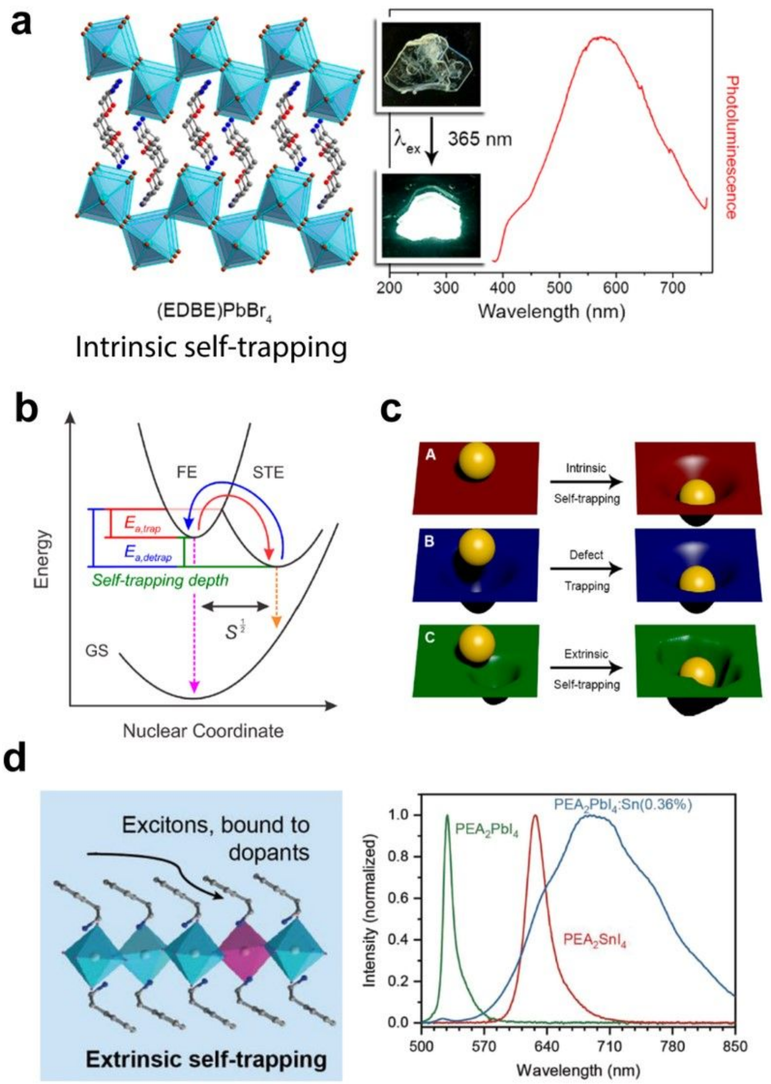

Figure 14. (a) Crystal structure of the (110) 2D (EDBE)$PbBr_4$ perovskite and its PL emission. Inset shows the crystal photographs. Reproduced with permission from ref. 132. Copyright 2014, American Chemical Society. **(b)** Schematic illustration of dopant-induced extrinsic self-trap exciton and PL spectra of PEA_2PbI_4, PEA_2SnI_4, and PEA_2PbI_4:Sn (0.36%). Reproduced with permission from ref. 122. Copyright 2017, Royal Society of Chemistry. **(c)** Schematic illustration of the three formation mechanisms of self-trap excitons: intrinsic, defect, and extrinsic. Reproduced with permission from ref. 288. Copyright 2018, American Chemical Society. **(d)** Nuclear coordinate diagram for exciton self-trapping and detrapping process in 2D perovskites. Reproduced with permission from ref. 289. Copyright 2019, Wiley-VCH.

Although some research groups attributed the broadband emission to crystal defects that serve as the broadband color centers,[290, 291] the mechanism of the broadband emission in these 2D perovskite systems is generally believed to be exciton self-trapping (**Figure 14b**), where photoexcitation induces an excited-state lattice distortion mediated through the strong electron-lattice coupling.[122, 288] Ultrafast pump-probe spectroscopy results suggest that the photogenerated excitons self-trap in sub-ps (~400 fs), which is followed by luminescence, and the lattice distortion leads to homogeneous emission broadening.[64] The presence of multiple self-trapped exciton states can further broaden the emission inhomogeneously. Additionally, reducing the temperature generally leads to an enhanced broadband emission compared to free-exciton emission. This temperature-dependent emission property can be understood by the thermodynamics of the self-trapping and de-trapping processes (**Figure 14b**),[122] where the higher temperature provides enough activation energy to de-trap back to the free-exciton state from self-trapped exciton ($k_B T > E_{a,\mathrm{detrap}}$), thereby reducing the broadband emission and increasing the free-exciton emission. Therefore, although only a few 2D perovskites have been reported as white-light emitters, broadband emission in perovskites, in theory, can be generalized if the thermodynamic activation energies of self-trapping and de-trapping process are optimized at specific temperatures.

Table 9. Summary of representative broadband-emitting 2D perovskites

Perovskite Composition	**PLQY (%)**	**CRI**	**CIE (*x*, *y*)**	**Year[Ref]**
(EDBE)$PbBr_4$	9	84	(0.39, 0.42)	2014[132]
(EDBE)$PbCl_4$	2	81	(0.33, 0.39)	2014[132]
(*N*-MEDA)$PbBr_4$	0.5	82	(0.36, 0.41)	2014[128]
(*N*-MEDA)$PbBr_{3.5}Cl_{0.5}$	–	85	(0.31, 0.36)	2014[128]
α-(DMEN)$PbBr_4$	–	73	(0.28, 0.36)	2017[129]
(AEA)$PbBr_4$	–	87	(0.29, 0.34)	2017[122]
(CyBMA)$PbBr_4$	1.5	–	(0.23, 0.29)	2017[287]
$(EA)_4Pb_3Br_{0.5}Cl_{9.5}$	–	83	(0.30, 0.35)	2017[76]
PEA_2PbI_4:Sn (0.36%)	6.0	–	–	2019[289]
PEA_2PbI_4:Sn (1%)	23	–	–	2020[292]

Thus far, most reported broadband-emitting 2D perovskites have been discovered with the special design of organic amines, where the broadband emission is ascribed to the intrinsic self-trapped excitons (**Figure 14c**). More recently, Chen and co-workers demonstrated that impurity Sn dopants can trigger extrinsic self-trapping of excitons in PEA_2PbI_4, giving broadband red-to-near-infrared emission at room temperature (**Figure 14d**).[289] A similar observation has recently been reported by Mitzi and co-workers, which suggests that metal impurities, even at trace levels, should be considered more carefully when preparing these crystals and films, as they could have a fundamental impact on their optical and electronic properties.[292] This introduces a new strategy— namely, dopant-induced extrinsic exciton self-trapping approach (**Figure 14c**)—to the development of broadband-emitting perovskites. However, this field is still in its infancy, and more materials need to be investigated. A generalized theory and a mechanism of broadband emission, across different hybrid material systems, are very much needed for discovering next-generation white-light phosphors. For instance, the community is still searching for a simple and general correlation between broadband emission and structure dimensionality, crystal distortions (e.g., in-plane and out-of-plane octahedral distortion), and impurity dopants. Karunadasa and co-workers have shown an interesting linear correlation between the most considerable measured out-of-plane distortion D_{out} ($180° - \theta_{\text{out}}$) and the ratio of broadband emission vs. excitonic emission at a given temperature, after rigorously testing over 50 other structural parameters.[122] DFT calculations by Yan and co-workers revealed that a low electronic dimensionality, rather than the structural dimensionality, is a prerequisite for forming broadband emission, and only the self-trapped excitons with Jahn-Teller-like octahedral distortions can lead to the observed broadband emission.[293]

5.2. Spintronic Application

Because of strong spin-orbital coupling (SOC) associated with heavy elements (e.g., Pb and I), hybrid metal halide perovskites are considered attractive candidates for spintronics and spin optoelectronics. In conjunction with inversion asymmetry, SOC in perovskites further leads to an effective magnetic field that lifts the degeneracy of the carrier spin states within conduction and/or valence bands, which is often referred to as the Rashba effect.[294] The spin-degenerate parabolic band is now split into two spin-polarized bands, and the new parabolic bands can be described by $E\pm(k) = (\hbar^2k^2/2m^*) \pm \alpha_R|k|$, where α_R is the Rashba splitting parameter (**Figure 15a**). Thus far, spin-optoelectronic devices based on 3D perovskites have been investigated both theoretically and experimentally,[40, 295-297] although the relative role of bulk and surface Rashba contributions is still under debate.[298, 299] This is because crystal structures of perovskite in bulk (*i.e.,* tetragonal or orthorhombic) present inversion symmetry, where Rashba effect should be forbidden. As such, it is proposed that the Rashba effect is a surface effect due to structural distortion at the surface; but it is likely that surface reconstruction penetrates several hundred nanometers toward the bulk. In many cases, large Rashba splitting has been experimentally observed (by angle-resolved photoelectron spectroscopy (ARPES),[300] for instance), making them promising candidates for spintronic applications. Reduced dimensionality, namely from 3D perovskite to 2D perovskite, can further reduce the symmetry, resulting in an enhanced Rashba effect. This is similar to many aspects of 2D heterostructures in traditional semiconductors where the Rashba effect are often observed.[301] Additionally, the rich chemical tunability of 2D perovskites—including controllable distortions of the inorganic framework, inorganic layer thickness, and organic components—makes 2D perovskites an exciting platform to investigate their structure-Rashba-effect relationships; it also brings new opportunities for spintronic applications. Here we summarized recent advances in spintronic devices based on 2D hybrid perovskites, neglecting those based on 3D perovskites which can be found in other literature reports.[295, 297, 302-305]

5.2.1. Rashba splitting in 2D perovskite

Based on the electroabsorption and photoinduced absorption spectra, Vardeny and co-workers reported a giant Rashba splitting in 2D $n = 1$ PEA_2PbI_4, with energy splitting of (40 ± 5) meV and Rashba parameter of (1.6 ± 0.1) eV (**Figure 15b**).[306] Further DFT calculations showed that the Rashba splitting originates from the broken inversion symmetry due to Pb atom displacement from the octahedral center. This resulted in the Rashba band splitting in the plane perpendicular to the 2D barriers. However, a subsequent report from Mohammed and co-workers using both DFT calculations and time-resolved PL showed that intrinsic, large Rashba splitting only occurs in the 2D perovskite crystals with even number of inorganic layers, namely $PEA_2MAPb_2I_7$ ($n = 2$), but not in the $n = 1$ or $n = 3$ crystals.[307] Their results highlight the importance of the layer thickness in 2D perovskites for Rashba splitting. The presence of Rashba splitting in 2D $BA_2MAPb_2I_7$ ($n = 2$) was also recently confirmed by Hall and co-workers, in which time-resolved circular dichroism techniques were used to probe the carrier spin-relaxation dynamics.[308] Their simulations of the measured spin dynamics show a Rashba spin splitting of 10 meV at an electron energy of 50 meV above the bandgap. Also, a 2018 report measured the spin-relaxation dynamics to “indirectly” probe the Rashba effects in 2D perovskite systems.[309] In this study, Beard and co-workers used a circularly polarized pump-probe method (**Figure 15c**) to study the spin-coherence dynamics in 2D perovskite single crystals with different layer thicknesses ($n = 1– 4, \infty$). It was found that the spin-coherence lifetime increases with increasing layer thickness from $n = 1$ to $n = 4$, followed by a decrease from $n = 4$ to ∞ (**Figure 15d**). These results were attributed to two counteracting contributions: 1) Rashba splitting increases the spin-coherence lifetime from the $n = \infty$ to the layered systems; and 2) phonon scattering, which increases for smaller n values, decreases the spin-coherence lifetime due to spin-lattice relaxation. They proposed that the Elliot−Yafet (EY) mechanism is the main cause for spin depolarization.

Using 2D perovskites to manipulate spin polarization has also been demonstrated recently. In the $(F\text{-}PEA)_2PbI_4$ thin film, Sum and co-workers demonstrated a room-temperature spin-selective optical Stark effect (OSE).[310] They found that the exciton spin states can be selectively tuned by ~6.3 meV using circularly polarized optical pulses without any external photonic cavity. Their result opens up new avenues for using these 2D perovskites for opto-spin logic applications. In the quasi-2D perovskite systems, the same group recently demonstrated that the ultrafast energy funneling from *low-n* to *high-n* perovskites, as shown in LEDs, also preserves their spin information, thus achieving spin funneling in the quasi-2D perovskite films with thickness up to 600 nm.[311] Using 2D perovskites for (optical) spin manipulation is an intriguing and exciting research direction; however, the spin lifetime of these systems are generally very short at high temperature. Future research should focus on 1) understanding the structure-Rashba-effect and structure-spin-lifetime correlation, and 2) demonstrating other spintronic devices, such as spin light-emitting diodes and spin valves.

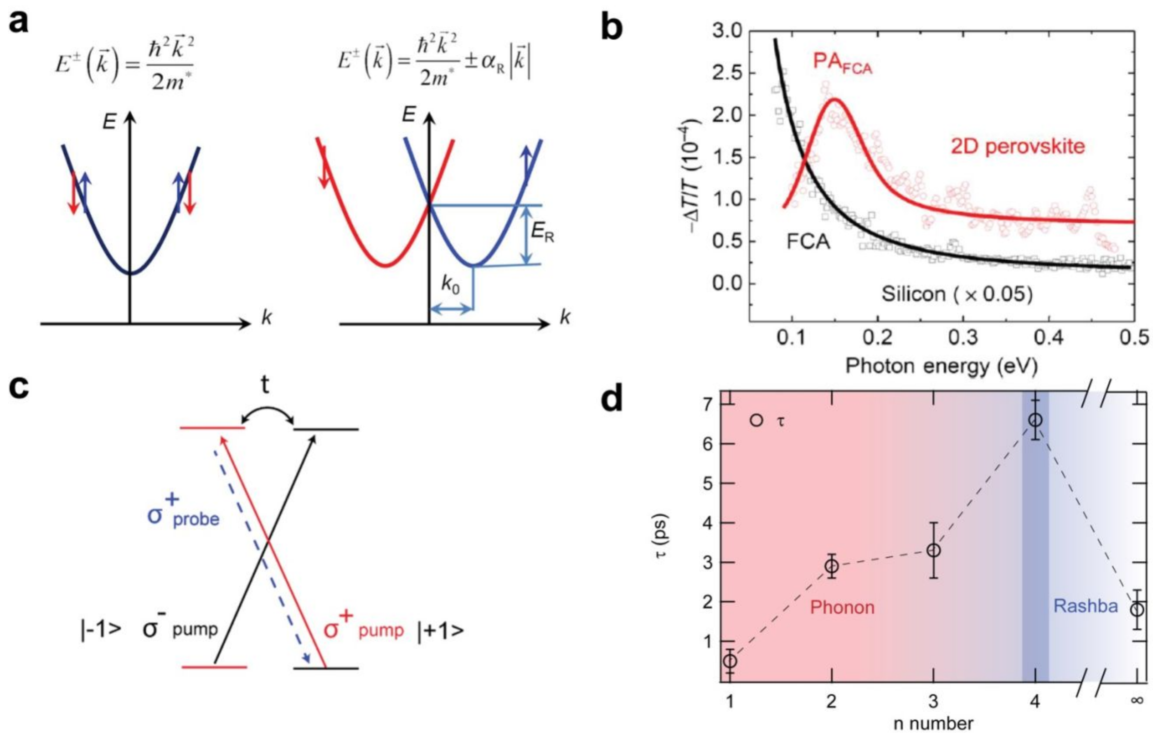

Figure 15. (a) Schematic illustration of Rashba splitting that generates two parabolic branches with opposite spin orientations. Reproduced with permission from ref. 306. Copyright 2017, American Association for the Advancement of Science. **(b)** Photomodulation spectrum of PEA_2PbI_4 film (excited at 2.8 eV) compared to that of a silicon wafer. Reproduced with permission from ref. 306. Copyright 2017, American Association for the Advancement of Science. **(c)** Illustration of spin dynamics measurements. **(d)** Spin coherent lifetime in excited states for $n = 1 - 4$ and 3D $MAPbI_3$ single crystals. c and d are reproduced with permission from ref. 309. Copyright 2018, American Chemical Society.

5.2.2. Chiral 2D layered perovskite systems

The chemical tunability of 2D perovskites also offers a unique opportunity to directly incorporate chiral organic molecules in between the inorganic layers, introducing chirality into the hybrid framework. Understanding how chirality can affect the Rashba effect, and how their synergetic effects can provide spin-control within this hybrid layered system, may bring new opportunities for spintronic applications. In 2018, Sargent and co-workers reported 3% spin-polarized photoluminescence at zero magnetic fields at 2 K in 2D Pb-Br perovskite multilayers that incorporated chiral organic molecules, suggesting that the spin degree of freedom of hybrid perovskites can be controlled by the chirality of the incorporated organic cations.[312] This is subsequently confirmed by Li and co-workers, who reported an average degree of circularly polarized photoluminescence (CPL) of 9.6% and 10.1% at 77 K for $(R\text{-MBA})_2PbI_4$ and (*S*-

MBA)$_2$PbI$_4$ (MBA: $C_6H_5CH(CH_3)NH_3$), respectively.[313] However, it should be noted that the demonstrated spin-polarized photoluminescence is likely intrinsically limited because the PL emission of $n = 1$ 2D chiral perovskite is rather weak. As such, more direct spin manipulation and associated demonstration in a spintronic device based on chiral perovskites should be both intriguing and insightful.

In a recent study, Lu *et al*. demonstrated that a polarized spin-transport through 2D chiral hybrid perovskites can be effectively manipulated depending on the handedness of the organic molecules, which occurs via the chiral-induced spin selectivity (CISS) mechanism (**Figure 16**).[314] Magnetic conductive probe AFM studies showed the highest spin-polarization transport of up to 86%, which is much larger than previously reported in chiral self-assembled monolayer systems (typically in the range of 30% to 50%[315, 316, 317]), as carriers transfer through multiple chiral layers undergoing a spin-polarized tunneling process. Magnetoresistance measurements in spintronics devices further confirm the spin-filtering effect enabled by the chiral organic layers, forming half spin-valve devices based on a single ferromagnetic electrode. The successful demonstration of the CISS effect in these 2D chiral perovskite films opens the door for future spintronic applications based on chiral hybrid materials.

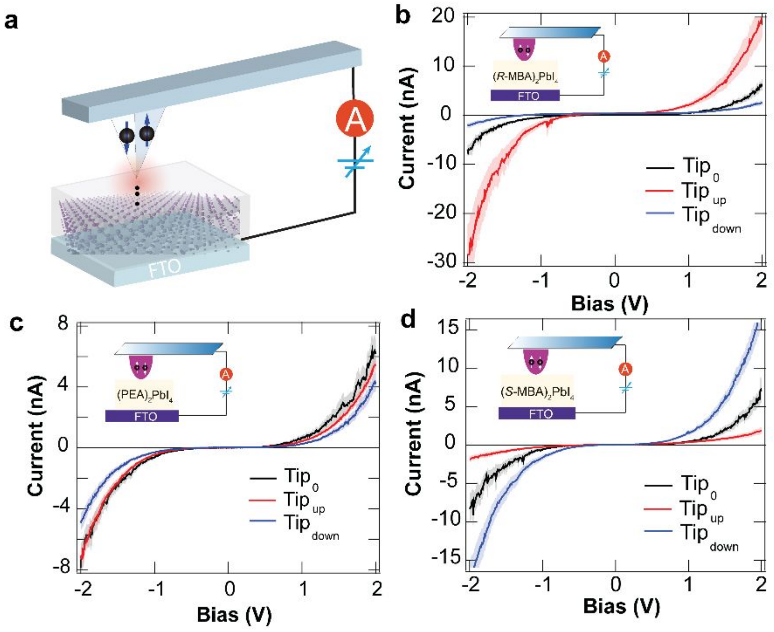

Figure 16. Schematic illustration of magnetic conductive probe AFM measurements **(a)** and chirality dependence in out-of-plane charge transport **(b–d)**. Reproduced with permission from ref. 314. Copyright 2019, American Association for the Advancement of Science.

5.3. Photodetector

Compared to 3D perovskites, which have drawn extensive attention for next-generation photodetectors,[318-321] the development of 2D perovskites for photodetectors is still in its infancy. Due to the poorly controlled crystalline orientation, phases, and anisotropic transport properties in microcrystalline films, 2D perovskite-based photodetectors usually require the use of single crystals; however, the growth of large-area, high-quality, shape-controlled 2D perovskite single crystals remains a significant challenge. As such, advances in 2D perovskite-based photodetectors is strongly tied to the growth of 2D perovskite single crystals.[322] Thus far, surface-tension-driven crystal growth has been shown to be the most effective approach to grow photodetector-quality 2D perovskite single crystals. In 2018, Priya and co-workers reported the growth of quasi-2D perovskite single-crystal membranes based on the surface-tension effect, where the growth rate of the precursor molecules at the water/air interface is much higher than those in bulk solution.[248] Their photodetector based on the BA_2PbI_4 ($n = 1$) shows a shallow dark current (10^{-13} A), higher on/off ratio (~10^4), and faster response time compared to those with higher n numbers. More recently, Liu and co-workers coupled the inverse temperature crystallization method with surface-tension control to achieve preferential crystallization of 2D perovskite single crystals at the solution/air interfaces.[323] Using this method, they were able to obtain high-quality, 36-mm-sized 2D PEA_2PbI_4 single crystals with a high aspect ratio. Photodetector devices based on different crystal facets, namely (001) and (010), show very different properties. The photodetectors based on the (010) planes show much less photo-response than those based on the (001) planes. Based on the (001) plane, the photodetectors display responsivity as high as 139.6 A W^{-1}, EQE of 37,719.6%, detectivity of 1.89×10^{15} Jones, and response speed as fast as τ_{rise}= 21 μs and τ_{decay} = 37 μs. Their photodetector performance based on 2D PEA_2PbI_4 single crystals is so far among the highest reported for all perovskite planar photodetectors.

6. Conclusion and Outlook

Since the first application of 2D perovskite absorbers in solar cells in 2014, the best PCE of 2D PSCs has improved to ~19% to date. This points out the promise of using or incorporating 2D perovskites for solar cells. In addition, 2D perovskites also display tremendous potential in LED, broadband emission, spintronic, and photodetector applications, and they serve as a prototype system to understand many fundamental structure-property relationships including spin-orbital coupling, Rashba effect, exciton-phonon coupling, and light-matter interactions. To further advance or explore the unique characteristics of 2D perovskites for all these applications, more efforts are required to focus on materials design, growth controls, and the fundamental physical and chemical properties of 2D organic-inorganic hybrid halide perovskites. Below we discuss key scientific challenges as well as our perspective on future research directions for 2D perovskites.

Phase purity of 2D perovskite thin films. The as-prepared 2D films almost always contain different *n* values, which presents a challenge to enabling different applications, but also complicates the scientific understanding of various physical and chemical properties of 2D perovskite structures, which, in turn, presents another challenge for tailoring materials design. Thus, it is necessary to develop synthetic tools and controls to obtain pure-phase 2D perovskite structures. Similarly, continued efforts on developing strategies to manipulate the growth orientation of 2D perovskite to either use or avoid the limitation of the anisotropic properties of 2D structures is crucial for the future development of this field.

Anisotropic charge transport in 2D perovskites. The vastly different charge-transport properties along the out-of-plane and in-plane directions for 2D perovskites will remain an active area of research for various optoelectronic applications. In addition, mixed bulky cations for 2D perovskite also shows promising results that should be pursued.[324, 325] Accurate description of the crystal structure of 2D perovskites is essential for revealing the role of bulky cations in perovskite formation and charge transport. In addition, a molecular library should be established by investigating the effect of different molecular lengths, conjugated groups, functional units, and the substituent groups on the charge-transfer capacity and other properties.

Quantum efficiency and stability. PLQY is a key parameter for characterizing the emission properties of 2D perovskites. At present, the PLQY for 2D structures remains low at room temperature because of the fast nonradiative exciton quenching due to the strong exciton-lattice coupling. Strategies in both molecular design and device engineering need to be explored to inhibit the nonradiative recombination in these systems. Meanwhile, a balance between quantum efficiency and stability need to be considered.

Fundamental structure-property relationships. Given all the observed interesting optical, electronic, and spin properties in 2D perovskites, little is known about the structural origin of these properties at the atomic level. In particular, general correlations between the crystallographic structural characters (e.g., dimensionality, distortions, impurity dopants) and broadband emission, Rashba effect, spin coherent lifetime, and spin polarization still need to be rigorously tested and established. The challenge here stems not only from the difficulties associated with the synthetic output, but also on developing direct, unambiguous characterization methods and theory to probe the optical, electronic, and spin properties. Understanding these key structure-property relationships can further provide synthetic guidance for the next-generation hybrid materials for targeted optoelectronic applications. This is a new, exciting area where synthetic, spectroscopic, and computational tools will be heavily involved, and it provides a tremendous playground and opportunities for chemists, physicists, and engineers to unveil the mystery of hybrid materials.

Finally, it is worth emphasizing that for solar cell applications even if 2D perovskites may not be used as the primary light absorber, these low-dimensional materials can still play important roles to improve the conventional 3D perovskite based photovoltaic devices. More research efforts will likely focus on 2D/3D mixed perovskites, where 2D perovskite can serve as a passivating agent or capping layer for improving the stability and efficiency of devices. At present, as many of these behaviors in these 2D systems have not yet been clearly defined, developing tools to identify/control/study the materials and their properties represents a pressing need for the field. More studies should focus on developing the synthetic control to form a transparent 2D capping layer with controlled energy levels and/or the layer thickness (i.e., n value) of the 2D structures. Design of new bulky organic cations that could form stable 2D structures with enhanced plane-to-plane charge transport along with new ways to control the 2D structure/composition will further advance the performance and stability of 2D/3D PSCs. [106, 175]

Acknowledgements

The work was supported by the U.S. Department of Energy under Contract No. DE-AC36-08GO28308 with Alliance for Sustainable Energy, Limited Liability Company (LLC), the

Manager and Operator of the National Renewable Energy Laboratory. The authors thank the support on fundamental design and characterization of 2D perovskite materials from the Center for Hybrid Organic Inorganic Semiconductors for Energy (CHOISE), an Energy Frontier Research Center funded by the Office of Basic Energy Sciences, Office of Science within the U.S. Department of Energy. The authors also appreciate the support of PV applications of 2D perovskites from the De-risking Halide Perovskite Solar Cells program, funded by the U.S. Department of Energy, Office of Energy Efficiency and Renewable Energy, Solar Energy Technologies Office. The views expressed in the article do not necessarily represent the views of the DOE or the U.S. Government. The U.S. Government retains and the publisher, by accepting the article for publication, acknowledges that the U.S. Government retains a nonexclusive, paid-up, irrevocable, worldwide license to publish or reproduce the published form of this work or allow others to do so, for U.S. Government purposes.

References

1. M. Grätzel, *Accounts of Chemical Research*, 2017, **50**, 487-491.
2. J.-P. Correa-Baena, M. Saliba, T. Buonassisi, M. Grätzel, A. Abate, W. Tress and A. Hagfeldt, *Science*, 2017, **358**, 739-744.
3. *Best Research-Cell Efficiency Chart, National Renewable Energy Laboratory,* *https://www.nrel.gov/pv/cell-efficiency.html* *(Augest,2019)*
4. Y. Rong, Y. Hu, A. Mei, H. Tan, M. I. Saidaminov, S. I. Seok, M. D. McGehee, E. H. Sargent and H. Han, *Science*, 2018, **361**, eaat8235.
5. D. Weber, *Z. Naturforsch. B.* , 1978, **33**, 1443.
6. D. Weber, *Z. Naturforsch. B.* , 1979, **34**, 939.
7. D. B. Mitzi, C. A. Feild, W. T. A. Harrison and A. M. Guloy, *Nature*, 1994, **369**, 467-469.
8. D. B. Mitzi, S. Wang, C. A. Feild, C. A. Chess and A. M. Guloy, *Science*, 1995, **267**, 1473-1476.
9. A. Kojima, K. Teshima, Y. Shirai and T. Miyasaka, *Journal of the American Chemical Society*, 2009, **131**, 6050-6051.
10. H.-S. Kim, C.-R. Lee, J.-H. Im, K.-B. Lee, T. Moehl, A. Marchioro, S.-J. Moon, R. Humphry-Baker, J.-H. Yum, J. E. Moser, M. Grätzel and N.-G. Park, *Scientific Reports*, 2012, **2**, 591.
11. M. M. Lee, J. Teuscher, T. Miyasaka, T. N. Murakami and H. J. Snaith, *Science*, 2012, **338**, 643-647.
12. D. Bi, C. Yi, J. Luo, J.-D. Décoppet, F. Zhang, Shaik M. Zakeeruddin, X. Li, A. Hagfeldt and M. Grätzel, *Nature Energy*, 2016, **1**, 16142.
13. Q. Jiang, Y. Zhao, X. Zhang, X. Yang, Y. Chen, Z. Chu, Q. Ye, X. Li, Z. Yin and J. You, *Nature Photonics*, 2019, **13**, 460–466.
14. N. J. Jeon, H. Na, E. H. Jung, T.-Y. Yang, Y. G. Lee, G. Kim, H.-W. Shin, S. Il Seok, J. Lee and J. Seo, *Nature Energy*, 2018, **3**, 682-689.
15. W. S. Yang, B.-W. Park, E. H. Jung, N. J. Jeon, Y. C. Kim, D. U. Lee, S. S. Shin, J. Seo, E. K. Kim, J. H. Noh and S. I. Seok, *Science*, 2017, **356**, 1376-1379.

16. W. S. Yang, J. H. Noh, N. J. Jeon, Y. C. Kim, S. Ryu, J. Seo and S. I. Seok, *Science*, 2015, **348**, 1234-1237.
17. M. Abdi-Jalebi, Z. Andaji-Garmaroudi, S. Cacovich, C. Stavrakas, B. Philippe, J. M. Richter, M. Alsari, E. P. Booker, E. M. Hutter, A. J. Pearson, S. Lilliu, T. J. Savenije, H. Rensmo, G. Divitini, C. Ducati, R. H. Friend and S. D. Stranks, *Nature*, 2018, **555**, 497.
18. N. Ahn, D.-Y. Son, I.-H. Jang, S. M. Kang, M. Choi and N.-G. Park, *Journal of the American Chemical Society*, 2015, **137**, 8696-8699.
19. J. Burschka, N. Pellet, S.-J. Moon, R. Humphry-Baker, P. Gao, M. K. Nazeeruddin and M. Grätzel, *Nature*, 2013, **499**, 316.
20. A. Mei, X. Li, L. Liu, Z. Ku, T. Liu, Y. Rong, M. Xu, M. Hu, J. Chen, Y. Yang, M. Grätzel and H. Han, *Science*, 2014, **345**, 295-298.
21. E. H. Jung, N. J. Jeon, E. Y. Park, C. S. Moon, T. J. Shin, T.-Y. Yang, J. H. Noh and J. Seo, *Nature*, 2019, **567**, 511-515.
22. D. H. Kim, C. P. Muzzillo, J. Tong, A. F. Palmstrom, B. W. Larson, C. Choi, S. P. Harvey, S. Glynn, J. B. Whitaker, F. Zhang, Z. Li, H. Lu, M. F. A. M. van Hest, J. J. Berry, L. M. Mansfield, Y. Huang, Y. Yan and K. Zhu, *Joule*, 2019, **3**, 1734-1745.
23. W. Chen, Y. Wu, Y. Yue, J. Liu, W. Zhang, X. Yang, H. Chen, E. Bi, I. Ashraful, M. Grätzel and L. Han, *Science*, 2015, **350**, 944-948.
24. S. Yang, S. Chen, E. Mosconi, Y. Fang, X. Xiao, C. Wang, Y. Zhou, Z. Yu, J. Zhao, Y. Gao, F. De Angelis and J. Huang, *Science*, 2019, **365**, 473-478.
25. T. Niu, J. Lu, X. Jia, Z. Xu, M.-C. Tang, D. Barrit, N. Yuan, J. Ding, X. Zhang, Y. Fan, T. Luo, Y. Zhang, D.-M. Smilgies, Z. Liu, A. Amassian, S. Jin, K. Zhao and S. Liu, *Nano Letters*, 2019, **19**, 7181-7190.
26. A. R. b. M. Yusoff and M. K. Nazeeruddin, *Advanced Energy Materials*, 2018, **8**, 1702073.
27. M. Saliba, T. Matsui, J.-Y. Seo, K. Domanski, J.-P. Correa-Baena, M. K. Nazeeruddin, S. M. Zakeeruddin, W. Tress, A. Abate, A. Hagfeldt and M. Grätzel, *Energy & Environmental Science*, 2016, **9**, 1989-1997.
28. G. E. Eperon, T. Leijtens, K. A. Bush, R. Prasanna, T. Green, J. T.-W. Wang, D. P. McMeekin, G. Volonakis, R. L. Milot, R. May, A. Palmstrom, D. J. Slotcavage, R. A. Belisle, J. B. Patel, E. S. Parrott, R. J. Sutton, W. Ma, F. Moghadam, B. Conings, A. Babayigit, H.-G. Boyen, S. Bent, F. Giustino, L. M. Herz, M. B. Johnston, M. D. McGehee and H. J. Snaith, *Science*, 2016, **354**, 861-865.
29. A. Swarnkar, A. R. Marshall, E. M. Sanehira, B. D. Chernomordik, D. T. Moore, J. A. Christians, T. Chakrabarti and J. M. Luther, *Science*, 2016, **354**, 92-95.
30. Q. Zhao, A. Hazarika, X. Chen, S. P. Harvey, B. W. Larson, G. R. Teeter, J. Liu, T. Song, C. Xiao, L. Shaw, M. Zhang, G. Li, M. C. Beard and J. M. Luther, *Nature Communications*, 2019, **10**, 2842.
31. Z. Li, M. Yang, J.-S. Park, S.-H. Wei, J. J. Berry and K. Zhu, *Chemistry of Materials*, 2016, **28**, 284-292.
32. W. Travis, E. N. K. Glover, H. Bronstein, D. O. Scanlon and R. G. Palgrave, *Chemical Science*, 2016, **7**, 4548-4556.
33. X. Zheng, B. Chen, J. Dai, Y. Fang, Y. Bai, Y. Lin, H. Wei, Xiao C. Zeng and J. Huang, *Nature Energy*, 2017, **2**, 17102.
34. F. Zhang, D. Bi, N. Pellet, C. Xiao, Z. Li, J. J. Berry, S. M. Zakeeruddin, K. Zhu and M. Grätzel, *Energy & Environmental Science*, 2018, **11**, 3480-3490.
35. F. Zhang, W. Shi, J. Luo, N. Pellet, C. Yi, X. Li, X. Zhao, T. J. S. Dennis, X. Li, S. Wang, Y. Xiao, S. M. Zakeeruddin, D. Bi and M. Grätzel, *Advanced Materials*, 2017, **29**, 1606806.
36. M. Sun, F. Zhang, H. Liu, X. Li, Y. Xiao and S. Wang, *Journal of Materials Chemistry A*, 2017, **5**, 13448-13456.
37. J. A. Christians, P. Schulz, J. S. Tinkham, T. H. Schloemer, S. P. Harvey, B. J. Tremolet de Villers, A. Sellinger, J. J. Berry and J. M. Luther, *Nature Energy*, 2018, **3**, 68-74.

38. F. Zhang, Z. Wang, H. Zhu, N. Pellet, J. Luo, C. Yi, X. Liu, H. Liu, S. Wang, X. Li, Y. Xiao, S. M. Zakeeruddin, D. Bi and M. Grätzel, *Nano Energy*, 2017, **41**, 469-475.
39. J.-J. Guo, Z.-C. Bai, X.-F. Meng, M.-M. Sun, J.-H. Song, Z.-S. Shen, N. Ma, Z.-L. Chen and F. Zhang, *Solar Energy*, 2017, **155**, 121-129.
40. X. Liu, F. Zhang, Z. Liu, Y. Xiao, S. Wang and X. Li, *Journal of Materials Chemistry C*, 2017, **5**, 11429-11435.
41. Y. Bai, Q. Dong, Y. Shao, Y. Deng, Q. Wang, L. Shen, D. Wang, W. Wei and J. Huang, *Nature Communications*, 2016, **7**, 12806.
42. X. Zheng, J. Troughton, N. Gasparini, Y. Lin, M. Wei, Y. Hou, J. Liu, K. Song, Z. Chen, C. Yang, B. Turedi, A. Y. Alsalloum, J. Pan, J. Chen, A. A. Zhumekenov, T. D. Anthopoulos, Y. Han, D. Baran, O. F. Mohammed, E. H. Sargent and O. M. Bakr, *Joule*, 2019, **3**, 1963-1976.
43. F. Bella, G. Griffini, J.-P. Correa-Baena, G. Saracco, M. Grätzel, A. Hagfeldt, S. Turri and C. Gerbaldi, *Science*, 2016, **354**, 203-206.
44. Y. Jiang, L. Qiu, E. J. Juarez-Perez, L. K. Ono, Z. Hu, Z. Liu, Z. Wu, L. Meng, Q. Wang and Y. Qi, *Nature Energy*, 2019, **4**, 585–593.
45. F. Zhang, D. H. Kim and K. Zhu, *Current Opinion in Electrochemistry*, 2018, **11**, 105-113.
46. D. Thrithamarassery Gangadharan and D. Ma, *Energy & Environmental Science*, 2019, **12**, 2860-2889.
47. L. Etgar, *Energy & Environmental Science*, 2018, **11**, 234-242.
48. B. Saparov and D. B. Mitzi, *Chemical Reviews*, 2016, **116**, 4558-4596.
49. S. Yang, Y. Wang, P. Liu, Y.-B. Cheng, H. J. Zhao and H. G. Yang, *Nature Energy*, 2016, **1**, 15016.
50. I. C. Smith, E. T. Hoke, D. Solis-Ibarra, M. D. McGehee and H. I. Karunadasa, *Angewandte Chemie International Edition*, 2014, **53**, 11232-11235.
51. T. Luo, Y. Zhang, Z. Xu, T. Niu, J. Wen, J. Lu, S. Jin, S. Liu and K. Zhao, *Advanced Materials*, 2019, **31**, 1903848.
52. G. Grancini, C. Roldán-Carmona, I. Zimmermann, E. Mosconi, X. Lee, D. Martineau, S. Narbey, F. Oswald, F. De Angelis, M. Graetzel and M. K. Nazeeruddin, *Nature Communications*, 2017, **8**, 15684.
53. P. Chen, Y. Bai, M. Lyu, J.-H. Yun, M. Hao and L. Wang, *Solar RRL*, 2018, **2**, 1700186.
54. J. Tong, Z. Song, D. H. Kim, X. Chen, C. Chen, A. F. Palmstrom, P. F. Ndione, M. O. Reese, S. P. Dunfield, O. G. Reid, J. Liu, F. Zhang, S. P. Harvey, Z. Li, S. T. Christensen, G. Teeter, D. Zhao, M. M. Al-Jassim, M. F. A. M. van Hest, M. C. Beard, S. E. Shaheen, J. J. Berry, Y. Yan and K. Zhu, *Science*, 2019, **364**, 475-479.
55. Z. Wang, Q. Lin, F. P. Chmiel, N. Sakai, L. M. Herz and H. J. Snaith, *Nature Energy*, 2017, **2**, 17135.
56. C. Ortiz-Cervantes, P. Carmona-Monroy and D. Solis-Ibarra, *ChemSusChem*, 2019, **12**, 1560-1575.
57. F. Zhang, S. Wang, X. Li and Y. Xiao, *Current Nanoscience*, 2016, **12**, 137-156.
58. V. M. Goldschmidt, *Naturwissenschaften*, 1926, **14**, 477-485.
59. C. Li, X. Lu, W. Ding, L. Feng, Y. Gao and Z. Guo, *Acta Crystallographica Section B*, 2008, **64**, 702-707.
60. W. A. Dunlap-Shohl, Y. Zhou, N. P. Padture and D. B. Mitzi, *Chemical Reviews*, 2019, **119**, 3193-3295.
61. M. Yuan, L. N. Quan, R. Comin, G. Walters, R. Sabatini, O. Voznyy, S. Hoogland, Y. Zhao, E. M. Beauregard, P. Kanjanaboos, Z. Lu, D. H. Kim and E. H. Sargent, *Nature Nanotechnology*, 2016, **11**, 872.
62. N. Zhou, Y. Shen, L. Li, S. Tan, N. Liu, G. Zheng, Q. Chen and H. Zhou, *Journal of the American Chemical Society*, 2018, **140**, 459-465.
63. C. M. M. Soe, W. Nie, C. C. Stoumpos, H. Tsai, J.-C. Blancon, F. Liu, J. Even, T. J. Marks, A. D. Mohite and M. G. Kanatzidis, *Advanced Energy Materials*, 2018, **8**, 1700979.

64. T. Hu, M. D. Smith, E. R. Dohner, M.-J. Sher, X. Wu, M. T. Trinh, A. Fisher, J. Corbett, X. Y. Zhu, H. I. Karunadasa and A. M. Lindenberg, *The Journal of Physical Chemistry Letters*, 2016, **7**, 2258-2263.
65. L. Mao, C. C. Stoumpos and M. G. Kanatzidis, *Journal of the American Chemical Society*, 2019, **141**, 1171-1190.
66. B. Vargas, R. Torres-Cadena, J. Rodríguez-Hernández, M. Gembicky, H. Xie, J. Jiménez-Mier, Y.-S. Liu, E. Menéndez-Proupin, K. R. Dunbar, N. Lopez, P. Olalde-Velasco and D. Solis-Ibarra, *Chemistry of Materials*, 2018, **30**, 5315-5321.
67. C. C. Stoumpos, D. H. Cao, D. J. Clark, J. Young, J. M. Rondinelli, J. I. Jang, J. T. Hupp and M. G. Kanatzidis, *Chemistry of Materials*, 2016, **28**, 2852-2867.
68. W. Paritmongkol, N. S. Dahod, A. Stollmann, N. Mao, C. Settens, S.-L. Zheng and W. A. Tisdale, *Chemistry of Materials*, 2019, **31**, 5592-5607.
69. L. Mao, W. Ke, L. Pedesseau, Y. Wu, C. Katan, J. Even, M. R. Wasielewski, C. C. Stoumpos and M. G. Kanatzidis, *Journal of the American Chemical Society*, 2018, **140**, 3775-3783.
70. I.-H. Park, Q. Zhang, K. C. Kwon, Z. Zhu, W. Yu, K. Leng, D. Giovanni, H. S. Choi, I. Abdelwahab, Q.-H. Xu, T. C. Sum and K. P. Loh, *Journal of the American Chemical Society*, 2019, **141**, 15972-15976.
71. X. Li, W. Ke, B. Traoré, P. Guo, I. Hadar, M. Kepenekian, J. Even, C. Katan, C. C. Stoumpos, R. D. Schaller and M. G. Kanatzidis, *Journal of the American Chemical Society*, 2019, **141**, 12880-12890.
72. C. M. M. Soe, C. C. Stoumpos, M. Kepenekian, B. Traoré, H. Tsai, W. Nie, B. Wang, C. Katan, R. Seshadri, A. D. Mohite, J. Even, T. J. Marks and M. G. Kanatzidis, *Journal of the American Chemical Society*, 2017, **139**, 16297-16309.
73. Y. Zhang, P. Wang, M.-C. Tang, D. Barrit, W. Ke, J. Liu, T. Luo, Y. Liu, T. Niu, D.-M. Smilgies, Z. Yang, Z. Liu, S. Jin, M. G. Kanatzidis, A. Amassian, S. F. Liu and K. Zhao, *Journal of the American Chemical Society*, 2019, **141**, 2684-2694.
74. S. Ahmad, P. Fu, S. Yu, Q. Yang, X. Liu, X. Wang, X. Wang, X. Guo and C. Li, *Joule*, 2019, **3**, 794-806.
75. T. Nakajima, H. Yamauchi, T. Goto, M. Yoshizawa, T. Suzuki and T. Fujimura, *Journal of Magnetism and Magnetic Materials*, 1983, **31-34**, 1189-1190.
76. L. Mao, Y. Wu, C. C. Stoumpos, B. Traore, C. Katan, J. Even, M. R. Wasielewski and M. G. Kanatzidis, *Journal of the American Chemical Society*, 2017, **139**, 11956-11963.
77. B. Doudin and G. Chapuis, *Acta Crystallographica Section B*, 1990, **46**, 180-186.
78. E. R. Peterson and R. D. Willett, *The Journal of Chemical Physics*, 1972, **56**, 1879-1882.
79. C. C. Stoumpos, C. M. M. Soe, H. Tsai, W. Nie, J.-C. Blancon, D. H. Cao, F. Liu, B. Traoré, C. Katan, J. Even, A. D. Mohite and M. G. Kanatzidis, *Chem*, 2017, **2**, 427-440.
80. P. Cheng, P. Wang, Z. Xu, X. Jia, Q. Wei, N. Yuan, J. Ding, R. Li, G. Zhao, Y. Cheng, K. Zhao and S. F. Liu, *ACS Energy Letters*, 2019, **4**, 1830-1838.
81. D. G. Billing and A. Lemmerer, *Acta Crystallographica Section B*, 2007, **63**, 735-747.
82. A. Lemmerer and D. G. Billing, *Dalton Transactions*, 2012, **41**, 1146-1157.
83. W.-W. Zhong, Y.-Y. Di, Y.-X. Kong, D.-F. Lu and J.-M. Dou, *The Journal of Chemical Thermodynamics*, 2014, **72**, 100-107.
84. H. Ren, S. Yu, L. Chao, Y. Xia, Y. Sun, S. Zuo, F. Li, T. Niu, Y. Yang, H. Ju, B. Li, H. Du, X. Gao, J. Zhang, J. Wang, L. Zhang, Y. Chen and W. Huang, *Nature Photonics*, 2020, DOI: 10.1038/s41566-019-0572-6.
85. A. H. Proppe, R. Quintero-Bermudez, H. Tan, O. Voznyy, S. O. Kelley and E. H. Sargent, *Journal of the American Chemical Society*, 2018, **140**, 2890-2896.
86. D. Solis-Ibarra and H. I. Karunadasa, *Angewandte Chemie International Edition*, 2014, **53**, 1039-1042.
87. C. Lermer, S. T. Birkhold, I. L. Moudrakovski, P. Mayer, L. M. Schoop, L. Schmidt-Mende and B. V. Lotsch, *Chemistry of Materials*, 2016, **28**, 6560-6566.

88. Z.-X. Wang, W.-Q. Liao, H.-Y. Ye and Y. Zhang, *Dalton Transactions*, 2015, **44**, 20406-20412.
89. N. Mercier, *CrystEngComm*, 2005, **7**, 429-432.
90. N. Ashari-Astani, F. Jahanbakhshi, M. Mladenović, A. Q. M. Alanazi, I. Ahmadabadi, M. R. Ejtehadi, M. I. Dar, M. Grätzel and U. Rothlisberger, *The Journal of Physical Chemistry Letters*, 2019, **10**, 3543-3549.
91. A. Lemmerer and D. G. Billing, *CrystEngComm*, 2010, **12**, 1290-1301.
92. D. G. Billing and A. Lemmerer, *CrystEngComm*, 2009, **11**, 1549-1562.
93. D. G. Billing and A. Lemmerer, *CrystEngComm*, 2007, **9**, 236-244.
94. X.-N. Li, P.-F. Li, W.-Q. Liao, J.-Z. Ge, D.-H. Wu and H.-Y. Ye, *European Journal of Inorganic Chemistry*, 2017, **2017**, 938-942.
95. D. G. Billing and A. Lemmerer, *Acta Crystallographica Section C*, 2006, **62**, m269-m271.
96. G. S. Lorena, H. Hasegawa, Y. Takahashi, J. Harada and T. Inabe, *Chemistry Letters*, 2014, **43**, 1535-1537.
97. Y. Takahashi, R. Obara, K. Nakagawa, M. Nakano, J.-y. Tokita and T. Inabe, *Chemistry of Materials*, 2007, **19**, 6312-6316.
98. Z. Li, N. Liu, K. Meng, Z. Liu, Y. Hu, Q. Xu, X. Wang, S. Li, L. Cheng and G. Chen, *Nano Letters*, 2019, **19**, 5237-5245.
99. L. Mao, H. Tsai, W. Nie, L. Ma, J. Im, C. C. Stoumpos, C. D. Malliakas, F. Hao, M. R. Wasielewski, A. D. Mohite and M. G. Kanatzidis, *Chemistry of Materials*, 2016, **28**, 7781-7792.
100. B.-E. Cohen, M. Wierzbowska and L. Etgar, *Sustainable Energy & Fuels*, 2017, **1**, 1935-1943.
101. M. E. Kamminga, H.-H. Fang, M. R. Filip, F. Giustino, J. Baas, G. R. Blake, M. A. Loi and T. T. M. Palstra, *Chemistry of Materials*, 2016, **28**, 4554-4562.
102. M. Braun and W. Frey, *Zeitschrift für Kristallographie - New Crystal Structures*, 1999, **214**, 331-332.
103. W.-Q. Liao, Y. Zhang, C.-L. Hu, J.-G. Mao, H.-Y. Ye, P.-F. Li, S. D. Huang and R.-G. Xiong, *Nature Communications*, 2015, **6**, 7338.
104. Y. Jin, C.-H. Yu and W. Zhang, *Journal of Coordination Chemistry*, 2014, **67**, 1156-1173.
105. J. Calabrese, N. L. Jones, R. L. Harlow, N. Herron, D. L. Thorn and Y. Wang, *Journal of the American Chemical Society*, 1991, **113**, 2328-2330.
106. F. Zhang, D. H. Kim, H. Lu, J.-S. Park, B. W. Larson, J. Hu, L. Gao, C. Xiao, O. G. Reid, X. Chen, Q. Zhao, P. F. Ndione, J. J. Berry, W. You, A. Walsh, M. C. Beard and K. Zhu, *Journal of the American Chemical Society*, 2019, **141**, 5972-5979.
107. G. C. Papavassiliou, I. B. Koutselas, A. Terzis and M. H. Whangbo, *Solid State Communications*, 1994, **91**, 695-698.
108. D. B. Mitzi, *Journal of Solid State Chemistry*, 1999, **145**, 694-704.
109. G. C. Papavassiliou, G. A. Mousdis, C. P. Raptopoulou and A. Terzis, *Zeitschrift für Naturforschung B*, 2000, **55**, 536.
110. H. Dammak, S. Elleuch, H. Feki and Y. Abid, *Solid State Sciences*, 2016, **61**, 1-8.
111. H. Pan, X. Zhao, X. Gong, Y. Shen and M. Wang, *The Journal of Physical Chemistry Letters*, 2019, **10**, 1813-1819.
112. W. Fu, H. Liu, X. Shi, L. Zuo, X. Li and A. K.-Y. Jen, *Advanced Functional Materials*, 2019, **29**, 1900221.
113. K. Kikuchi, Y. Takeoka, M. Rikukawa and K. Sanui, *Current Applied Physics*, 2004, **4**, 599-602.
114. J. Hu, I. W. H. Oswald, H. Hu, S. J. Stuard, M. M. Nahid, L. Yan, Z. Chen, H. Ade, J. R. Neilson and W. You, *ACS Materials Letters*, 2019, **1**, 171-176.
115. I.-H. Park, L. Chu, K. Leng, Y. F. Choy, W. Liu, I. Abdelwahab, Z. Zhu, Z. Ma, W. Chen, Q.-H. Xu, G. Eda and K. P. Loh, *Advanced Functional Materials*, 2019, **29**, 1904810.
116. X.-H. Zhu, N. Mercier, A. Riou, P. Blanchard and P. Frère, *Chemical Communications*, 2002, 2160-2161.

117. Y. Gao, E. Shi, S. Deng, S. B. Shiring, J. M. Snaider, C. Liang, B. Yuan, R. Song, S. M. Janke, A. Liebman-Peláez, P. Yoo, M. Zeller, B. W. Boudouris, P. Liao, C. Zhu, V. Blum, Y. Yu, B. M. Savoie, L. Huang and L. Dou, *Nature Chemistry*, 2019, **11**, 1151-1157.
118. K.-z. Du, Q. Tu, X. Zhang, Q. Han, J. Liu, S. Zauscher and D. B. Mitzi, *Inorganic Chemistry*, 2017, **56**, 9291-9302.
119. J. V. Passarelli, D. J. Fairfield, N. A. Sather, M. P. Hendricks, H. Sai, C. L. Stern and S. I. Stupp, *Journal of the American Chemical Society*, 2018, **140**, 7313-7323.
120. R. Herckens, W. T. M. Van Gompel, W. Song, M. C. Gélvez-Rueda, A. Maufort, B. Ruttens, J. D'Haen, F. C. Grozema, T. Aernouts, L. Lutsen and D. Vanderzande, *Journal of Materials Chemistry A*, 2018, **6**, 22899-22908.
121. A. B. Corradi, A. M. Ferrari, G. C. Pellacani, A. Saccani, F. Sandrolini and P. Sgarabotto, *Inorganic Chemistry*, 1999, **38**, 716-721.
122. M. D. Smith, A. Jaffe, E. R. Dohner, A. M. Lindenberg and H. I. Karunadasa, *Chemical Science*, 2017, **8**, 4497-4504.
123. M. Amami, R. Zouari, A. Ben Salah and H. Burzlaff, *Acta Crystallographica Section E*, 2002, **58**, m357-m359.
124. M. Safdari, P. H. Svensson, M. T. Hoang, I. Oh, L. Kloo and J. M. Gardner, *Journal of Materials Chemistry A*, 2016, **4**, 15638-15646.
125. X. Li, J. Hoffman, W. Ke, M. Chen, H. Tsai, W. Nie, A. D. Mohite, M. Kepenekian, C. Katan, J. Even, M. R. Wasielewski, C. C. Stoumpos and M. G. Kanatzidis, *Journal of the American Chemical Society*, 2018, **140**, 12226-12238.
126. A. Lemmerer and D. G. Billing, *CrystEngComm*, 2012, **14**, 1954-1966.
127. K. Pradeesh, G. S. Yadav, M. Singh and G. Vijaya Prakash, *Materials Chemistry and Physics*, 2010, **124**, 44-47.
128. E. R. Dohner, E. T. Hoke and H. I. Karunadasa, *Journal of the American Chemical Society*, 2014, **136**, 1718-1721.
129. L. Mao, Y. Wu, C. C. Stoumpos, M. R. Wasielewski and M. G. Kanatzidis, *Journal of the American Chemical Society*, 2017, **139**, 5210-5215.
130. M. Daub and H. Hillebrecht, *Journal*, 2018, **233**, 555.
131. N. Louvain, W. Bi, N. Mercier, J.-Y. Buzaré, C. Legein and G. Corbel, *Dalton Transactions*, 2007, DOI: 10.1039/B617225C, 965-970.
132. E. R. Dohner, A. Jaffe, L. R. Bradshaw and H. I. Karunadasa, *Journal of the American Chemical Society*, 2014, **136**, 13154-13157.
133. Y. Li, G. Zheng and J. Lin, *European Journal of Inorganic Chemistry*, 2008, **2008**, 1689-1692.
134. A. Bonamartini Corradi, A. M. Ferrari, L. Righi and P. Sgarabotto, *Inorganic Chemistry*, 2001, **40**, 218-223.
135. M. K. Rayner and D. G. Billing, *Acta Crystallographica Section E*, 2010, **66**, m660.
136. D. B. Mitzi, C. D. Dimitrakopoulos and L. L. Kosbar, *Chemistry of Materials*, 2001, **13**, 3728-3740.
137. H. Yu, Z. Wei, Y. Hao, Z. Liang, Z. Fu and H. Cai, *New Journal of Chemistry*, 2017, **41**, 9586-9589.
138. M. P. Hautzinger, J. Dai, Y. Ji, Y. Fu, J. Chen, I. A. Guzei, J. C. Wright, Y. Li and S. Jin, *Inorganic Chemistry*, 2017, **56**, 14991-14998.
139. Y. Li, J. V. Milić, A. Ummadisingu, J.-Y. Seo, J.-H. Im, H.-S. Kim, Y. Liu, M. I. Dar, S. M. Zakeeruddin, P. Wang, A. Hagfeldt and M. Grätzel, *Nano Letters*, 2019, **19**, 150-157.
140. Y. Li, G. Zheng, C. Lin and J. Lin, *Crystal Growth & Design*, 2008, **8**, 1990-1996.
141. C. Lermer, S. P. Harm, S. T. Birkhold, J. A. Jaser, C. M. Kutz, P. Mayer, L. Schmidt-Mende and B. V. Lotsch, *Zeitschrift für anorganische und allgemeine Chemie*, 2016, **642**, 1369-1376.
142. X.-H. Zhu, N. Mercier, P. Frère, P. Blanchard, J. Roncali, M. Allain, C. Pasquier and A. Riou, *Inorganic Chemistry*, 2003, **42**, 5330-5339.
143. D. B. Mitzi, K. Chondroudis and C. R. Kagan, *Inorganic Chemistry*, 1999, **38**, 6246-6256.

144. K. Zheng and T. Pullerits, *The Journal of Physical Chemistry Letters*, 2019, **10**, 5881-5885.
145. X. Hong, T. Ishihara and A. V. Nurmikko, *Physical Review B*, 1992, **45**, 6961-6964.
146. Z. Guo, X. Wu, T. Zhu, X. Zhu and L. Huang, *ACS Nano*, 2016, **10**, 9992-9998.
147. R. L. Milot, R. J. Sutton, G. E. Eperon, A. A. Haghighirad, J. Martinez Hardigree, L. Miranda, H. J. Snaith, M. B. Johnston and L. M. Herz, *Nano Letters*, 2016, **16**, 7001-7007.
148. P. Gao, A. R. Bin Mohd Yusoff and M. K. Nazeeruddin, *Nature Communications*, 2018, **9**, 5028.
149. J. A. Sichert, Y. Tong, N. Mutz, M. Vollmer, S. Fischer, K. Z. Milowska, R. García Cortadella, B. Nickel, C. Cardenas-Daw, J. K. Stolarczyk, A. S. Urban and J. Feldmann, *Nano Letters*, 2015, **15**, 6521-6527.
150. D. H. Cao, C. C. Stoumpos, O. K. Farha, J. T. Hupp and M. G. Kanatzidis, *Journal of the American Chemical Society*, 2015, **137**, 7843-7850.
151. Q. Zhang, R. Su, W. Du, X. Liu, L. Zhao, S. T. Ha and Q. Xiong, *Small Methods*, 2017, **1**, 1700163.
152. J. S. Manser, J. A. Christians and P. V. Kamat, *Chemical Reviews*, 2016, **116**, 12956-13008.
153. T. M. Koh, V. Shanmugam, J. Schlipf, L. Oesinghaus, P. Müller-Buschbaum, N. Ramakrishnan, V. Swamy, N. Mathews, P. P. Boix and S. G. Mhaisalkar, *Advanced Materials*, 2016, **28**, 3653-3661.
154. H. Tsai, W. Nie, J.-C. Blancon, C. C. Stoumpos, R. Asadpour, B. Harutyunyan, A. J. Neukirch, R. Verduzco, J. J. Crochet, S. Tretiak, L. Pedesseau, J. Even, M. A. Alam, G. Gupta, J. Lou, P. M. Ajayan, M. J. Bedzyk, M. G. Kanatzidis and A. D. Mohite, *Nature*, 2016, **536**, 312.
155. F. Li, Y. Pei, F. Xiao, T. Zeng, Z. Yang, J. Xu, J. Sun, B. Peng and M. Liu, *Nanoscale*, 2018, **10**, 6318-6322.
156. X. Zhang, X. Ren, B. Liu, R. Munir, X. Zhu, D. Yang, J. Li, Y. Liu, D.-M. Smilgies, R. Li, Z. Yang, T. Niu, X. Wang, A. Amassian, K. Zhao and S. Liu, *Energy & Environmental Science*, 2017, **10**, 2095-2102.
157. Y. Jiang, X. He, T. Liu, N. Zhao, M. Qin, J. Liu, F. Jiang, F. Qin, L. Sun, X. Lu, S. Jin, Z. Xiao, T. Kamiya and Y. Zhou, *ACS Energy Letters*, 2019, **4**, 1216-1224.
158. D. B. Straus, S. Hurtado Parra, N. Iotov, J. Gebhardt, A. M. Rappe, J. E. Subotnik, J. M. Kikkawa and C. R. Kagan, *Journal of the American Chemical Society*, 2016, **138**, 13798-13801.
159. A. Brehier, R. Parashkov, J. S. Lauret and E. Deleporte, *Applied Physics Letters*, 2006, **89**, 171110.
160. M. Braun, W. Tuffentsammer, H. Wachtel and H. C. Wolf, *Chemical Physics Letters*, 1999, **303**, 157-164.
161. K. Ema, M. Inomata, Y. Kato, H. Kunugita and M. Era, *Physical Review Letters*, 2008, **100**, 257401.
162. J. Liu, J. Leng, K. Wu, J. Zhang and S. Jin, *Journal of the American Chemical Society*, 2017, **139**, 1432-1435.
163. Y. Chen, S. Yu, Y. Sun and Z. Liang, *The Journal of Physical Chemistry Letters*, 2018, **9**, 2627-2631.
164. C. Ma, D. Shen, T.-W. Ng, M.-F. Lo and C.-S. Lee, *Advanced Materials*, 2018, **30**, 1800710.
165. J. Zhang, L. Zhang, X. Li, X. Zhu, J. Yu and K. Fan, *ACS Sustainable Chemistry & Engineering*, 2019, **7**, 3487-3495.
166. J. Qiu, Y. Zheng, Y. Xia, L. Chao, Y. Chen and W. Huang, *Advanced Functional Materials*, 2019, **29**, 1806831.
167. L. Gao, F. Zhang, C. Xiao, X. Chen, B. W. Larson, J. J. Berry and K. Zhu, *Advanced Functional Materials*, 2019, **29**, 1901652.
168. C. J. Dahlman, R. A. DeCrescent, N. R. Venkatesan, R. M. Kennard, G. Wu, M. A. Everest, J. A. Schuller and M. L. Chabinyc, *Chemistry of Materials*, 2019, **31**, 5832-5844.
169. X. Lian, J. Chen, Y. Zhang, S. Tian, M. Qin, J. Li, T. R. Andersen, G. Wu, X. Lu and H. Chen, *Journal of Materials Chemistry A*, 2019, **7**, 18980-18986.

170. W. Fu, J. Wang, L. Zuo, K. Gao, F. Liu, D. S. Ginger and A. K. Y. Jen, *ACS Energy Letters*, 2018, **3**, 2086-2093.
171. X. Zhang, G. Wu, S. Yang, W. Fu, Z. Zhang, C. Chen, W. Liu, J. Yan, W. Yang and H. Chen, *Small*, 2017, **13**, 1700611.
172. J. Qing, X.-K. Liu, M. Li, F. Liu, Z. Yuan, E. Tiukalova, Z. Yan, M. Duchamp, S. Chen, Y. Wang, S. Bai, J.-M. Liu, H. J. Snaith, C.-S. Lee, T. C. Sum and F. Gao, *Advanced Energy Materials*, 2018, **8**, 1800185.
173. H. J. Jung, C. C. Stompus, M. G. Kanatzidis and V. P. Dravid, *Nano Letters*, 2019, **19**, 6109-6117.
174. Y. Chen, Y. Sun, J. Peng, W. Zhang, X. Su, K. Zheng, T. Pullerits and Z. Liang, *Advanced Energy Materials*, 2017, **7**, 1700162.
175. L. Gao, F. Zhang, X. Chen, C. Xiao, B. W. Larson, S. P. Dunfield, J. J. Berry and K. Zhu, *Angewandte Chemie*, 2019, **131**, 11863-11867.
176. B. Febriansyah, T. M. Koh, Y. Lekina, N. F. Jamaludin, A. Bruno, R. Ganguly, Z. X. Shen, S. G. Mhaisalkar and J. England, *Chemistry of Materials*, 2019, **31**, 890-898.
177. J. V. Milić, J.-H. Im, D. J. Kubicki, A. Ummadisingu, J.-Y. Seo, Y. Li, M. A. Ruiz-Preciado, M. I. Dar, S. M. Zakeeruddin, L. Emsley and M. Grätzel, *Advanced Energy Materials*, 2019, **9**, 1900284.
178. H. Gu, C. Liang, Y. Xia, Q. Wei, T. Liu, Y. Yang, W. Hui, H. Chen, T. Niu, L. Chao, Z. Wu, X. Xie, J. Qiu, G. Shao, X. Gao, G. Xing, Y. Chen and W. Huang, *Nano Energy*, 2019, **65**, 104050.
179. C. Zuo, A. D. Scully, D. Vak, W. Tan, X. Jiao, C. R. McNeill, D. Angmo, L. Ding and M. Gao, *Advanced Energy Materials*, 2019, **9**, 1803258.
180. G. Wu, X. Li, J. Zhou, J. Zhang, X. Zhang, X. Leng, P. Wang, M. Chen, D. Zhang, K. Zhao, S. Liu, H. Zhou and Y. Zhang, *Advanced Materials*, 2019, **31**, 1903889.
181. J. Zhang, J. Qin, M. Wang, Y. Bai, H. Zou, J. K. Keum, R. Tao, H. Xu, H. Yu, S. Haacke and B. Hu, *Joule*, 2019, **3**, 3061-3071.
182. X. Zhang, G. Wu, W. Fu, M. Qin, W. Yang, J. Yan, Z. Zhang, X. Lu and H. Chen, *Advanced Energy Materials*, 2018, **8**, 1702498.
183. M. Kim, G.-H. Kim, T. K. Lee, I. W. Choi, H. W. Choi, Y. Jo, Y. J. Yoon, J. W. Kim, J. Lee, D. Huh, H. Lee, S. K. Kwak, J. Y. Kim and D. S. Kim, *Joule*, 2019, **3**, 2179-2192.
184. Y. Zhao and K. Zhu, *The Journal of Physical Chemistry C*, 2014, **118**, 9412-9418.
185. H. Lai, B. Kan, T. Liu, N. Zheng, Z. Xie, T. Zhou, X. Wan, X. Zhang, Y. Liu and Y. Chen, *Journal of the American Chemical Society*, 2018, **140**, 11639-11646.
186. T. Niu, H. Ren, B. Wu, Y. Xia, X. Xie, Y. Yang, X. Gao, Y. Chen and W. Huang, *The Journal of Physical Chemistry Letters*, 2019, **10**, 2349-2356.
187. X. Lian, J. Chen, M. Qin, Y. Zhang, S. Tian, X. Lu, G. Wu and H. Chen, *Angewandte Chemie International Edition*, 2019, **58**, 9409-9413.
188. X. Lian, J. Chen, Y. Zhang, M. Qin, T. R. Andersen, J. Ling, G. Wu, X. Lu, D. Yang and H. Chen, *Journal of Materials Chemistry A*, 2019, **7**, 19423-19429.
189. X. Lian, J. Chen, Y. Zhang, M. Qin, J. Li, S. Tian, W. Yang, X. Lu, G. Wu and H. Chen, *Advanced Functional Materials*, 2019, **29**, 1807024.
190. Y. Zhang, J. Chen, X. Lian, M. Qin, J. Li, T. R. Andersen, X. Lu, G. Wu, H. Li and H. Chen, *Small Methods*, 2019, **3**, 1900375.
191. C. Yi, J. Luo, S. Meloni, A. Boziki, N. Ashari-Astani, C. Grätzel, S. M. Zakeeruddin, U. Röthlisberger and M. Grätzel, *Energy & Environmental Science*, 2016, **9**, 656-662.
192. L. T. Schelhas, Z. Li, J. A. Christians, A. Goyal, P. Kairys, S. P. Harvey, D. H. Kim, K. H. Stone, J. M. Luther, K. Zhu, V. Stevanovic and J. J. Berry, *Energy & Environmental Science*, 2019, **12**, 1341-1348.
193. D. Ramirez, K. Schutt, Z. Wang, A. J. Pearson, E. Ruggeri, H. J. Snaith, S. D. Stranks and F. Jaramillo, *ACS Energy Letters*, 2018, **3**, 2246-2251.

194. J. Hu, I. W. H. Oswald, S. J. Stuard, M. M. Nahid, N. Zhou, O. F. Williams, Z. Guo, L. Yan, H. Hu, Z. Chen, X. Xiao, Y. Lin, Z. Yang, J. Huang, A. M. Moran, H. Ade, J. R. Neilson and W. You, *Nature Communications*, 2019, **10**, 1276.
195. Y. Li, H. Cheng, K. Zhao and Z.-S. Wang, *ACS Applied Materials & Interfaces*, 2019, **11**, 37804-37811.
196. C. Katan, L. Pedesseau, M. Kepenekian, A. Rolland and J. Even, *Journal of Materials Chemistry A*, 2015, **3**, 9232-9240.
197. P. Li, C. Liang, X.-L. Liu, F. Li, Y. Zhang, X.-T. Liu, H. Gu, X. Hu, G. Xing, X. Tao and Y. Song, *Advanced Materials*, 2019, **31**, 1901966.
198. A. Krishna, S. Gottis, M. K. Nazeeruddin and F. Sauvage, *Advanced Functional Materials*, 2019, **29**, 1806482.
199. K. Yao, X. Wang, F. Li and L. Zhou, *Chemical Communications*, 2015, **51**, 15430-15433.
200. J. Chen, D. Lee and N.-G. Park, *ACS Applied Materials & Interfaces*, 2017, **9**, 36338-36349.
201. S. V. Morozov, D. I. Kryzhkov, A. N. Yablonsky, A. V. Antonov, D. I. Kuritsin, D. M. Gaponova, Y. G. Sadofyev, N. Samal, V. I. Gavrilenko and Z. F. Krasilnik, *Journal of Applied Physics*, 2013, **113**, 163107.
202. G. Liu, H. Zheng, X. Xu, S. Xu, X. Zhang, X. Pan and S. Dai, *Advanced Functional Materials*, 2019, **29**, 1807565.
203. Y. Wang, H. Xu, F. Wang, D. Liu, H. Chen, H. Zheng, L. Ji, P. Zhang, T. Zhang, Z. D. Chen, J. Wu, L. Chen and S. Li, *Chemical Engineering Journal*, 2019, DOI: https://doi.org/10.1016/j.cej.2019.123589, 123589.
204. L. Zhou, Z. Lin, Z. Ning, T. Li, X. Guo, J. Ma, J. Su, C. Zhang, J. Zhang, S. Liu, J. Chang and Y. Hao, *Solar RRL*, 2019, **3**, 1900293.
205. T. Zhou, H. Lai, T. Liu, D. Lu, X. Wan, X. Zhang, Y. Liu and Y. Chen, *Advanced Materials*, 2019, **31**, 1901242.
206. S. Heo, G. Seo, K. T. Cho, Y. Lee, S. Paek, S. Kim, M. Seol, S. H. Kim, D.-J. Yun, K. Kim, J. Park, J. Lee, L. Lechner, T. Rodgers, J. W. Chung, J.-S. Kim, D. Lee, S.-H. Choi and M. K. Nazeeruddin, *Advanced Energy Materials*, 2019, **9**, 1902470.
207. C.-T. Lin, J. Lee, J. Kim, T. J. Macdonald, J. Ngiam, B. Xu, M. Daboczi, W. Xu, S. Pont, B. Park, H. Kang, J.-S. Kim, D. J. Payne, K. Lee, J. R. Durrant and M. A. McLachlan, *Advanced Functional Materials*, **n/a**, 1906763.
208. E. Shirzadi, A. Mahata, C. Roldán Carmona, F. De Angelis, P. J. Dyson and M. K. Nazeeruddin, *ACS Energy Letters*, 2019, **4**, 2989-2994.
209. H. Chen, Q. Wei, M. I. Saidaminov, F. Wang, A. Johnston, Y. Hou, Z. Peng, K. Xu, W. Zhou, Z. Liu, L. Qiao, X. Wang, S. Xu, J. Li, R. Long, Y. Ke, E. H. Sargent and Z. Ning, *Advanced Materials*, 2019, **31**, 1903559.
210. B.-E. Cohen, Y. Li, Q. Meng and L. Etgar, *Nano Letters*, 2019, **19**, 2588-2597.
211. L. Iagher and L. Etgar, *ACS Energy Letters*, 2018, **3**, 366-372.
212. N. D. Pham, C. Zhang, V. T. Tiong, S. Zhang, G. Will, A. Bou, J. Bisquert, P. E. Shaw, A. Du, G. J. Wilson and H. Wang, *Advanced Functional Materials*, 2019, **29**, 1806479.
213. N. De Marco, H. Zhou, Q. Chen, P. Sun, Z. Liu, L. Meng, E.-P. Yao, Y. Liu, A. Schiffer and Y. Yang, *Nano Letters*, 2016, **16**, 1009-1016.
214. D. J. Kubicki, D. Prochowicz, A. Hofstetter, M. Saski, P. Yadav, D. Bi, N. Pellet, J. Lewiński, S. M. Zakeeruddin, M. Grätzel and L. Emsley, *Journal of the American Chemical Society*, 2018, **140**, 3345-3351.
215. A. D. Jodlowski, C. Roldán-Carmona, G. Grancini, M. Salado, M. Ralaiarisoa, S. Ahmad, N. Koch, L. Camacho, G. de Miguel and M. K. Nazeeruddin, *Nature Energy*, 2017, **2**, 972-979.
216. R. J. Stoddard, A. Rajagopal, R. L. Palmer, I. L. Braly, A. K. Y. Jen and H. W. Hillhouse, *ACS Energy Letters*, 2018, **3**, 1261-1268.
217. L. Hong, J. Milic, P. Ahlawat, M. Mladenovic, D. J. Kubicki, F. Jahanbakhshi, D. Ren, M. Gelvez-Rueda, M. A. Ruiz-Preciado, A. Ummadisingu, Y. Liu, C. Tian, L. Pan, S. M.

Zakeeruddin, A. Hagfeldt, F. C. Grozema, U. Rothlisberger, L. Emsley, H. Han and M. Grätzel, *Angewandte Chemie International Edition*, 2019, **n/a**.
218. S. Wu, Z. Li, J. Zhang, T. Liu, Z. Zhu and A. K. Y. Jen, *Chemical Communications*, 2019, **55**, 4315-4318.
219. A. Thote, I. Jeon, J.-W. Lee, S. Seo, H.-S. Lin, Y. Yang, H. Daiguji, S. Maruyama and Y. Matsuo, *ACS Applied Energy Materials*, 2019, **2**, 2486-2493.
220. T. Zhang, M. I. Dar, G. Li, F. Xu, N. Guo, M. Grätzel and Y. Zhao, *Science Advances*, 2017, **3**, e1700841.
221. Y. Jiang, J. Yuan, Y. Ni, J. Yang, Y. Wang, T. Jiu, M. Yuan and J. Chen, *Joule*, 2018, **2**, 1356-1368.
222. J.-W. Lee, Z. Dai, T.-H. Han, C. Choi, S.-Y. Chang, S.-J. Lee, N. De Marco, H. Zhao, P. Sun, Y. Huang and Y. Yang, *Nature Communications*, 2018, **9**, 3021.
223. D. S. Lee, J. S. Yun, J. Kim, A. M. Soufiani, S. Chen, Y. Cho, X. Deng, J. Seidel, S. Lim, S. Huang and A. W. Y. Ho-Baillie, *ACS Energy Letters*, 2018, **3**, 647-654.
224. T. Niu, J. Lu, M.-C. Tang, D. Barrit, D.-M. Smilgies, Z. Yang, J. Li, Y. Fan, T. Luo, I. McCulloch, A. Amassian, S. Liu and K. Zhao, *Energy & Environmental Science*, 2018, **11**, 3358-3366.
225. X. Huang, Q. Cui, W. Bi, L. Li, P. Jia, Y. Hou, Y. Hu, Z. Lou and F. Teng, *RSC Advances*, 2019, **9**, 7984-7991.
226. T. M. Koh, V. Shanmugam, X. Guo, S. S. Lim, O. Filonik, E. M. Herzig, P. Müller-Buschbaum, V. Swamy, S. T. Chien, S. G. Mhaisalkar and N. Mathews, *Journal of Materials Chemistry A*, 2018, **6**, 2122-2128.
227. B. Liu, M. Long, M. Cai, L. Ding and J. Yang, *Nano Energy*, 2019, **59**, 715-720.
228. S. G. Motti, T. Crothers, R. Yang, Y. Cao, R. Li, M. B. Johnston, J. Wang and L. M. Herz, *Nano Letters*, 2019, **19**, 3953-3960.
229. K. T. Cho, G. Grancini, Y. Lee, E. Oveisi, J. Ryu, O. Almora, M. Tschumi, P. A. Schouwink, G. Seo, S. Heo, J. Park, J. Jang, S. Paek, G. Garcia-Belmonte and M. K. Nazeeruddin, *Energy & Environmental Science*, 2018, **11**, 952-959.
230. P. Chen, Y. Bai, S. Wang, M. Lyu, J.-H. Yun and L. Wang, *Advanced Functional Materials*, 2018, **28**, 1706923.
231. Q. Zhou, L. Liang, J. Hu, B. Cao, L. Yang, T. Wu, X. Li, B. Zhang and P. Gao, *Advanced Energy Materials*, 2019, **9**, 1802595.
232. H. Min, M. Kim, S.-U. Lee, H. Kim, G. Kim, K. Choi, J. H. Lee and S. I. Seok, *Science*, 2019, **366**, 749-753.
233. Y. Liu, S. Akin, L. Pan, R. Uchida, N. Arora, J. V. Milić, A. Hinderhofer, F. Schreiber, A. R. Uhl, S. M. Zakeeruddin, A. Hagfeldt, M. I. Dar and M. Grätzel, *Science Advances*, 2019, **5**, eaaw2543.
234. C. Ma, C. Leng, Y. Ji, X. Wei, K. Sun, L. Tang, J. Yang, W. Luo, C. Li, Y. Deng, S. Feng, J. Shen, S. Lu, C. Du and H. Shi, *Nanoscale*, 2016, **8**, 18309-18314.
235. H. Kim, S.-U. Lee, D. Y. Lee, M. J. Paik, H. Na, J. Lee and S. I. Seok, *Advanced Energy Materials*, 2019, **9**, 1902740.
236. J. Chen, J.-Y. Seo and N.-G. Park, *Advanced Energy Materials*, 2018, **8**, 1702714.
237. S. Gharibzadeh, B. Abdollahi Nejand, M. Jakoby, T. Abzieher, D. Hauschild, S. Moghadamzadeh, J. A. Schwenzer, P. Brenner, R. Schmager, A. A. Haghighirad, L. Weinhardt, U. Lemmer, B. S. Richards, I. A. Howard and U. W. Paetzold, *Advanced Energy Materials*, 2019, **9**, 1803699.
238. M. S. de Holanda, R. Szostak, P. E. Marchezi, L. G. T. A. Duarte, J. C. Germino, T. D. Z. Atvars and A. F. Nogueira, *Solar RRL*, 2019, **3**, 1900199.
239. K. T. Cho, Y. Zhang, S. Orlandi, M. Cavazzini, I. Zimmermann, A. Lesch, N. Tabet, G. Pozzi, G. Grancini and M. K. Nazeeruddin, *Nano Letters*, 2018, **18**, 5467-5474.

240. X. Zhang, R. Munir, Z. Xu, Y. Liu, H. Tsai, W. Nie, J. Li, T. Niu, D.-M. Smilgies, M. G. Kanatzidis, A. D. Mohite, K. Zhao, A. Amassian and S. Liu, *Advanced Materials*, 2018, **30**, 1707166.
241. Y. Hu, J. Schlipf, M. Wussler, M. L. Petrus, W. Jaegermann, T. Bein, P. Müller-Buschbaum and P. Docampo, *ACS Nano*, 2016, **10**, 5999-6007.
242. J. J. Yoo, S. Wieghold, M. C. Sponseller, M. R. Chua, S. N. Bertram, N. T. P. Hartono, J. S. Tresback, E. C. Hansen, J.-P. Correa-Baena, V. Bulović, T. Buonassisi, S. S. Shin and M. G. Bawendi, *Energy & Environmental Science*, 2019, **12**, 2192-2199.
243. M. Jung, T. J. Shin, J. Seo, G. Kim and S. I. Seok, *Energy & Environmental Science*, 2018, **11**, 2188-2197.
244. S. Yang, Y. Wang, P. Liu, Y.-B. Cheng, H. J. Zhao and H. G. Yang, *Nature Energy*, 2016, **1**, 15016.
245. A. Dutta, S. K. Dutta, S. Das Adhikari and N. Pradhan, *Angewandte Chemie International Edition*, 2018, **57**, 9083-9087.
246. E. M. Sanehira, A. R. Marshall, J. A. Christians, S. P. Harvey, P. N. Ciesielski, L. M. Wheeler, P. Schulz, L. Y. Lin, M. C. Beard and J. M. Luther, *Science Advances*, 2017, **3**, eaao4204.
247. Y. Wang, M. I. Dar, L. K. Ono, T. Zhang, M. Kan, Y. Li, L. Zhang, X. Wang, Y. Yang, X. Gao, Y. Qi, M. Grätzel and Y. Zhao, *Science*, 2019, **365**, 591-595.
248. Y. Wang, T. Zhang, M. Kan, Y. Li, T. Wang and Y. Zhao, *Joule*, 2018, **2**, 2065-2075.
249. Y. Wang, T. Zhang, M. Kan and Y. Zhao, *Journal of the American Chemical Society*, 2018, **140**, 12345-12348.
250. D. Luo, W. Yang, Z. Wang, A. Sadhanala, Q. Hu, R. Su, R. Shivanna, G. F. Trindade, J. F. Watts, Z. Xu, T. Liu, K. Chen, F. Ye, P. Wu, L. Zhao, J. Wu, Y. Tu, Y. Zhang, X. Yang, W. Zhang, R. H. Friend, Q. Gong, H. J. Snaith and R. Zhu, *Science*, 2018, **360**, 1442-1446.
251. M. Tai, Y. Zhou, X. Yin, J. Han, Q. Zhang, Y. Zhou and H. Lin, *Journal of Materials Chemistry A*, 2019, **7**, 22675-22682.
252. B. Chen, P. N. Rudd, S. Yang, Y. Yuan and J. Huang, *Chemical Society Reviews*, 2019, **48**, 3842-3867
253. T. Niu, J. Lu, X. Jia, Z. Xu, M.-C. Tang, D. Barrit, N. Yuan, J. Ding, X. Zhang, Y. Fan, T. Luo, Y. Zhang, D.-M. Smilgies, Z. Liu, A. Amassian, S. Jin, K. Zhao and S. Liu, *Nano Letters*, 2019, DOI: 10.1021/acs.nanolett.9b02781.
254. F. Giustino and H. J. Snaith, *ACS Energy Letters*, 2016, **1**, 1233-1240.
255. F. Hao, C. C. Stoumpos, D. H. Cao, R. P. H. Chang and M. G. Kanatzidis, *Nature Photonics*, 2014, **8**, 489.
256. T. Miyasaka, A. Kulkarni, G. M. Kim, S. Öz and A. K. Jena, *Advanced Energy Materials*, 2019, **0**, 1902500.
257. I. Zimmermann, S. Aghazada and M. K. Nazeeruddin, *Angewandte Chemie International Edition*, 2019, **58**, 1072-1076.
258. C. Ran, J. Xi, W. Gao, F. Yuan, T. Lei, B. Jiao, X. Hou and Z. Wu, *ACS Energy Letters*, 2018, **3**, 713-721.
259. D. H. Cao, C. C. Stoumpos, T. Yokoyama, J. L. Logsdon, T.-B. Song, O. K. Farha, M. R. Wasielewski, J. T. Hupp and M. G. Kanatzidis, *ACS Energy Letters*, 2017, **2**, 982-990.
260. Y. Liao, H. Liu, W. Zhou, D. Yang, Y. Shang, Z. Shi, B. Li, X. Jiang, L. Zhang, L. N. Quan, R. Quintero-Bermudez, B. R. Sutherland, Q. Mi, E. H. Sargent and Z. Ning, *Journal of the American Chemical Society*, 2017, **139**, 6693-6699.
261. S. Shao, J. Liu, G. Portale, H.-H. Fang, G. R. Blake, G. H. ten Brink, L. J. A. Koster and M. A. Loi, *Advanced Energy Materials*, 2018, **8**, 1702019.
262. J. Qiu, Y. Xia, Y. Zheng, W. Hui, H. Gu, W. Yuan, H. Yu, L. Chao, T. Niu, Y. Yang, X. Gao, Y. Chen and W. Huang, *ACS Energy Letters*, 2019, **4**, 1513-1520.
263. M. Chen, M.-G. Ju, M. Hu, Z. Dai, Y. Hu, Y. Rong, H. Han, X. C. Zeng, Y. Zhou and N. P. Padture, *ACS Energy Letters*, 2019, **4**, 276-277.

264. M.-G. Ju, J. Dai, L. Ma, Y. Zhou, W. Liang and X. C. Zeng, *Journal of Materials Chemistry A*, 2019, **7**, 16742-16747.
265. D. B. Straus and C. R. Kagan, *The Journal of Physical Chemistry Letters*, 2018, **9**, 1434-1447.
266. C. Katan, N. Mercier and J. Even, *Chemical Reviews*, 2019, **119**, 3140-3192.
267. L. Zhang, Y. Liu, Z. Yang and S. Liu, *Journal of Energy Chemistry*, 2019, **37**, 97-110.
268. B. R. Sutherland and E. H. Sargent, *Nature Photonics*, 2016, **10**, 295-302.
269. Y.-H. Kim, H. Cho and T.-W. Lee, *Proceedings of the National Academy of Sciences*, 2016, **113**, 11694-11702.
270. Y.-H. Kim, H. Cho, J. H. Heo, T.-S. Kim, N. Myoung, C.-L. Lee, S. H. Im and T.-W. Lee, *Advanced Materials*, 2015, **27**, 1248-1254.
271. H. Zhu, Y. Fu, F. Meng, X. Wu, Z. Gong, Q. Ding, M. V. Gustafsson, M. T. Trinh, S. Jin and X. Y. Zhu, *Nature Materials*, 2015, **14**, 636-642.
272. X. Gong, Z. Yang, G. Walters, R. Comin, Z. Ning, E. Beauregard, V. Adinolfi, O. Voznyy and E. H. Sargent, *Nature Photonics*, 2016, **10**, 253-257.
273. X. Hong, T. Ishihara and A. V. Nurmikko, *Physical Review B*, 1992, **45**, 6961-6964.
274. M. Era, S. Morimoto, T. Tsutsui and S. Saito, *Applied Physics Letters*, 1994, **65**, 676-678.
275. K. Gauthron, J. S. Lauret, L. Doyennette, G. Lanty, A. Al Choueiry, S. J. Zhang, A. Brehier, L. Largeau, O. Mauguin, J. Bloch and E. Deleporte, *Opt. Express*, 2010, **18**, 5912-5919.
276. D. Liang, Y. Peng, Y. Fu, M. J. Shearer, J. Zhang, J. Zhai, Y. Zhang, R. J. Hamers, T. L. Andrew and S. Jin, *ACS Nano*, 2016, **10**, 6897-6904.
277. X. Gong, O. Voznyy, A. Jain, W. Liu, R. Sabatini, Z. Piontkowski, G. Walters, G. Bappi, S. Nokhrin, O. Bushuyev, M. Yuan, R. Comin, D. McCamant, S. O. Kelley and E. H. Sargent, *Nature Materials*, 2018, **17**, 550-556.
278. J. Byun, H. Cho, C. Wolf, M. Jang, A. Sadhanala, R. H. Friend, H. Yang and T.-W. Lee, *Advanced Materials*, 2016, **28**, 7515-7520.
279. N. Wang, L. Cheng, R. Ge, S. Zhang, Y. Miao, W. Zou, C. Yi, Y. Sun, Y. Cao, R. Yang, Y. Wei, Q. Guo, Y. Ke, M. Yu, Y. Jin, Y. Liu, Q. Ding, D. Di, L. Yang, G. Xing, H. Tian, C. Jin, F. Gao, R. H. Friend, J. Wang and W. Huang, *Nature Photonics*, 2016, **10**, 699.
280. B. Zhao, S. Bai, V. Kim, R. Lamboll, R. Shivanna, F. Auras, J. M. Richter, L. Yang, L. Dai, M. Alsari, X.-J. She, L. Liang, J. Zhang, S. Lilliu, P. Gao, H. J. Snaith, J. Wang, N. C. Greenham, R. H. Friend and D. Di, *Nature Photonics*, 2018, **12**, 783-789.
281. L. N. Quan, Y. Zhao, F. P. García de Arquer, R. Sabatini, G. Walters, O. Voznyy, R. Comin, Y. Li, J. Z. Fan, H. Tan, J. Pan, M. Yuan, O. M. Bakr, Z. Lu, D. H. Kim and E. H. Sargent, *Nano Letters*, 2017, **17**, 3701-3709.
282. J. Xing, Y. Zhao, M. Askerka, L. N. Quan, X. Gong, W. Zhao, J. Zhao, H. Tan, G. Long, L. Gao, Z. Yang, O. Voznyy, J. Tang, Z.-H. Lu, Q. Xiong and E. H. Sargent, *Nature Communications*, 2018, **9**, 3541.
283. X. Yang, X. Zhang, J. Deng, Z. Chu, Q. Jiang, J. Meng, P. Wang, L. Zhang, Z. Yin and J. You, *Nature Communications*, 2018, **9**, 570.
284. Y. Shang, Y. Liao, Q. Wei, Z. Wang, B. Xiang, Y. Ke, W. Liu and Z. Ning, *Science Advances*, 2019, **5**, eaaw8072.
285. H. Tsai, W. Nie, J.-C. Blancon, C. C. Stoumpos, C. M. M. Soe, J. Yoo, J. Crochet, S. Tretiak, J. Even, A. Sadhanala, G. Azzellino, R. Brenes, P. M. Ajayan, V. Bulović, S. D. Stranks, R. H. Friend, M. G. Kanatzidis and A. D. Mohite, *Advanced Materials*, 2018, **30**, 1704217.
286. A. Yangui, D. Garrot, J. S. Lauret, A. Lusson, G. Bouchez, E. Deleporte, S. Pillet, E. E. Bendeif, M. Castro, S. Triki, Y. Abid and K. Boukheddaden, *The Journal of Physical Chemistry C*, 2015, **119**, 23638-23647.
287. I. Neogi, A. Bruno, D. Bahulayan, T. W. Goh, B. Ghosh, R. Ganguly, D. Cortecchia, T. C. Sum, C. Soci, N. Mathews and S. G. Mhaisalkar, *ChemSusChem*, 2017, **10**, 3765-3772.
288. M. D. Smith and H. I. Karunadasa, *Accounts of Chemical Research*, 2018, **51**, 619-627.

289. J. Yu, J. Kong, W. Hao, X. Guo, H. He, W. R. Leow, Z. Liu, P. Cai, G. Qian, S. Li, X. Chen and X. Chen, *Advanced Materials*, 2019, **31**, 1806385.
290. E. P. Booker, T. H. Thomas, C. Quarti, M. R. Stanton, C. D. Dashwood, A. J. Gillett, J. M. Richter, A. J. Pearson, N. J. L. K. Davis, H. Sirringhaus, M. B. Price, N. C. Greenham, D. Beljonne, S. E. Dutton and F. Deschler, *Journal of the American Chemical Society*, 2017, **139**, 18632-18639.
291. Q. Zhang, Y. Ji, Z. Chen, D. Vella, X. Wang, Q.-H. Xu, Y. Li and G. Eda, *The Journal of Physical Chemistry Letters*, 2019, **10**, 2869-2873.
292. T. Li, X. Chen, X. Wang, H. Lu, Y. Yan, M. C. Beard and D. B. Mitzi, *ACS Energy Letters*, 2019, DOI: 10.1021/acsenergylett.9b02490, 347-352.
293. X. Wang, W. Meng, W. Liao, J. Wang, R.-G. Xiong and Y. Yan, *The Journal of Physical Chemistry Letters*, 2019, **10**, 501-506.
294. E. I. J. S. P. Rashba, Solid State, 1960, **2**, 1109-1122.
295. M. Kepenekian and J. Even, *The Journal of Physical Chemistry Letters*, 2017, **8**, 3362-3370.
296. P. Odenthal, W. Talmadge, N. Gundlach, R. Wang, C. Zhang, D. Sun, Z.-G. Yu, Z. Valy Vardeny and Y. S. Li, *Nature Physics*, 2017, **13**, 894.
297. J. Wang, C. Zhang, H. Liu, R. McLaughlin, Y. Zhai, S. R. Vardeny, X. Liu, S. McGill, D. Semenov, H. Guo, R. Tsuchikawa, V. V. Deshpande, D. Sun and Z. V. Vardeny, *Nature Communications*, 2019, **10**, 129.
298. E. Mosconi, T. Etienne and F. De Angelis, *The Journal of Physical Chemistry Letters*, 2017, **8**, 2247-2252.
299. X. Che, B. Traore, C. Katan, M. Kepenekian and J. Even, *Physical Chemistry Chemical Physics*, 2018, **20**, 9638-9643.
300. D. Niesner, M. Wilhelm, I. Levchuk, A. Osvet, S. Shrestha, M. Batentschuk, C. Brabec and T. Fauster, *Physical Review Letters*, 2016, **117**, 126401.
301. Y. A. Bychkov and É. I. Rashba, *Soviet Journal of Experimental and Theoretical Physics Letters*, 1984, **39**, 78.
302. K. Liao, X. Hu, Y. Cheng, Z. Yu, Y. Xue, Y. Chen and Q. Gong, *Advanced Optical Materials*, 2019, **7**, 1900350.
303. P. Odenthal, W. Talmadge, N. Gundlach, R. Wang, C. Zhang, D. Sun, Z.-G. Yu, Z. Valy Vardeny and Y. S. Li, *Nature Physics*, 2017, **13**, 894-899.
304. Y. Yang, M. Yang, K. Zhu, J. C. Johnson, J. J. Berry, J. van de Lagemaat and M. C. Beard, *Nature Communications*, 2016, **7**, 12613.
305. D. Sun, C. Zhang, M. Kavand, K. J. van Schooten, H. Malissa, M. Groesbeck, R. McLaughlin, C. Boehme and Z. V. Vardeny, *arXiv preprint arXiv:1608.00993*, 2016.
306. Y. Zhai, S. Baniya, C. Zhang, J. Li, P. Haney, C.-X. Sheng, E. Ehrenfreund and Z. V. Vardeny, *Science Advances*, 2017, **3**, e1700704.
307. J. Yin, P. Maity, L. Xu, A. M. El-Zohry, H. Li, O. M. Bakr, J.-L. Brédas and O. F. Mohammed, *Chemistry of Materials*, 2018, **30**, 8538-8545.
308. S. B. Todd, D. B. Riley, A. Binai-Motlagh, C. Clegg, A. Ramachandran, S. A. March, J. M. Hoffman, I. G. Hill, C. C. Stoumpos, M. G. Kanatzidis, Z.-G. Yu and K. C. Hall, *APL Materials*, 2019, **7**, 081116.
309. X. Chen, H. Lu, Z. Li, Y. Zhai, P. F. Ndione, J. J. Berry, K. Zhu, Y. Yang and M. C. Beard, *ACS Energy Letters*, 2018, **3**, 2273-2279.
310. D. Giovanni, W. K. Chong, H. A. Dewi, K. Thirumal, I. Neogi, R. Ramesh, S. Mhaisalkar, N. Mathews and T. C. Sum, *Science Advances*, 2016, **2**, e1600477.
311. D. Giovanni, J. W. M. Lim, Z. Yuan, S. S. Lim, M. Righetto, J. Qing, Q. Zhang, H. A. Dewi, F. Gao, S. G. Mhaisalkar, N. Mathews and T. C. Sum, *Nature Communications*, 2019, **10**, 3456.
312. G. Long, C. Jiang, R. Sabatini, Z. Yang, M. Wei, L. N. Quan, Q. Liang, A. Rasmita, M. Askerka, G. Walters, X. Gong, J. Xing, X. Wen, R. Quintero-Bermudez, H. Yuan, G. Xing, X. R. Wang,

D. Song, O. Voznyy, M. Zhang, S. Hoogland, W. Gao, Q. Xiong and E. H. Sargent, *Nature Photonics*, 2018, **12**, 528-533.

313. J. Ma, C. Fang, C. Chen, L. Jin, J. Wang, S. Wang, J. Tang and D. Li, *ACS Nano*, 2019, **13**, 3659-3665.
314. H. Lu, J. Wang, C. Xiao, X. Chen, R. Brunecky, J. J. Berry, K. Zhu, M. C. Beard and Z. V. Vardeny, *Science Advances*, 2019, **5**, aay0571.
315. B. P. Bloom, V. Kiran, V. Varade, R. Naaman and D. H. Waldeck, *Nano Letters*, 2016, **16**, 4583-4589.
316. P. C. Mondal, C. Fontanesi, D. H. Waldeck and R. Naaman, *Accounts of Chemical Research*, 2016, **49**, 2560-2568.
317. V. Kiran, S. R. Cohen and R. Naaman, *The Journal of Chemical Physics*, 2017, **146**, 092302.
318. L. Dou, Y. Yang, J. You, Z. Hong, W.-H. Chang, G. Li and Y. Yang, *Nature Communications*, 2014, **5**, 5404.
319. Y. Fang, Q. Dong, Y. Shao, Y. Yuan and J. Huang, *Nature Photonics*, 2015, **9**, 679-686.
320. M. Ahmadi, T. Wu and B. Hu, *Advanced Materials*, 2017, **29**, 1605242.
321. F. P. García de Arquer, A. Armin, P. Meredith and E. H. Sargent, *Nature Reviews Materials*, 2017, **2**, 16100.
322. Akriti, E. Shi and L. Dou, *Trends in Chemistry*, 2019, **1**, 365-367.
323. Y. Liu, H. Ye, Y. Zhang, K. Zhao, Z. Yang, Y. Yuan, H. Wu, G. Zhao, Z. Yang, J. Tang, Z. Xu and S. Liu, *Matter*, 2019, **1**, 465-480.
324. N. Zhou, B. Huang, M. Sun, Y. Zhang, L. Li, Y. Lun, X. Wang, J. Hong, Q. Chen and H. Zhou, *Advanced Energy Materials*, 2019, **0**, 1901566.
325. M. Long, T. Zhang, D. Chen, M. Qin, Z. Chen, L. Gong, X. Lu, F. Xie, W. Xie, J. Chen and J. Xu, *ACS Energy Letters*, 2019, **4**, 1025-1033.